

U.S. DEPARTMENT OF COMMERCE
National Technical Information Service

AD-A034 383

INVESTIGATION OF TECHNOLOGICAL PROBLEMS IN GaAs

ROCKWELL INTERNATIONAL, THOUSAND OAKS, CALIFORNIA

AUGUST 1976

20
ADA 034383

REPRODUCED BY
**NATIONAL TECHNICAL
INFORMATION SERVICE**
U. S. DEPARTMENT OF COMMERCE
SPRINGFIELD, VA. 22161

This report has been reviewed by the RADC Information Office (OI) and is releasable to the National Technical Information Service (NTIS). At NTIS it will be releasable to the general public, including foreign nations.

This technical report has been reviewed and is approved.

Sven A. Rosild

SVEN A. ROSILD
Contract Monitor
Solid State Sciences Division

Unclassified

SECURITY CLASSIFICATION OF THIS PAGE (When Data Entered)

REPORT DOCUMENTATION PAGE		READ INSTRUCTIONS BEFORE COMPLETING FORM
1. REPORT NUMBER RADC-TR-76-342	2. GOVT ACCESSION NO.	3. RECIPIENT'S CATALOG NUMBER
4. TITLE (and Subtitle) INVESTIGATION OF TECHNOLOGICAL PROBLEMS IN GaAs		5. TYPE OF REPORT & PERIOD COVERED Semi-annual Technical Report (1/16/76 - 7/15/76) No. 3
		6. PERFORMING ORG. REPORT NUMBER SC5017.13SAR
7. AUTHOR(s) Fred H. Eisen, John A. Higgins, G. D. Robinson, Bryant M. Welch, Cheng P. Wen, Ricardo Zucca		8. CONTRACT OR GRANT NUMBER(s) F19628-75-C-0113
9. PERFORMING ORGANIZATION NAME AND ADDRESS Science Center, Rockwell International Thousand Oaks, CA 91360		10. PROGRAM ELEMENT, PROJECT, TASK AREA & WORK UNIT NUMBERS 61101E ARPA No. 2489 2489 T&WU n/a
11. CONTROLLING OFFICE NAME AND ADDRESS Defense Advanced Research Projects Agency 1400 Wilson Boulevard Arlington, VA 22209		12. REPORT DATE August, 1976
		13. NUMBER OF PAGES 118
14. MONITORING AGENCY NAME & ADDRESS (If different from Controlling Office) Deputy for Electronic Technology (RADC/ETSD) Hanscom AFB, MA 01731 Monitor: S. A. Roosild		15. SECURITY CLASS. (of this report) Unclassified
		15a. DECLASSIFICATION/DOWNGRADING SCHEDULE
16. DISTRIBUTION STATEMENT (of this Report) A. Approved for public release; distribution unlimited		
17. DISTRIBUTION STATEMENT (of the abstract entered in Block 20, if different from Report)		
18. SUPPLEMENTARY NOTES This research was supported by the Defense Advanced Research Projects Agency. ARPA Order No. 2489		
19. KEY WORDS (Continue on reverse side if necessary and identify by block number) Ion Implantation MESFET Semi-insulating GaAs IMPATT GaAs Substrate Ionization Coefficients GaAs Epitaxy		
20. ABSTRACT (Continue on reverse side if necessary and identify by block number) Significant progress in areas of GaAs technology with impact on the development of microwave FET devices is reported. Improvement in the yield of bulk semi-insulating GaAs substrate material has been achieved by refining fabrication procedures. Transport measurements on semi-insulating GaAs have led to interpretation of the electrical compensation in terms of a deep-donor-deep-acceptor model. Transient capacitance measurements have confirmed that the growth of FET active layers on high-resistivity buffer layers results in the elimination		

DD FORM 1 JAN 73 1473

EDITION OF 1 NOV 65 IS OBSOLETE


Unclassified

SECURITY CLASSIFICATION OF THIS PAGE (When Data Entered)

Unclassified

SECURITY CLASSIFICATION OF THIS PAGE(When Data Entered)

of interface traps. In ion implantation, a simple annealing technique which avoids the use of any protective cap has been successfully applied to high dose Se implants. A test to preselect substrates for ion implantation has been developed, leading to good reproducibility of carrier concentration profiles. Accurate measurements of ionization coefficients have confirmed the dependence of electron ionization rates on doping density. Improved RF performance has been achieved from FET devices made on Se implanted layers. These devices are free from short term drift problems exhibited by transistors made on epitaxial layers.



Unclassified

SECURITY CLASSIFICATION OF THIS PAGE(When Data Entered)

SUBCONTRACTORS

K. Gamo, T. Inada, E. F. Kennedy, R. Pretorius, M. Wittner, J. W. Mayer,
M-A. Nicolet

California Institute of Technology
Pasadena, California 91109

L. F. Eastman, D. Law, C. A. Lee, and H. Morkoc

Cornell University
Ithaca, New York 14853

B. L. Mattes, G. L. Pearson, Y. M. Houn

Stanford University
Stanford, California 94305

W. P. Allred

Crystal Specialties, Inc.
Monrovia, California 91016

ACCESSION for		
RTIS	White Section	<input checked="" type="checkbox"/>
DDC	Buff Section	<input type="checkbox"/>
UNANNOUNCED		<input type="checkbox"/>
JUSTIFICATION		
BY		
DISTRIBUTION/AVAILABILITY CODES		
Dist.	MAIL	and/or SPECIAL
<i>A</i>		

TABLE OF CONTENTS

	<u>Page</u>
1.0 INTRODUCTION	1
2.0 HIGHLIGHTS	2
2.1 Semi-Insulating Substrate Material Growth	2
2.2 Semi-Insulating Material Evaluation	2
2.3 Epitaxial Material Growth and Characterization	3
2.4 Ion Implantation and Ion Beam Analysis	3
2.5 Effects of Material Properties on FET Performance	4
2.6 Avalanche Parameters	4
3.0 SEMI-INSULATING SUBSTRATE MATERIAL	6
3.1 Material Growth - Crystal Specialties	6
3.2 Material Evaluation	10
3.2.1 Bulk Electrical Properties of Semi-Insulating GaAs - Science Center	10
A. Deep Acceptor Model	13
B. Deep-Donor-Deep-Acceptor Model	16
A. Low-Cr Case	24
B. Mid-Cr Case	26
C. High-Cr Case	30
3.2.2 Effects of Heat Treatment on Semi-Insulating GaAs - Science Center	34
3.2.3 Study of Inclusions in Semi-Insulating GaAs - Cornell University	42
4.0 EPITAXIAL MATERIAL GROWTH AND CHARACTERIZATION	43
4.1 Growth and Evaluation of Semi-Insulating Liquid Phase Epitaxial GaAs - Stanford University	44
A. Growth Studies	44
B. Evaluation of Buffer Layers - Buffered vs. Unbuffered Structures.	50
4.2 LPE Growth of Active and Buffer Layers for Microwave FETs - Cornell University	55
5.0 ION IMPLANTATION AND ION BEAM ANALYSIS	58
5.1 Substrate Qualification - Science Center	58
5.2 Capless Annealing of High Dose Se Implants - Science Center and California Institute of Technology	64
5.3 Investigations of the Ge-Au-Ni System Used For Contacts to GaAs - California Institute of Technology	67

TABLE OF CONTENTS (Cont'd)

	<u>Page</u>
5.4 Reordering of Implanted Amorphous Layers in GaAs - Science Center and California Institute of Technology . . .	73
6.0 EFFECTS OF MATERIAL PARAMETERS ON DEVICE PERFORMANCE	86
6.1 Characterization of FETs Fabricated on Epitaxial and Implanted Active Layers - Science Center	86
6.2 GaAs Ionization Coefficients	90
7.0 FUTURE PLANS	103
7.1 Semi-Insulating Substrate Material Growth - Crystal Specialties	103
7.2 Semi-Insulating Substrate Material Evaluation - Science Center	103
7.3 LPE Growth and Evaluation of Semi-Insulating Buffer Layers - Stanford University	103
7.4 LPE Growth of FET Active Buffer Layers - Cornell University	104
7.5 Ion Implantation and Ion Beam Analysis	104
7.6 Effects of Material Parameters on FET Performance - Science Center	104
7.7 GaAs Ionization Coefficients - Cornell University	104
8.0 REFERENCES	105

LIST OF FIGURES

<u>Figure</u>		<u>Page</u>
1	Yield of single crystal material at Crystal Specialties . .	7
2	Percentage of successfully grown semi-insulating crystals which had high resistivity ($\rho > 10^7$ ohm-cm)	9
3	Graphic representation of n , p , N_d^+ and N_a^- as functions of the position of the Fermi level in the energy gap; (a) for the deep-acceptor model, (b) for the deep-donor-deep acceptor model.	15
4	Resistivity vs. temperature data for all samples	22
5	Plot of $\rho T^{3/2}$ vs. $1/T'$ for the low-Cr data of Fig. 2. The temperature scale was corrected for the effect of the thermal variation of the energy gap, $T' = T E_g(298K)/E_g(T)$. The solid line is the result of a linear least square fit	25
6	Result of a non-linear least square fit of the mid-Cr data for $E_C - E_d = 0.64$ eV. Fitting parameters: $N_a/N_d = 0.98$; $E_C - E_a = 0.90$ eV. The dots represent the experimental points.	28
7	Plot of the mean square error ϵ and the fitting parameters N_a/N_d and $E_C - E_a$ against the parameter $E_C - E_d$ in the non-linear least square fit of the mid-Cr data	29
8	Result of a non-linear least square fit of the high-Cr data for $E_C - E_d = 0$. Fitting parameters: $N_a/N_d = 1.04$; $E_C - E_d = 0.83$ eV. The dots represent the experimental points. The dashed lines represent the separate contributions of electrons and holes	31
9	Plot of the mean square error ϵ and the fitting parameters N_a/N_d and $E_C - E_a$ against the parameter $E_C - E_d$ in the non-linear least square fit of the high-Cr data	32
10	Sheet resistance as a function of the Cr concentration for several samples (identified by boule numbers) heat treated at 750°C for 2 hrs. in H_2 atmosphere. The Al contact pattern used for the measurement is shown in the insert	36
11	Intensity of the photoluminescence peaks (at 77K) and resistance between two contacts as functions of the thickness of material removed by sequential etching	38
12	Photoluminescence of a heat treated sample from boule 2109 measured at 25K.	39

LIST OF FIGURES (Cont'd)

<u>Figure</u>		<u>Page</u>
13	Carrier density vs. bakeout temperature for three different growth systems: C: Fused quartz-graphite-hydrogen ($\text{SiO}_2\text{-C-H}_2$) system; BN(C): Fused quartz-boron nitride (on graphite cradle) - hydrogen ($\text{SiO}_2\text{-BN(C)-H}_2$) system; BN: Fused quartz-boron nitride-hydrogen ($\text{SiO}_2\text{-BN-H}_2$) system	51
14	Schematic diagram of the transient capacitance measurement setup and the capacitance variation with time corresponding to different bias states. W is the depletion region width of the Schottky barrier	53
15	Temperature dependence of the corrected time constant (τT^2) of the transient capacitance of an n-type GaAs FET active layer grown on a Cr-doped substrate	54
16	Electron concentration profiles for various GaAs substrates implanted at 350°C with 1.8×10^{12} 400 keV Si ions/cm ² and annealed at 850°C for 30 min with a silicon nitride cap . .	62
17	Electron concentration and mobility profiles for semi-insulating GaAs samples implanted with 1×10^{14} 400 keV Se ions/cm ² at 350°C and annealed under the conditions indicated	65
18	Electron concentration and mobility profiles for semi-insulating GaAs samples implanted with 2×10^{14} 400 keV Se ions/cm ² at 350°C and annealed under the conditions indicated	66
19	Backscattering spectra for 2 MeV He ions incident on a Ni-Ge sample before and after annealing at 250°C for 1 hr.	69
20	Backscattering spectra for 2 MeV He ions incident on a Ni-Ge sample before and after annealing at 300°C for 1 hr.	70
21	Backscattering spectra for 2 MeV He ions incident on a Ni-Au-Ge sample before and after annealing at 450°C for 1 hr.	71
22	Backscattering spectra for 2 MeV He ions incident on a Au-Ni-Ge sample before and after annealing at 450°C for 5 min	72
23	Random and $\langle 110 \rangle$ aligned backscattering spectra from $\langle 100 \rangle$ GaAs samples implanted with Zn and annealed for 15 min at the indicated temperatures	76

LIST OF FIGURES (Cont'd)

<u>Figure</u>		<u>Page</u>
24	Random and $\langle 110 \rangle$ aligned backscattering spectra from $\langle 100 \rangle$ (a and b) GaAs samples implanted with Zn and annealed as indicated	78
24	Random and $\langle 110 \rangle$ aligned backscattering spectra from $\langle 111 \rangle$ (c and d) GaAs samples implanted with Zn and annealed as indicated	79
25(a)	Random and aligned spectra from Se implanted GaAs samples annealed as indicated. $\langle 111 \rangle$ GaAs and $\langle 111 \rangle$ aligned spectra	81
25(b)	Random and aligned spectra from Se implanted GaAs samples annealed as indicated. $\langle 100 \rangle$ GaAs and $\langle 100 \rangle$ aligned spectra	82
26	TEM of GaAs implanted with 400 keV Se ions and annealed at 200°C for 1100 minutes. (a) Dark field image illustrating crystalline substructure in implanted layer. g: $\langle 111 \rangle$ streak. (b) Selected area diffraction pattern, $[110]$ zone normal with intense $\langle 111 \rangle$ streaking	84
27	Saturation characteristics of FETs fabricated from an epitaxial layer. (a) grown on an unbuffered semi-insulating substrate, (b) grown on a high resistivity LPE buffer layer	89
28	Ionization coefficients of electron and hole in GaAs . . .	97
29(a)	Multiplication profile inside the diode ($N = 9.5 \times 10^{15} \text{cm}^{-3}$) for $M = 1$	98
29(b)	Multiplication profile inside same diode in Fig. 29(a) for $M \approx 2$	98
30	Pt Schottky barrier in GaAs with native oxide guard ring .	102

LIST OF TABLES

<u>Table Number</u>		<u>Page</u>
I	Results of Resistivity-Hall Measurements at Room Temperature	19
II	Properties of Epitaxial GaAs Layers Grown in a SiO ₂ -BN-H ₂ System; Growth Series #1700	46
III	Properties of Undoped Epitaxial Layers Grown in a SiO ₂ -BN-H ₂ System; Growth Series #1800 and 1900	47
IV	Properties of Undoped Epitaxial GaAs Layers Grown in a SiO ₂ -BN-H ₂ System; Growth Series #2000	48
V	Properties of Epitaxial GaAs Layers Grown in a SiO ₂ -BN-H ₂ System; Growth Series #2100	49
VI	Si ₃ N ₄ Capped, Cr-doped GaAs Samples Annealed at 850°C for 30 Minutes	60
VII	Average Profile Parameters for Se Implants (400 keV - 1.8x10 ¹² ions/cm ²) into Cr-doped Semi-Insulating GaAs from 5 Different Boules	63
VIII	Summary of RF Measurements of FETs at 10 GHz	87

1.0 INTRODUCTION

The work described in this report includes results on the preparation and evaluation of Cr-doped semi-insulating GaAs as a substrate for the production of active layers for FETs by epitaxial growth or by ion implantation. The growth of buffer layers and growth of epitaxial layers on buffer layers has also been investigated. The performance of FETs fabricated on Se implanted layers has been measured. In addition to these efforts which relate most closely to GaAs FET devices a study of avalanche phenomena, of interest for IMPATT diode applications, has also been carried out.

The principal results described in this report include improvements in the yield of bulk semi-insulating GaAs and the interpretation of transport measurements in this material in terms of a deep-donor-deep-acceptor model. Transient capacitance measurements have confirmed that the growth of FET active layers on high resistivity buffer layers results in the elimination of interface traps. In ion implantation progress has been made in high dose Se implants by the successful application of a simple capless annealing technique; and in low dose Se implants by the preselection of substrates, resulting in good reproducibility of carrier concentration profiles. Improved RF performance has been achieved from FETs made on Se implanted layers and these devices are free from the short term drift problems exhibited by FETs made on epitaxial layers. Accurate measurements of ionization coefficients have confirmed the previously reported dependence of electron ionization rates on doping density.

2.0 HIGHLIGHTS

Highlights of the progress made in the various areas of research during the period 1-16-76 to 7-15-76 are presented.

2.1 Semi-Insulating Substrate Material Growth

Crystal Specialties has a dual role; (1) supplying substrate materials for all the activities in this program, and (2) investigating growth of bulk semi-insulating GaAs. Significant improvement in the yield of semi-insulating GaAs (80% on a monthly basis) has been achieved by refining fabrication procedures. Problems which previously made it difficult to achieve electrical compensation have been eliminated, leaving boat wetting as the main yield limiting factor. Occasional drops in yield due to this cause are being investigated.

2.2 Semi-Insulating Material Evaluation

This activity, carried out at the Science Center, covers two areas. In the first area, the study of bulk electrical properties, preliminary transport measurements had indicated that the "conventional" model for the electrical compensation involving only a deep acceptor level might be invalid and suggested its replacement by a model which includes both the deep acceptor and a deep donor level. This conclusion has been verified by additional measurements and by further analysis of experimental data. In the second area, the study of surface stability under heat treatment, a prominent acceptor peak has been observed in the photoluminescence spectra of the low resistivity surface layers formed by heat treatment.

2.3 Epitaxial Material Growth and Characterization

Liquid phase epitaxial growth is carried out at Stanford University and Cornell University. The goal of Stanford's work is to grow high resistivity compensated buffer layers. Earlier work has demonstrated that the melt bakeout temperature is the most critical parameter for achieving high resistivity. The optimum bakeout temperature has been determined and compared for three different growth systems, the most recent consisting of a pyrolytic BN boat in a fused quartz tube. Transient capacitance measurements have been used to compare n-type FET layers grown with and without a high resistivity buffer layer. These measurements confirmed the important advantage of growing the active layer on a buffer layer in that no traps were observed near the interface with the active layer. This observation is in contrast to active layers grown directly on the semi-insulating substrate, which displayed interface traps.

Cornell University is growing buffered FET structures. Their approach is to rely on high purity undoped buffer layers, with emphasis on developing a multilayer growth capability. High purity undoped buffer layers with an estimated net hole concentration of $2-4 \times 10^{13} \text{ cm}^{-3}$ have been grown in a Spectrosil quartz boat.

2.4 Ion Implantation and Ion Beam Analysis

This activity is carried out in close cooperation between the Science Center and California Institute of Technology. Implantation and annealing were done by the Science Center group while backscattering experiments were carried out mainly by the Caltech group. A simple annealing technique which

avoids the use of a protective cap has been successfully applied to high dose Se implants. A test to preselect substrates for ion implantation has been developed. Reproducibility of carrier concentration profiles in preselected substrates from five different boules was $\pm 10\%$ in peak doping level and depth. Backscattering has been used to study the annealing behavior of amorphous layers caused by ion implantation revealing a reordering process different from the simple epitaxial regrowth found in Si and Ge. Preliminary backscattering results have been obtained in an investigation of the Ge-Au-Ni system commonly used for ohmic contacts in GaAs.

2.5 Effects of Material Properties on FET Performance

At the Science Center, $1\mu\text{m}$ Schottky barrier gate FETs were fabricated on active layers made by liquid phase epitaxy and by Se implantation. Improved RF performance has been achieved from FET devices made on implanted layers (10 dB maximum available gain, 3.4 dB noise figure at 10 GHz). The implanted transistors are free from the short term drift problems exhibited by epitaxial transistors.

2.6 Avalanche Parameters

At Cornell University, experimental measurements of the low frequency noise of IMPATT diodes have been successfully used to extract parameters such as intrinsic response time and the multiplication factors under operating conditions of the diode. Knowledge of these parameters can be exploited to improve device design. Ionization coefficients for GaAs were measured on sample diodes displaying very uniform breakdown characteristics. The results

confirm the previously observed dependence of the electron ionization rate on doping density. An interpretation of this effect in terms of the newly proposed electron interband scattering effects has been carried out in detail.

3.0 SEMI-INSULATING SUBSTRATE MATERIAL

3.1 Material Growth - Crystal Specialties

Two major causes have been identified that limit the yield of single crystals by producing dislocations, slip, lineage and polycrystal formation. One of these is the solubility of gases in the molten GaAs. Gases such as H, He, N₂ or CO₂ are soluble in the melt and segregate upon solidification, similar to any other normal impurity. Gas contamination which exceeds the solubility limit would, therefore, be expected to produce dislocations, slip, lineage and nucleation of polycrystalline material. When use of N₂ as a backfill gas was discontinued, the yield of single crystals was greatly increased.

The second cause of growth failure, and the most difficult to correct, is that of boat "wetting" or "keying." The adherence of the growing crystal to the boat has been discussed in the previous report.¹ This causes stress in the ingot which produces dislocation, slip, lineage and polycrystal formation.

The usual boat material is quartz. Other materials such as BN or carbon have been evaluated but were found to be unacceptable.¹

All of the conditions which contribute to boat wetting are not understood. Water or hydroxyl ions in the quartz tubing, water induced during fabrication of the quartz boat, loading techniques, etching process, inadequate pumping as well as the As and Ga are all suspect.

Fig. 1 shows the monthly yield of single crystal material since January, 1975. A sudden increase of yield took place in January, 1976. This was achieved by eliminating N₂ backfill of the ampoules. Further im-

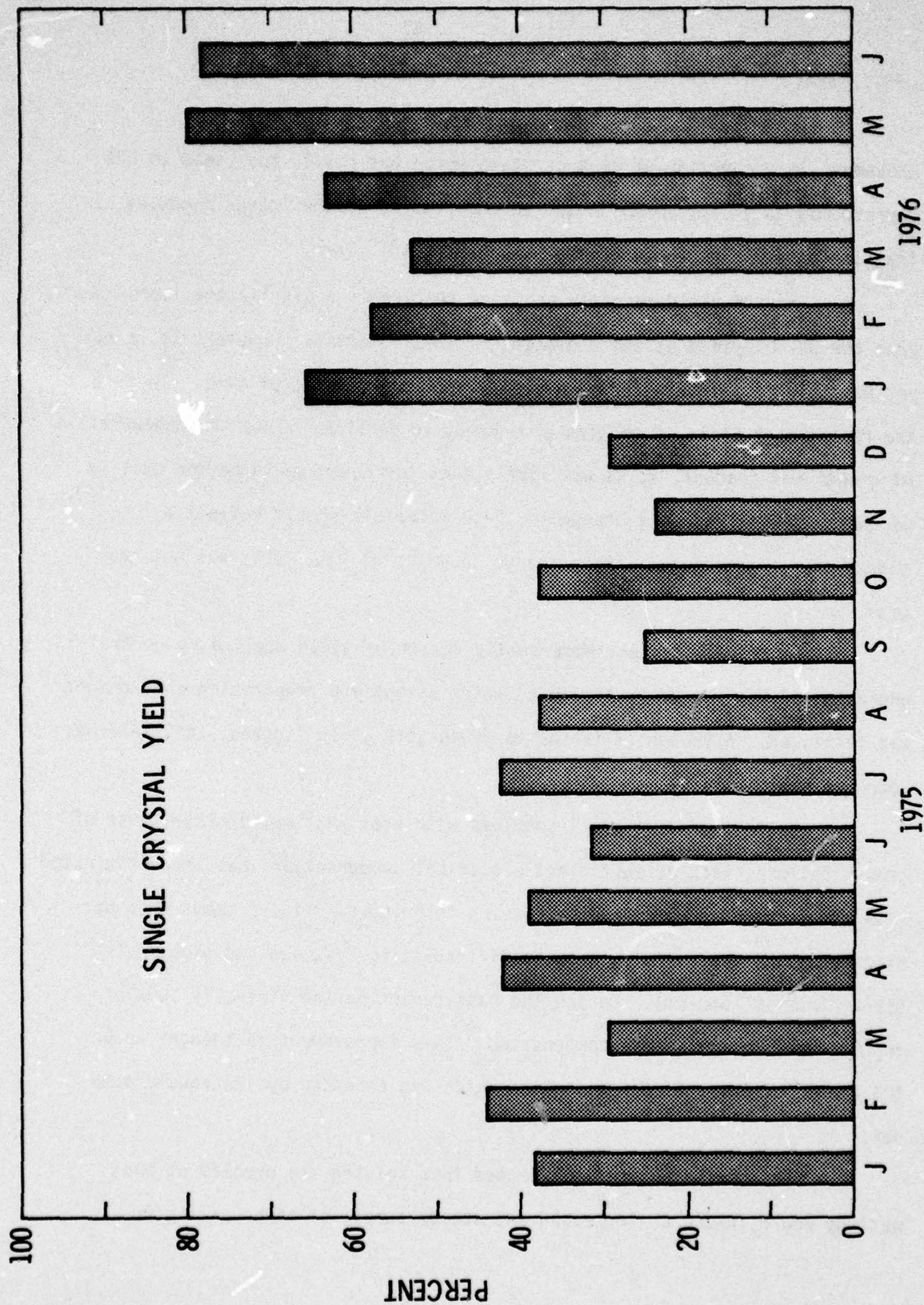


Fig. 1 Yield of single crystal material at Crystal Specialties.

provement in production of good crystals which has raised the yield to 80% corresponds to improvements in the vacuum pumping of the loaded ampoules so that the bakeout is now done at a pressure of 10^{-5} Torr.

The 80% yield recently achieved represents a significant improvement from the 30-40% yield at the beginning of this contract. However, it is not yet possible to maintain the high yield over long periods of time. In fact the recent high yield is showing a tendency to decline. Since the degeneration of growth was gradual, it is not likely that the cause would be the quality of quartz, Ga or As. Any change in these materials should reflect a sudden change associated with a change in material lot. This was not the case.

In order to attack more subtle causes of yield decline, a general upgrading of the vacuum system, D.I. water system and preparation environment was initiated. Although it is too early to give yield figures, the yield has improved substantially.

While there are still problems with boat wetting, another cause of growth failure, lack of sufficient electrical compensation, has been eliminated with the improved pumping and outgassing techniques. Fig. 2 shows what percentage of the successfully grown semi-insulating crystals had high resistivity ($\rho > 10^7$ ohm-cm). During the past report period virtually 100% of the Cr doped crystals were compensated. This improvement is thought to be the result of lower Si contamination which was enhanced by inadequate pump out.

In conclusion, it is expected that solving the problem of boat wetting would insure an increased and steady supply of high quality Cr-

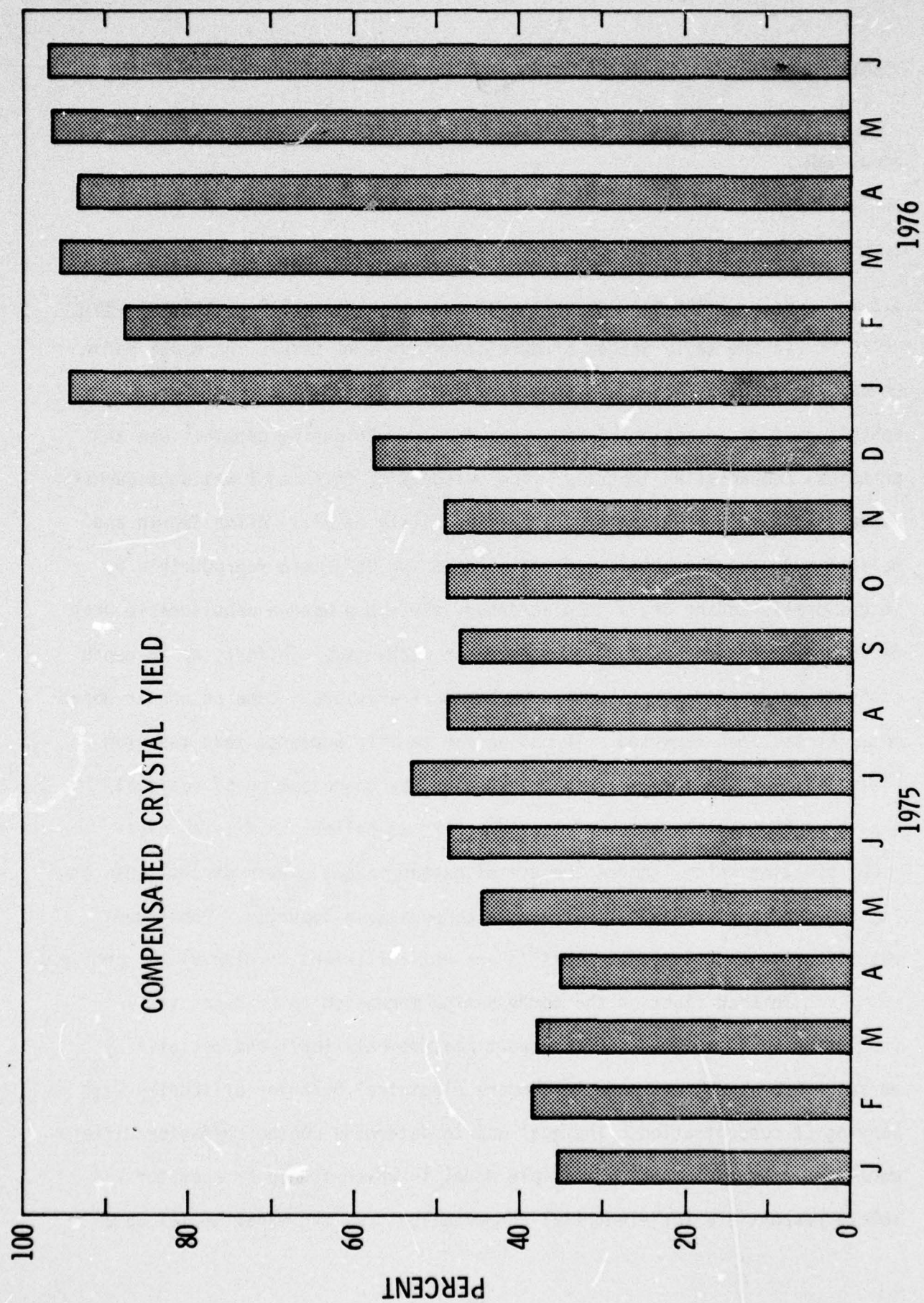


Fig. 2 Percentage of successfully grown semi-insulating crystals which had high resistivity ($\rho > 10^7$ ohm-cm).

doped GaAs.

3.2 Material Evaluation

3.2.1 Bulk Electrical Properties of Semi-Insulating GaAs - Science Center

In the early stages of development of semi-insulating GaAs, before Cr doping was used, Blanc and Weisberg² proposed that O, commonly used as an inhibitor of dissociation of SiO₂ from the ampoule during growth,¹ was the principal compensating impurity. The validity of this model was subsequently demonstrated by the doping experiments of Haisty et al.³ After Cronin and Haisty⁴ made the preparation of semi-insulating GaAs more reproducible by intentionally adding Cr, a deep acceptor, there has been a considerable drop of interest in the electrical compensation mechanism. In fact, no in-depth study of Cr-doped GaAs comparable to the work previously done on non-Cr-doped material has been reported. It has become tacitly accepted that the high resistivity of the material can be explained by compensation of residual shallow donors by the deep Cr acceptors.⁵⁻⁶ We believe this is an oversimplification which ignores the use of oxygen in the growth of semi-insulating GaAs and the proven role of O as a compensating impurity. Published results of transport measurements⁵⁻⁷ are not sufficient to clarify the problem.

To shed light on the compensation mechanism in Cr-doped semi-insulating GaAs, a series of transport measurements (Hall and resistivity versus temperature) was made to compare electrical behavior of samples with varying Cr concentration. The goal was to determine whether behavior differences could be explained by a simple model in which a deep Cr acceptor was solely responsible for electrical compensation. As the experimental data

are analyzed, it will become clear that such a model is incorrect. An extension of Blanc and Weisberg's model³ for non-Cr-doped semi-insulating GaAs, involving both a deep O donor and a deep Cr acceptor is proposed to properly interpret the experimental data. Although preliminary results were presented and discussed in the previous report,¹ a full discussion of the problem is presented here for completeness.

The resistivity ρ of the material is governed by the well-known general equations

$$\rho = (q\mu_e n + q\mu_h p)^{-1} \quad (1)$$

$$n = N_C \exp \left[- (E_C - E_f)/kT \right] \quad (2)$$

$$p = N_V \exp \left[- (E_f - E_V)/kT \right] , \quad (3)$$

where q is the elementary charge, μ_e and μ_h are the electron and hole mobility respectively, E_C and E_V are the energies of the conduction and valence band edges respectively, E_f is the Fermi energy, k is Boltzmann's constant, T is the absolute temperature, $N_C = 2(2\pi m_e kT/h^2)^{3/2}$ is the effective density of states in the conduction band, $N_V = 2(2\pi m_h kT/h^2)^{3/2}$ is the effective density of states in the valence band, h is Planck's constant, and m_e and m_h are the effective masses of electrons and holes, respectively.

The Fermi energy E_f required in Eqs. (2) and (3) can be derived from the condition of charge neutrality

$$n + N_a^- = p + N_d^+ . \quad (4)$$

For semi-insulating GaAs, Eq. (4) can be simplified because n and p are very small, typically on the order of 10^7 cm^{-3} , while N_d^+ and N_a^- are each on the order of the impurity density, which is higher than 10^{13} cm^{-3} . Therefore, n and p can be neglected in Eq. (4), and the condition of charge neutrality for semi-insulating GaAs becomes

$$N_a^- = N_d^+ \quad (5)$$

This simplification allows to calculate of the resistivity in two steps. In the first step the Fermi level is determined by Eq (5), neglecting the contribution of the free charge densities n and p because they are much smaller than the fixed charge densities N_a^- and N_d^+ . Once the Fermi level is determined, n and p are calculated from Eqs (2) and (3) and the resistivity is determined from Eq (1).

In order to solve Eq (5) exactly it would be necessary to consider all the impurity species present in the material. However, it is possible to assume, with little loss of generality, that one donor and one acceptor species are dominant, and neglect the contribution of any others to N_a^- and N_d^+ . With this assumption, substitution of the Fermi functions into Eq. (5) gives:

$$\frac{N_a}{1 + g_a \exp[(E_a - E_f)/kT]} = \frac{N_d}{1 + g_d \exp[(E_f - E_d)/kT]}, \quad (6)$$

where g_a and g_d are degeneracies, and E_a and E_d are the energies of the acceptor level and donor level respectively.

Eq. (6) can be solved for the Fermi energy E_f , which can then be substituted in Eqs. (1) to (3) to form an expression for the electrical resistivity. First, it is convenient to define

$$E_0 \equiv (E_d + E_a)/2 \quad (7)$$

$$G \equiv \exp[(E_0 - E_f)/kT] \quad (8)$$

Substituting E_0 and G , Eq. (6) becomes a quadratic equation for G . The solution is:

$$G = (1/2g_a) \left\{ - (1 - N_a/N_d) \exp \left[(E_d - E_a)/2kT \right] + \left[(1 - N_a/N_d)^2 \exp \left[(E_d - E_a)/kT \right] + 4(N_a/N_d)g_dg_a \right]^{1/2} \right\}. \quad (9)$$

Combining Eqs. (1) - (3) and Eqs. (7) - (9), the electrical conductivity ρ^{-1} becomes

$$\rho^{-1} = (q\mu_e N_c/G) \exp \left[-(E_c - E_0)/kT \right] + q\mu_h N_v G \exp \left[-(E_0 - E_v)/kT \right]. \quad (10)$$

Eqs. (9) and (10) express the electrical resistivity as a function of temperature, and the density, energy level and degeneracy of donors and acceptors. Notice that the use of Eq. (5) in the derivation has led to the donor and acceptor densities N_d and N_a appearing only as the ratio N_d/N_a .

Two alternative models for the impurity level scheme of Cr-doped semi-insulating GaAs will be considered. First, the conventional model in which the only deep level is an acceptor, and second, a more elaborate model is proposed in which there is both a deep donor level and a deep acceptor level.

A. Deep Acceptor Model

In this model, residual shallow impurities, which are mostly Si donors, are compensated by Cr acting as a deep acceptor. The acceptor density

N_a must always be larger than the residual donor density N_d , otherwise the Fermi level would lie close to the donor level and be near the conduction band. Fig. 3(a) describes the model. The density of free electrons, n , the density of free holes, p , the density of ionized donors, N_d^+ , and the density of ionized acceptors, N_a^- , are plotted in Fig. 3 on a logarithmic scale as functions of the position of the Fermi level in the bandgap. The Fermi level is at point F, the intersection of the curves for N_d^+ and N_a^- , to satisfy charge neutrality (Eq. (5)). The concentrations of free electrons n and free holes p are then represented by points N and P, respectively in Fig. 3(a).

Cr-doped semi-insulating GaAs can display either n- or p-type conduction at room temperature.^{6,7} It is difficult to account for such dual behavior with the deep acceptor model. Since the position of the Cr-acceptor level E_a is fixed, the only parameter varying from one crystal to another is the compensation ratio N_a/N_d . In principle, as N_a/N_d takes on different values, point F in Fig. 3(a) can move to different positions in the energy gap, making the electron and hole concentrations (points N and P in the figure) change in opposite directions, leading to electron or hole conduction dominance. In reality however, the range over which N_a/N_d may vary is narrow, only a few orders of magnitude, and is severely limited by practical restrictions on the concentrations of Cr that can be incorporated into the material due to the low distribution coefficient of Cr in GaAs.¹

For the analysis of some of the experimental results, an analytical expression for the electrical resistivity of n-type samples will be needed. Dropping the second term, the hole current, from the right hand side of Eq. (10) and also neglecting the second term in the square root of Eq. (9) since

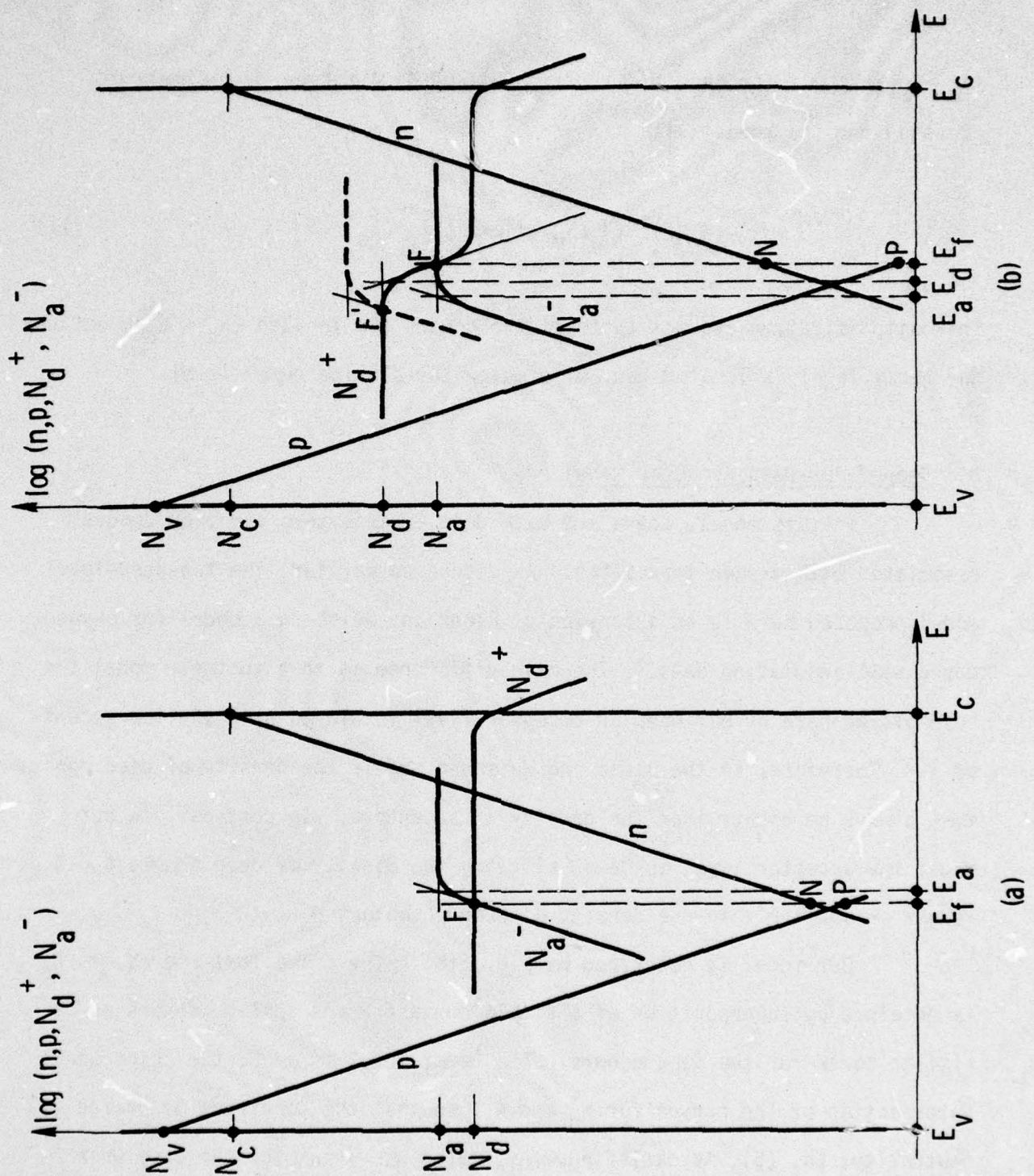


Fig. 3 Graphic representation of n , p , N_d^+ and N_a^- as functions of the position of the Fermi level in the energy gap; (a) for the deep-acceptor model, (b) for the deep-donor-deep-acceptor model.

$(E_d - E_a)/kT \gg 1$ for this model, Eqs. (9) and (10) reduce to a simple expression for the resistivity ρ

$$\rho (q\mu_e N_c g_a)^{-1} (N_a/N_d - 1) \exp \left[(E_c - E_a)/kT \right] . \quad (11)$$

This simplification assumes that all the donors are ionized ($N_d^+ \approx N_d$), because the Fermi level is located many kT 's below the shallow donor level.

B. Deep-Donor-Deep-Acceptor Model

In this model, there are both deep Cr acceptors and deep donors associated with oxygen impurities. As discussed earlier, the two-deep-level model proposed here is an extension of Blanc and Weisberg's model for oxygen doped semi-insulating GaAs.² The main difference is that in their model the role played here by our deep Cr-acceptor level is played by a shallow acceptor.^{2,3} Therefore, in the Blanc and Weisberg model, the density of deep donors must always be higher than the density of acceptors. In contrast, in our model the acceptor level is deep, allowing the density of deep donors N_d to be larger or smaller than the density of deep acceptors N_a .

Our model is described by Fig. 3(b). The curve that represents N_d^+ is obtained by superposition of a simple curve for the shallow donors and a similar curve for the deep donors. The Fermi level is at F, the point of intersection of the curves for N_d^+ and N_a^- , so that the condition of charge neutrality, Eq. (5), is satisfied. Fig. 3(b) was drawn for the case when $N_d > N_a$. In this case, the Fermi level (point F) is above E_d in the energy gap, its position depending on the ratio between the densities of deep donors

and deep acceptors N_d/N_a . The case when $N_a > N_d$ can be visualized in Fig. 3(b) by raising the curve that represents N_a^- above that for N_d , to the position shown with a dashed line. The intersection of N_d^+ and N_a^- , which again determines the Fermi level, is now at F' below E_a in the energy gap. Therefore, depending on whether $N_d > N_a$ or $N_a > N_d$, the Fermi level may move from above E_d to below E_a . The range over which the Fermi level may vary as a function of realistic impurity concentrations is broader than in the former model, making this model more suited for explaining the existence of either n- or p-type Cr-doped semi-insulating material.

For the analysis of some of the experimental results, an expression for the electrical resistivity of n-type material will be needed as with the previous model. The only simplification of Eqs. (9) and (10) without loss of generality is dropping of the second term from the right hand side of Eq. (10). However, in the limiting cases when either $N_a \gg N_d$ or $N_d \gg N_a$, the second term in the square root of the right hand side of Eq. (9) can be considered of second order with respect to the first. Retaining only first order terms in Eq. (9), and substituting into Eq. (10), leads to

$$\rho = (q\mu_e N_c g_a)^{-1} (N_a/N_d - 1) \exp \left[(E_c - E_a)/kT \right] ; N_a \gg N_d \quad (12)$$

$$\rho = (q\mu_e N_c)^{-1} g_d (N_d/N_a - 1)^{-1} \exp \left[(E_c - E_d)/kT \right] ; N_d \gg N_a. \quad (13)$$

These simplifications assume that all the donors are ionized ($N_d^+ \approx N_d$) when $N_a \gg N_d$ or that all the acceptors are ionized ($N_a^- \approx N_a$) when $N_d \gg N_a$. Eq. (12) is identical to Eq. (11) derived for the deep-acceptor model because

once we can assume that all the donors are ionized, the position of the Fermi level does not depend on whether the donors are deep or shallow.

Samples were prepared from three boules of single crystal Cr-doped semi-insulating GaAs each having a different Cr concentration. Table 3.2-4 in Ref. 1 shows the results of a mass spectrographic analysis of the two boules with the highest and lowest Cr concentration. The low-Cr samples contain $5 \times 10^{15} \text{ cm}^{-3}$ Cr atoms, which is near the threshold of Cr concentration required for high resistivity material. The high-Cr samples contain $5.8 \times 10^{16} \text{ cm}^{-3}$ Cr atoms, which we consider the upper bound for Cr concentration, since the high-Cr samples show incipient Cr precipitation in secondary ion mass spectroscopy measurements (see Section 3.2.3).⁸ The mid-Cr samples contain $1.2 \times 10^{16} \text{ cm}^{-3}$ Cr atoms, estimated from the amount of Cr added to the melt.

Room temperature measurements of resistivity and Hall constant were made on the high-, mid- and low-Cr samples, using a Van der Pauw configuration. Contacts were prepared by In evaporation through a mask and annealing (three minutes at 450°C in H_2 atmosphere). The current through the samples was measured with a Keithley 419 picoammeter and the voltage drops were measured with a Keithley 602 floating electrometer with input impedance and isolation higher than 10^{12} ohms. Precautions were taken to insure good shielding without ground loops in the system. For the highest values of sample impedance it was verified that no significant amount of current was diverted from the sample through the voltage sensing electrometer.

Table I summarizes the results of room temperature resistivity-Hall measurements on the three types of material. All the samples have high resistivity, between 3.4×10^8 ohm-cm and 1.1×10^9 ohm-cm. The low-Cr material

TABLE I: Results of Resistivity-Hall Measurements at Room Temperature.

	Low-Cr Boule 1718	Mid-Cr Boule 2312	High-Cr Boule 2000
ρ (ohm-cm)	3.4×10^8	1.1×10^9	3.8×10^8
R_H (cm ³ C ⁻¹)	-1.8×10^{12}	-9.5×10^{11}	-1.2×10^{11}
μ_H (cm ² V ⁻¹ sec ⁻¹)	5200	850	320
Type	n	p	p
n (cm ⁻³)	3.6×10^6	9.2×10^5 *	4.6×10^5 *
p (cm ⁻³)		1.3×10^7 *	2.7×10^7 *
μ_e (cm ² V ⁻¹ sec ⁻¹)	5200	2500 *	5200 *
μ_h (cm ² V ⁻¹ sec ⁻¹)		250 *	520 *

* Calculated assuming $b = \mu_e/\mu_h = 10$

is n-type with a free electron density $n = 3.6 \times 10^{16} \text{ cm}^{-3}$. The Hall mobility $\mu_h = R_H/\rho$, which corresponds to electrons, is $5200 \text{ cm}^2/\text{V-sec}$.

The mid- and high-Cr materials have a negative Hall constant as if they were n-type with low apparent Hall mobility μ_H . The small values of μ_H are indications of mixed conduction. Therefore, the contribution of both electrons and holes must be taken into account. The expression for the Hall constant R_H at low magnetic field is

$$R_H = q^{-1}(p - nb^2)/(p + nb)^2, \quad (14)$$

where $b \equiv \mu_e/\mu_h$ is the ratio between electron and hole mobility. Given the experimental value of R_H , since p and n are related by the condition $np = n_i^2$ (n_i is the intrinsic carrier concentration⁹), Eq. (14) yields values of n and p , provided that b is known. Once n and p are determined, the mobilities can be calculated from the experimental value of the resistivity ρ by means of Eq. (1). Using for b the value $b = 10$ reported for semi-insulating GaAs,⁶ the values of n , p , μ_e and μ_h listed in Table I are obtained. If the resulting values for the high-Cr material are substituted into Eq. (1), the term $qp\mu_h$ becomes 6 times larger than $qn\mu_e$ showing that most of the current is carried by holes. Therefore, the high-Cr material is p-type despite the negative value of the Hall constant. The mid-Cr material is also p-type but $qp\mu_h$ is only 1.4 times larger than $qn\mu_e$. In summary, there is a gradual change from n-type to p-type conduction as the Cr concentration of the samples increases.

The resistivity of the samples was measured as a function of tem-

perature with the same instrumentation and procedure described above. The samples were kept under vacuum to reduce surface contamination when they were heated. Fig. 4 shows the resistivity of a low-, mid- and a high-Cr sample as a function of temperature. The resistivity decreases very rapidly when the temperature increases, to the extent that it falls into the $10^3 - 10^4$ ohm-cm range at 200°C .

The room temperature resistivity and Hall constant measurements described above showed that the low-Cr material was n-type while the high-Cr material, with one order of magnitude more Cr impurities, was p-type. The mid-Cr material had an intermediate behavior. This observation is in agreement with both models described earlier in this section because in both models an increase of the density of Cr acceptors tends to displace the Fermi level toward the valence band. In order to sort between the two models it is necessary to analyze the resistivity vs. temperature data.

Before employing Eqs. (9) to (13) to fit the ρ vs. T data, it is necessary to consider the implicit temperature dependence of the equations through the parameters N_c , N_v , μ_e , μ_h , E_d and E_a . The temperature dependence of N_c and N_v is just proportional to $T^{3/2}$. Therefore, the temperature dependence of N_c and N_v will be easily corrected for by plotting $\rho T^{3/2}$ instead of ρ . As to the mobilities μ_e and μ_h , Look⁶ observed that the Hall mobility of a Cr-doped semi-insulating GaAs crystal was constant in a temperature range similar to that of our experiment. Therefore, the assumption that such behavior applies to our samples as well is made and the mobilities μ_e and μ_h will be treated as temperature independent. Later in this section it will be shown that the errors this assumption may cause are tolerable for our purpose,

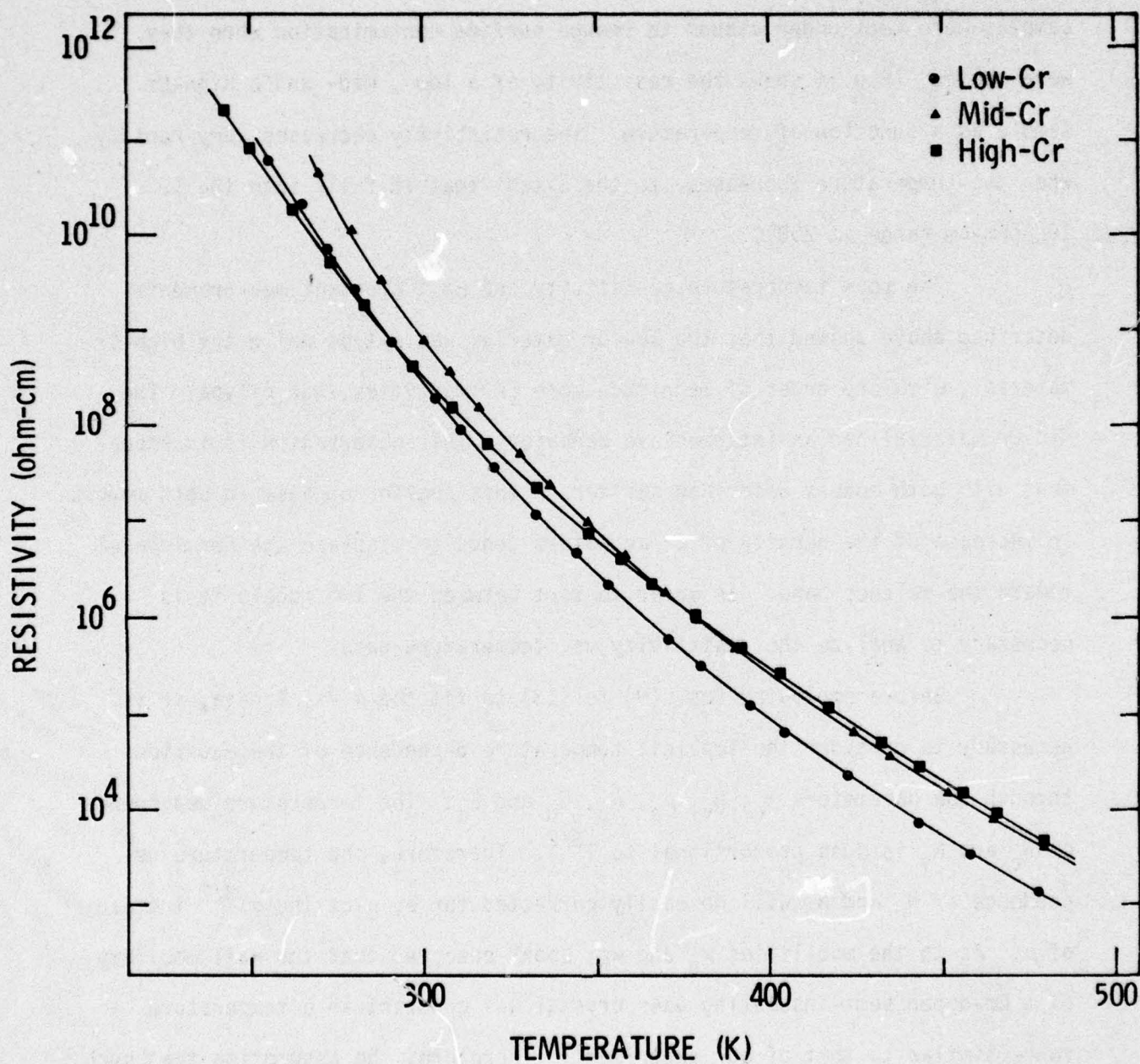


Fig. 4 Resistivity vs. temperature data for all the samples.

and therefore, a measurement of the temperature dependence of μ_e and μ_h is unwarranted.

The relative energy positions of the impurity levels $E_c - E_d$, $E_c - E_a$, $E_d - E_a$, etc. are subject to small temperature variations. The assumption that the energy separations of the deep levels from the band edges remain proportional to the energy gap as it changes with temperature is made. This is probably an oversimplification, but it is the best approximation lacking information on how deep levels in GaAs vary with temperature. Assuming the depth of the energy levels invariant with temperature would be appropriate only for shallow energy levels. In order to make this correction for the temperature variation of the energy levels, it is convenient to correct kT rather than the energies, taking advantage of the fact that the energy differences are always divided by kT in the equations. The temperature scale $T' = T E_g(298K)/E_g(T)$, where $E_g(T)$ is the bandgap energy, is introduced. When T' is used in place of T in the arguments of the exponential functions in Eqs. (9) to (13), the energy differences represent directly room temperature (298K) values. The expression $E_g(T) = 1.519 - 5.4 \times 10^{-4} T^2 / (T + 204K)$, from Ref. 10 is used to calculate T' .

The values of the degeneracy factors g_d and g_a for deep impurity levels in GaAs are not known. The frequently used values $g_d = 2$ and $g_a = 4$ apply only to shallow donors and acceptors since they are based on a hydrogenic model for the impurity states. For deep impurity levels, spin resonance information on the multiplicity of the ground state configuration is needed. Lacking sufficient information, we choose $g_d = g_a = 1$ with the understanding that our results can be easily corrected when values of g_d

and g_a become available.

A. Low-Cr Case

In comparing the low-Cr data of Fig. 4 with the predictions of the models, only the contribution of the electrons to the electrical conduction needs to be considered because the material is n-type as indicated by the Hall measurement (Table I). Under this circumstance, Eq. (11) subject to the condition $N_a > N_d$ applies for the deep-acceptor model, while Eqs. (12) and (13) apply for the deep-donor-deep-acceptor model. All three equations predict pure exponential behavior of the resistivity. The temperature corrections discussed earlier in this section are performed by replotting in Fig. 5 the data from Fig. 4 with new scales $\log \rho T^{3/2}$ and $1/T'$. A linear least square fit of the low-Cr data is shown with solid line in Fig. 5. The fit is excellent indicating that the criteria used in deriving the equations and correcting the data were appropriate. The low-Cr data are fit by

$$\rho = 1.08T^{-3/2}\exp(8380/T')\text{ohm-cm} \quad , \quad (14)$$

where T and T' are in degrees Kelvin.

Comparing Eq. (14) with Eqs. (12) and (13) for the deep-donor-deep-acceptor model, Eq. (13) becomes identical to Eq. (14) by choosing $N_d/N_a = 14$ and $E_c - E_d = 0.72$ eV. This is the situation described in Fig. 3(b), with the Fermi level at point F, near the deep donor level. It is also possible to make Eq. (11) for the deep-acceptor model identical to Eq. (14) by choosing $N_a/N_d = 1.07$ and $E_c - E_a = 0.72$ eV. This is approximately

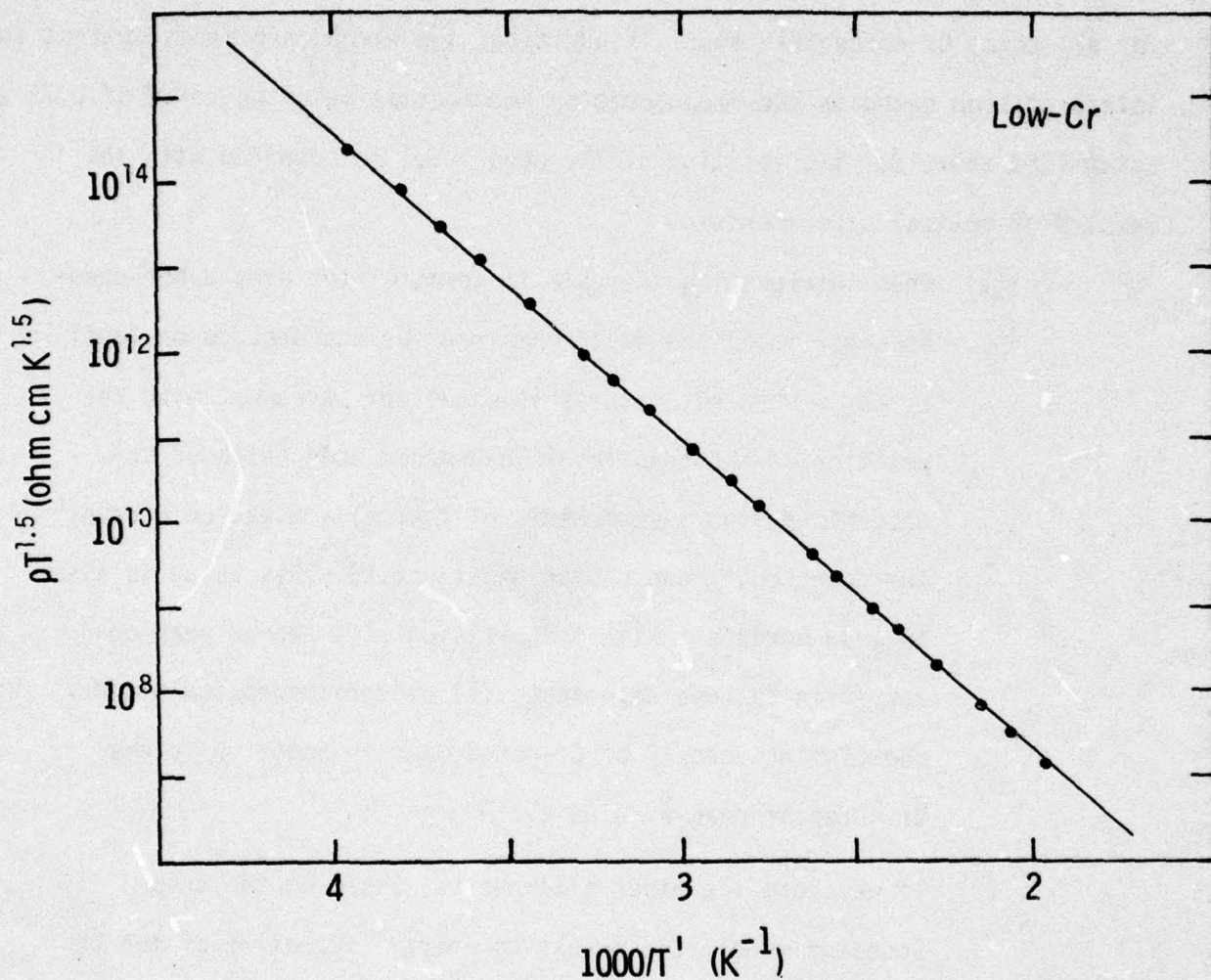


Fig. 5 Plot of $\rho T^{3/2}$ vs. $1/T'$ for the low-Cr data of Fig. 2. The temperature scale was corrected for the effect of the thermal variation of the energy gap, $T' = T E_g(298K)/E_g(T)$. The solid line is the result of a linear least square fit.

the situation described by Fig. 3(a), with the Fermi level, determined by point F, between the deep acceptor level and the conduction band. However, this alternative would not lead to a consistent interpretation of the results for all three Cr concentrations. In addition, two strong arguments against an interpretation based on the deep-acceptor model arise when the value of 0.72 eV determined above for the position of the deep level is compared with the results of optical experiments.

- (1) When interpreting the data in terms of the deep-donor-deep-acceptor model the depth obtained for the deep donor level, $E_c - E_d = 0.72$ eV, results in excellent agreement with the position of the deep level in 0-doped GaAs (without Cr), determined from measurements of thermal activation energy,³ luminescence,¹¹ and photocapacitance.¹² This value is also in good agreement with the position of a second peak observed in cathodoluminescence,¹³ electroabsorption¹⁴ and photoluminescence¹⁵ of Cr-doped GaAs in addition to the Cr acceptor peak at 0.84 eV.¹⁵
- (2) If we chose the other alternative, based on the deep-acceptor model, the resulting energy separation of the Cr-acceptor level from the conduction band, $E_c - E_a = 0.72$ eV, would be too low compared with the depth of the Cr level of 0.84 eV determined by photoluminescence,¹⁵ photoconductivity^{16,17} and optical absorption.¹⁸

B. Mid-Cr Case

Since the mid-Cr material exhibits mixed conduction (see Table I),

the full expression of the resistivity given by Eqs. (9) and (10) must be used, requiring a non-linear least square fitting procedure. The procedure to find the optimum fit to $\log \rho T^{3/2}$ vs. $1/T$ is the following. After replacing, in Eqs. (9) and (10), the numerical values of N_C and N_V and the mobilities (Table I), and assuming $g_d = g_a = 1$, a fit is made using N_a/N_d and $E_C - E_a$ as the adjustable parameters for a given value of $E_C - E_d$. A sequence of fits is made to find the value of $E_C - E_d$ which gives the minimum error. The excellent fit shown in Fig. 6 is obtained with $E_C - E_d = 0.64$ eV, $N_a/N_d = 0.98$ and $E_C - E_a = 0.90$ eV. The value $E_C - E_a = 0.90$ eV is 0.06 eV higher than the energy of the Cr level determined by optical experiments.¹¹⁻¹⁸ The value of $E_C - E_d$ is 0.06 eV lower than the value determined in the low-Cr case. We regard such differences a measure of the overall error margin of this work, a margin that is considered satisfactory given the simplifying assumptions on the temperature dependence of some of the parameters and on the degeneracy of the levels.

Fig. 7 shows how the results of the non-linear fit procedure depend on the value assigned to $E_C - E_d$. The mean square deviation ϵ is plotted against $E_C - E_d$ along with the resulting values of N_a/N_d and $E_C - E_a$. The curve for ϵ shows how sensitive the fit is to the position of the donor level. The minimum for ϵ at $E_C - E_d = 0.64$ eV proves that for a good fit of the experimental data, the deep-donor-deep-acceptor model must be used. If $E_C - E_d \sim 0$ were chosen in Fig. 7 (i.e., shallow donors), which is the assumption of the deep-acceptor model, the error ϵ would increase by a factor of almost two and $E_C - E_a$ would become incompatible with the optical data on the Cr level.^{15,18}

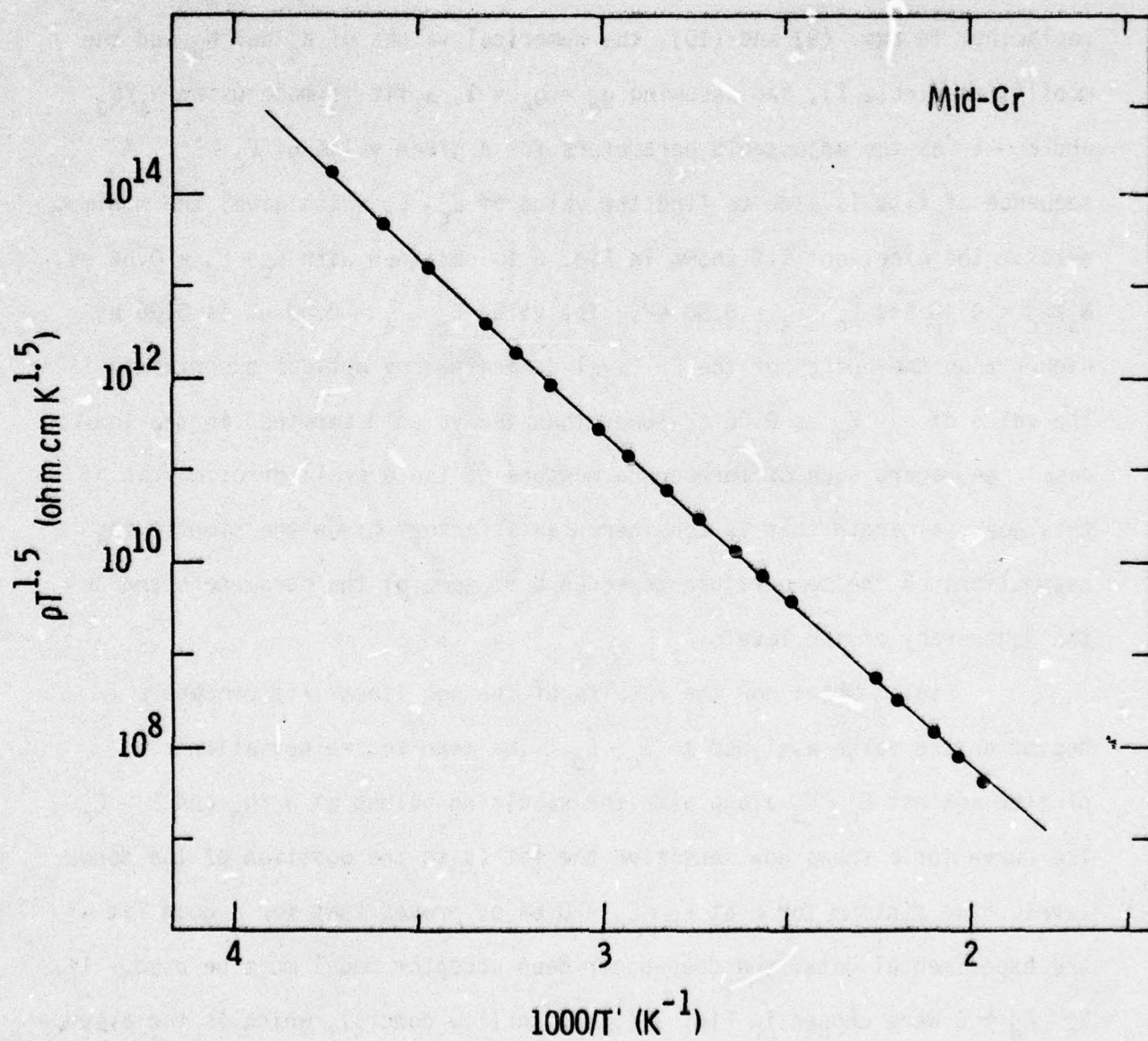


Fig. 6 Result of a non-linear least square fit of the mid-Cr data for $E_c - E_d = 0.64$ eV. Fitting parameters: $N_a/N_d = 0.98$; $E_c - E_a = 0.90$ eV. The dots represent the experimental points.

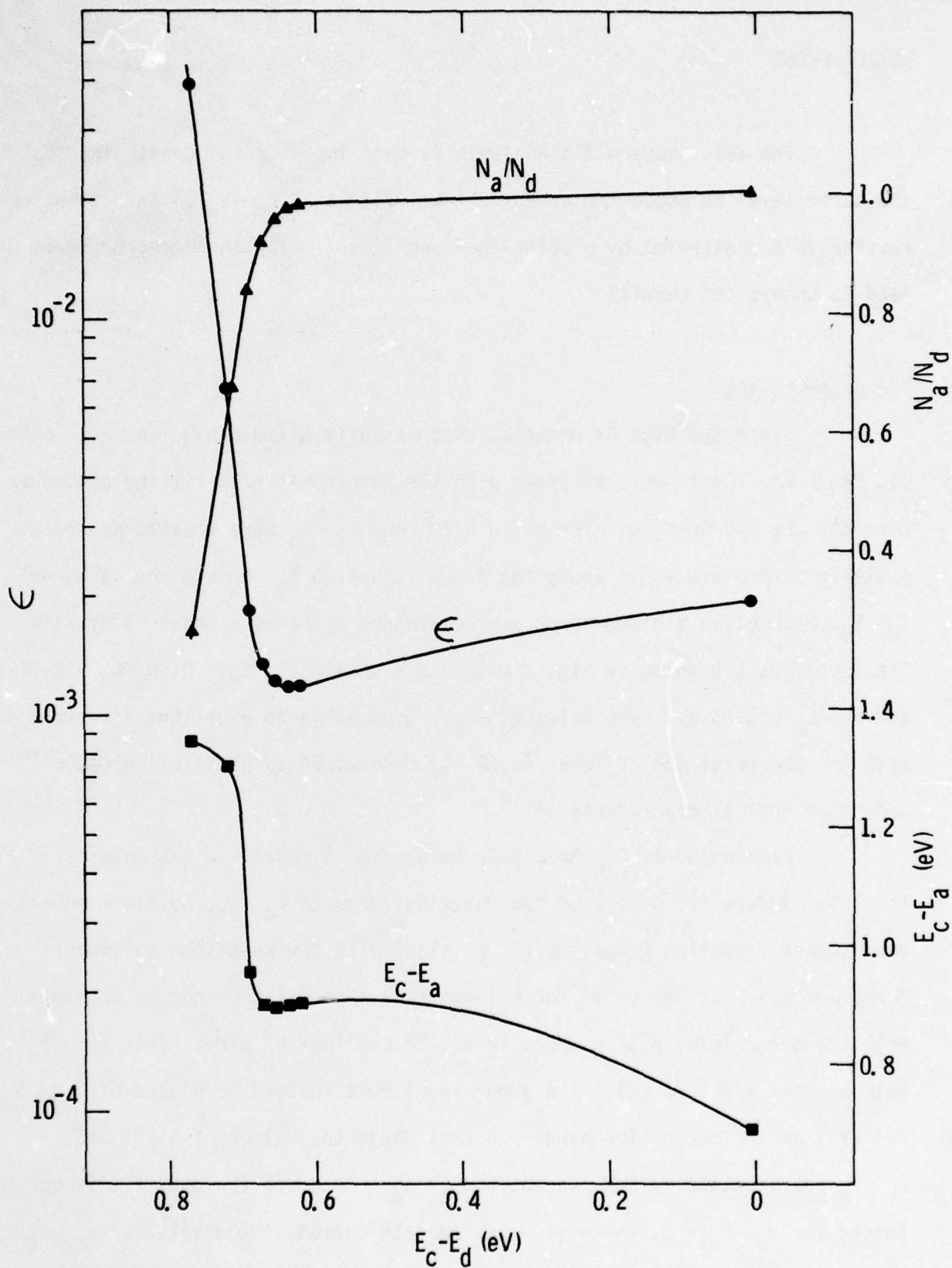


Fig. 7 Plot of the mean square error ϵ and the fitting parameters N_a/N_d and $E_c - E_a$ against the parameter $E_c - E_d$ in the non-linear least square fit of the mid-Cr data.

The least square fit analysis is done imposing the constraint that the donor level be above the acceptor level ($E_C - E_d \leq E_C - E_a$). An attempt to reverse this constraint by placing the donor level below the acceptor level lead to unphysical results.

C. High-Cr Case

Since the high-Cr material also exhibits mixed conduction (see Table I), the ρ vs. T data were analyzed with the same non-linear fitting procedure used for the mid-Cr case. The ratio N_a/N_d and $E_C - E_a$ were treated as the adjustable parameters while assigning fixed values to $E_C - E_d$ and the value of $E_C - E_d$ which gives minimum error was determined by doing a sequence of fits. The excellent fit shown in Fig. 8 was obtained with $E_C - E_d = 0$, $N_a/N_d = 1.04$ and $E_C - E_a = 0.83$ eV. The value $E_C - E_a = 0.83$ eV is in excellent agreement with the energy of the Cr level (0.84 eV) determined by photoluminescence,¹⁵ and other optical experiments.¹⁶⁻¹⁸

Proceeding as in the mid-Cr case, Fig. 9 shows how the results of the least square fit depend on the value assigned to $E_C - E_d$, by plotting the mean square deviation ϵ against $E_C - E_d$ along with the resulting values of N_a/N_d and $E_C - E_a$. The curve for ϵ shows that a good fit cannot be obtained with the donor level placed where it was in the low- or mid-Cr case ($E_C - E_d$ between 0.64 and 0.72 eV). The donor level must instead be placed within 0.4 eV from the conduction band. In this range the values of N_a/N_d and $E_C - E_a$ are practically independent of $E_C - E_d$. Although the best fit is obtained for $E_C - E_d = 0$, there is some indetermination in the value of $E_C - E_d$ because the curve for ϵ in Fig. 9 has almost zero slope near $E_C - E_d = 0$. It

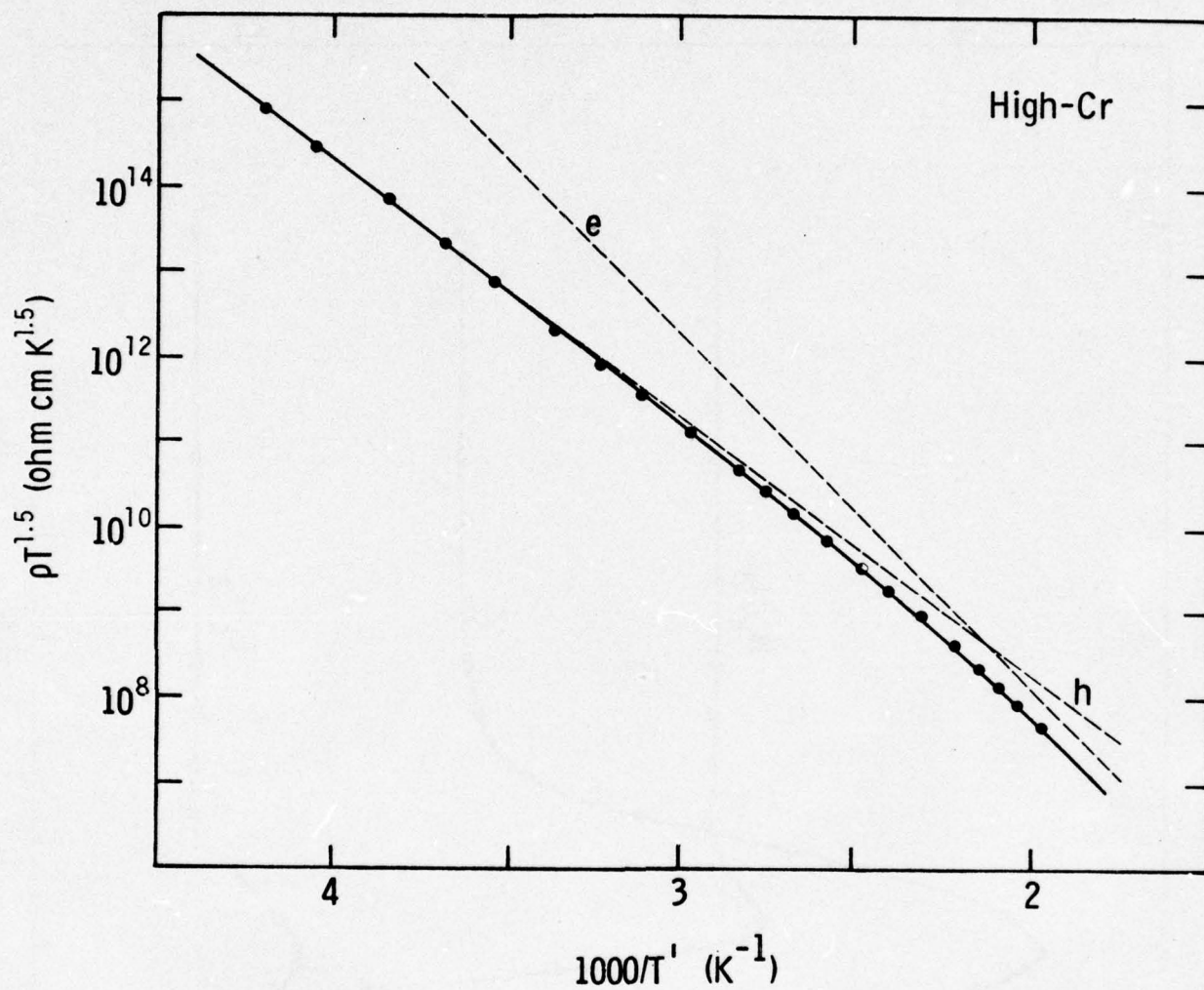


Fig. 8 Result of a non-linear least square fit of the high-Cr data for $E_c - E_d = 0$. Fitting parameters: $N_a/N_d = 1.04$; $E_c - E_a = 0.83$ eV. The dots represent the experimental points. The dashed lines represent the separate contributions of electrons and holes.

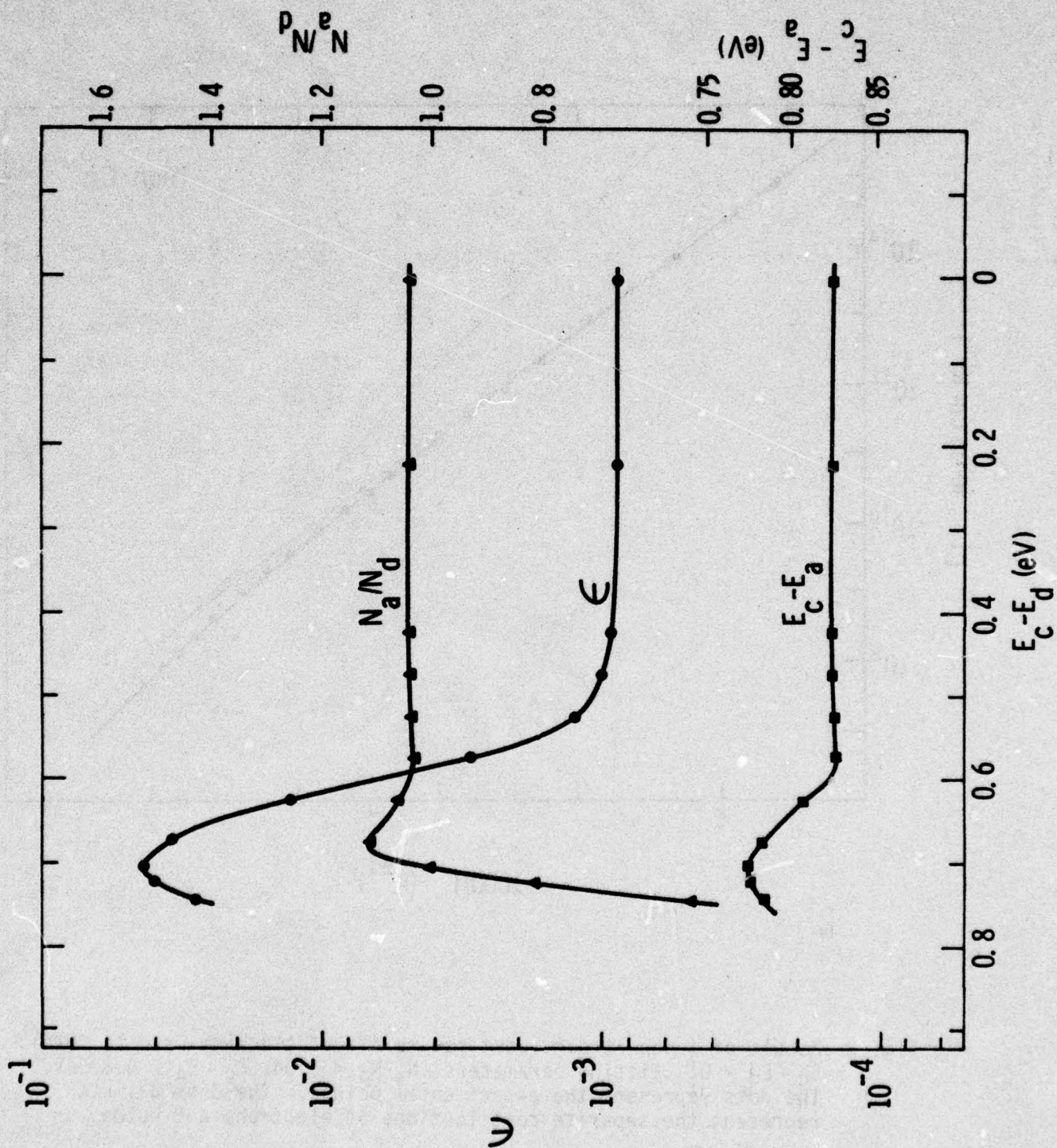


Fig. 9 Plot of the mean square error ϵ and the fitting parameters N_a/N_d and $E_c - E_a$ against the parameter $E_c - E_d$ in the non-linear least square fit of the high-Cr data.

was verified that changing the values of the mobilities within reasonable limits does not alter the conclusion that $N_a/N_d > 1$ or the conclusion that the donors are located within 0.4 eV from the conduction band where the curves in Fig. 9 are almost flat.

The analysis of the low- and mid-Cr data clearly supports the deep-donor-deep-acceptor model. In contrast, the high-Cr case is better described by a deep acceptor level compensating donors, which are shallower than in the low- and mid-Cr cases. Not being aware of any deep donor species within 0.4 eV from the conduction band, we believe that the donor level is shallow. We conclude that there is a large difference in the relative density of deep and shallow donors between the low- and mid-Cr and the high-Cr material. There is no evidence to support this interpretation in the mass spectrographic data on Si and O concentration (Table 3.2-4 in Ref. 1) in the samples. However, there may well be impurity complexes that are lowering the density of electrically active impurities,¹ or precipitates⁸ in which fractions of some impurities are segregated, or a combination of both.

In summary, it has been shown that with some knowledge of the material composition and of impurity energy levels, it is possible to interpret and model the electrical compensation of semi-insulating GaAs by means of ρ vs. T measurements. Semi-insulating GaAs crystals with low- and high-Cr concentration have been compared. The interpretation of the data from the low- and mid-Cr material requires a deep donor level located between 0.64 and 0.72 eV from the conduction band. The presence of this deep donor level implies that the "conventional" model with deep Cr acceptors compensating residual shallow donors is not correct. A three level model for Cr-doped

semi-insulating GaAs was proposed, the three levels being the residual shallow donor and deep Cr acceptor levels, plus an additional deep donor level. This model can interpret all the experimental data. Based on comparisons with O-doped GaAs, it was proposed that the deep donor level was associated with oxygen impurities.

3.2.2 Effects of Heat Treatment on Semi-Insulating GaAs - Science Center

GaAs substrates with low resistivity can usually be heated in epitaxial growth furnaces until they reach the required growth temperature without suffering appreciable changes of their electrical properties. Semi-insulating substrates are much more sensitive to such heat treatments because they are compensated semiconductors. In fact, it has been shown that even moderate heat treatment cycles similar to those that take place in liquid phase epitaxial growth may, in some cases, lower the sheet resistance of semi-insulating substrates by several orders of magnitude¹ producing disastrous effects on the performance of microwave FET devices.

The study of low resistivity surface layers formed by heat treatment of Cr-doped semi-insulating GaAs in H₂ atmosphere has been continued. Information has been derived by combining electrical measurements with photoluminescence measurements.

Samples from several boules of Cr-doped semi-insulating GaAs supplied by Crystal Specialties have been tested. The Cr concentration ranged from $8 \times 10^{14} \text{ cm}^{-3}$ to $5 \times 10^{17} \text{ cm}^{-3}$. The samples were polished, cleaned, chemically etched to remove damage, and finally annealed for 2 hours at a temperature of 750°C. This heat treatment was done in a furnace normally used for liquid

phase epitaxial growth which was continuously flushed with purified H_2 . Notice the precaution to simulate both the substrate preparation procedures and the heat treatment conditions typical of liquid phase epitaxial growth.

Concentric Al contacts with the dimensions shown in the insert of Fig. 10 were evaporated in order to measure I-V characteristics for the heat treated samples. For all but a few of the high resistance samples, the shapes of the I-V characteristics could be identified as those of two back to back diodes of different area with large series resistance. Sheet resistances were calculated based on the contact dimensions and the resistance values determined from the I-V characteristics. For comparison, the same measurements and calculations were made for the untreated and high resistance samples, neglecting bulk effects. The procedure of using evaporated Al contacts originally proposed by Barrera¹⁹ has been improved by using more sensitive instrumentation, so that small changes of resistivity could be detected.

In Fig. 10 the sheet resistivity of the samples after heat treatment was plotted against Cr concentration. The data points are clustered, indicating that there is no correlation between sheet resistivity and Cr-concentration. For boules 2312 and 2638 two data points each are plotted because different wafers yielded different sheet resistances. This is an indication of inhomogeneity. The dramatic difference between two wafers of boule 2638 is probably associated with the very low Cr concentration in that boule.

The low resistivity layers formed were p-type. This was determined from the asymmetric shapes of the I-V characteristics. This conclusion was also verified for some of the more conductive samples by Hall measurements

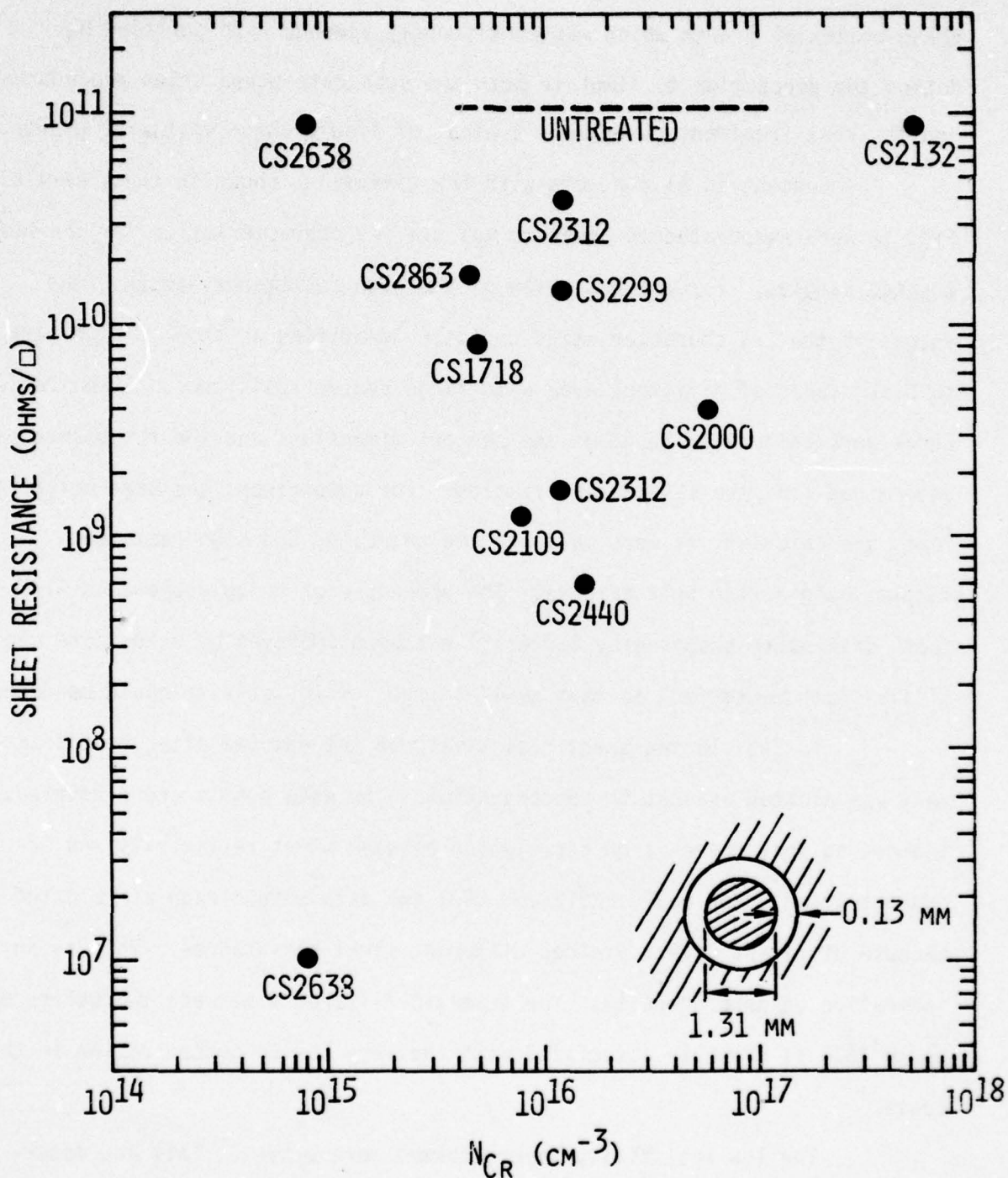


Fig. 10 Sheet resistance as a function of the Cr concentration for several samples (identified by boule numbers) heat treated at 750°C for 2 hrs. in H_2 atmosphere. The Al contact pattern used for the measurement is shown in the insert.

and by the polarity of the I-V characteristics of a point probe between the surface of the sample and an ohmic contact.

Photoluminescence measurements at 77K have been presented in an earlier report. The weak luminescent emission at 1.508 eV (corresponding to the energy gap) was greatly enhanced by annealing. In addition, a broad peak appeared at 1.39 eV in all samples after heat treatment. Both peaks were larger in the samples that display larger decrease of sheet resistance after heat treatment. The direct correlation between decrease of resistivity and increase of photoluminescence intensity in the heat treated material is demonstrated in Fig. 11. This figure represents the intensity of the luminescence peaks and the sheet resistance as functions of the thickness of material removed in sequential etching steps. When sufficient material was removed, the sheet resistance and photoluminescence intensities recovered their normal values as in untreated material. The depth of the low resistivity layer is on the order of $0.3\mu\text{m}$.

The two peaks in the 77K photoluminescence spectra of the heat treated samples can be resolved by lowering the measurement temperature. Fig. 12 shows the photoluminescence spectrum at 25K for the heat treated sample of Fig. 11. In the gap region it is now possible to distinguish the free exciton recombination peak at 1.514 eV signaling the position of the energy gap^{20,21} and a large peak at 1.491 eV. The energy of this peak, 27meV lower than the gap energy, is characteristic of conduction band to acceptor recombination or exciton bound to acceptor recombination.²² The observation of a prominent acceptor peak in the photoluminescence spectrum is in agreement with the p-type behavior of the low resistivity surface layer. This

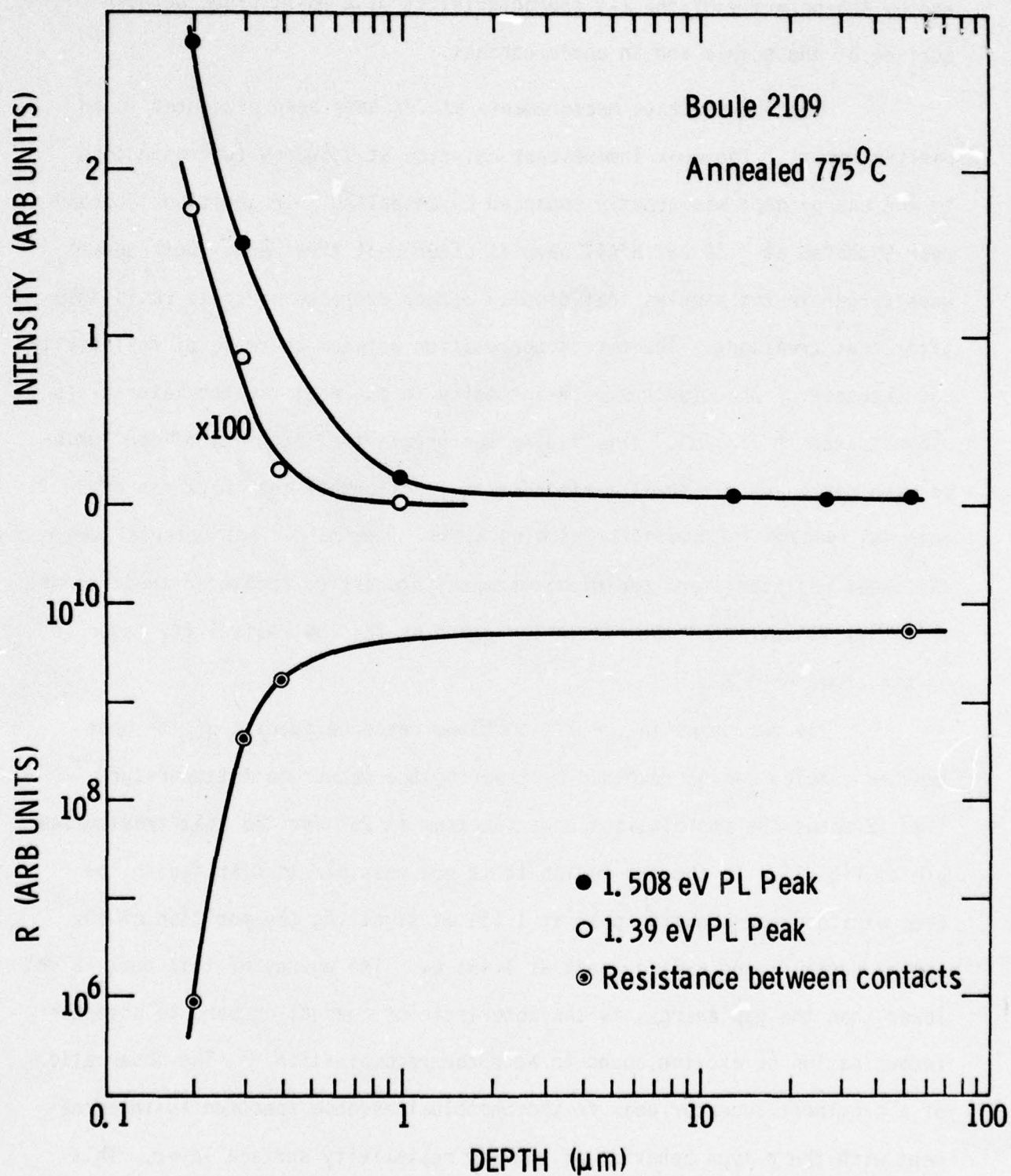


Fig. 11 Intensity of the photoluminescence peaks (at 77K) and resistance between two contacts as functions of the thickness of material removed by sequential etching.

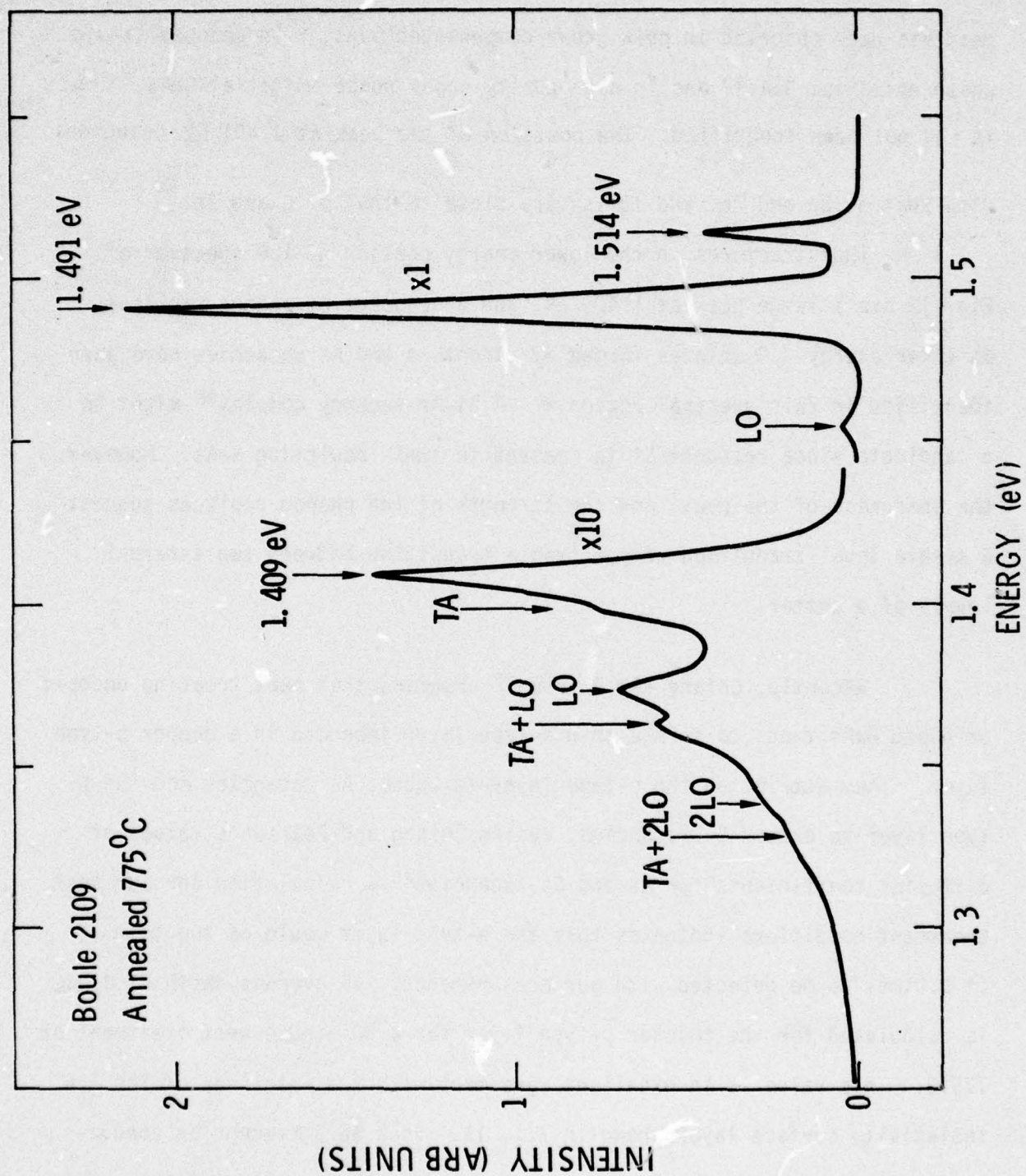


Fig. 12 Photoluminescence of a heat treated sample from boule 2109 measured at 25K.

peak has been observed in bulk grown compensated GaAs,²¹ in undoped liquid phase epitaxial GaAs²³ and in high purity vapor phase epitaxial GaAs,²⁴ but it had not been identified. The position of the peak at 1.491 eV coincides with that of Be and Zn, and it is very close to that of C and Zn.²⁵

The structures in the lower energy portion of the spectrum of Fig. 12 are a large peak at 1.409 eV, and a sequence of phonon replicas at lower energy. Complexes formed by acceptors and As vacancies have been identified in this spectral region.²² A Si-As vacancy complex²⁶ might be a candidate since residual Si is present in semi-insulating GaAs. However, the sharpness of the peak, and the strength of the phonon replicas suggest a single level transition rather than a transition between two internal levels of a center.

Recently, Chiang and Pearson²⁷ observed that heat treating undoped or doped GaAs tends to form a thin n-type layer imbedded in a deeper p-type layer. They attributed the n-type layer to excess As vacancies and the p-type layer to excess Ga vacancies. Using Chiang and Pearson's values of diffusion coefficients for As and Ga vacancies²⁸ a calculation for our heat treatment conditions indicates that the n-type layer would be too thin ($\sim 0.01\mu\text{m}$) to be detected with our measurements. An average depth of $0.3\mu\text{m}$ is calculated for the thicker p-type layer for a 90 minute heat treatment at 775°C . This value is in excellent agreement with the thickness of the low resistivity surface layer shown in Fig. 11. Such an agreement on conductivity type and thickness leads us to attribute the formation of the p-type surface layer in semi-insulating GaAs to a mechanism similar to that of un-

doped GaAs, which according to Chiang and Pearson, consists of formation and diffusion of Ga Vacancies.²⁷ It must be borne in mind, however, that vacancies can explain only the general trend of formation of a low resistivity layer on the heat treated material, but not the differences between samples from different boules. The existence of a range of sheet resistances produced by identical heat treatments (Fig. 10) indicates certain degrees of vacancy compensation which may be due to formation or dissociation of complexes. This problem required further investigation.

When the results of the heat treatment procedure shown in Fig. 10 were compared with those of the qualification test developed for ion implantation (See Section 5.9), it was found that these tests were not equivalent. The material which shows little conversion during heat treatment in H_2 atmosphere will not necessarily withstand the heat treatment of post implantation anneal. In fact, boules 2132 and 2299, which showed little drop of sheet resistance in Fig. 10, were rejected for implantation while exactly the opposite occurred with boules 2000, 2109 and 2440. The fact that substrates suitable for epitaxial growth and for ion implantation may not be exchangeable is understandable in light of the different heat treatment temperatures and the fact that a protective cap is used in the post-implantation anneals.

3.2.3 Study of Inclusions in Semi-Insulating GaAs - Cornell University

Preliminary observations of inclusions in semi-insulating GaAs were discussed in a previous report.⁸ Submicron inclusions of Si and Cr were found using a secondary ion mass spectrometer (SIMS).

More samples supplied by Crystal Specialties with a wide range of Cr concentration were analyzed with the SIMS. Heavily chromium-doped substrates showed submicron chromium inclusions, while corresponding inclusions were not observed in samples with $1 \times 10^{16}/\text{cm}^3$ or less chromium concentration. The Si inclusions were present in most samples. However, in substrates with extremely low Cr concentration ($N_{\text{Cr}} < 10^{15} \text{cm}^{-3}$), the silicon inclusions were nearly eliminated. This low level of Si inclusions is probably related to the fact that the overall Si content of the sample must be low in order to be electrically compensated with such a low Cr concentration.

SIMS measurements were made to study the effects of heat treatment. Samples were examined with the SIMS, heat treated for 10 hours in H_2 atmosphere at 700°C and reexamined under the SIMS. Substrates heavily doped with Cr ($N_{\text{Cr}} > 10^{17} \text{cm}^{-3}$), showed a large accumulation of chromium on the surface after heat treatment. This did not occur on substrates with lower doping ($N_{\text{Cr}} < 5 \times 10^{16} \text{cm}^{-3}$).

4.0 EPITAXIAL MATERIAL GROWTH AND CHARACTERIZATION

The LPE growth investigations under this contract involve two projects, one carried out at Stanford University, and the other at Cornell University. Epitaxial growth is also carried out at the Science Center but this activity will not be discussed during this reporting period since it involved only "routine" growth of FET active layers for device fabrication. The growth procedure developed at the Science Center was described in a previous report.¹

Stanford's work has had, since the inception of the contract, the primary goal of growing high resistivity ($> 10^4$ ohm-cm) epitaxial layers for potential use as a substrate buffer for active device layers and for the purpose of providing well-known, characterized layers for implantation studies. Crucial to achieving this goal is an understanding of the interactions between the growth system components, the melt bakeout temperature, the chemical composition of the melt, and subsequent impurity incorporation in the layer. Based on an understanding of these interrelated factors, the Stanford approach has been to control the chemical composition of the melt through a series of systematic bakeouts at a specific temperature and to use Cr to help chemically and electrically compensate donor and acceptor species. Layers exceeding resistivities of 10^4 ohm-cm have been produced in a $\text{SiO}_2\text{-BN(C)-H}_2$ system. In this report, the results of the study of a system in which the presence of C has been completely eliminated are presented and compared with those of other systems. Transient capacitance measurements were used to study the interface effects of active FET layers. No detectable traps were found in active layers grown on buffer layers in contrast with trapping effects observed when

the active layer was grown directly on the semi-insulating substrate.

At Cornell University the goal is to grow buffered layer FET structures using approaches different from those used at both the Science Center and Stanford. Active layers are grown in a more conventional manner to facilitate the incorporation of buffer layer growth. The Cornell approach for buffers is to use high purity undoped layers rather than high resistivity compensated layers as grown at Stanford. Growth of high purity undoped buffer layers with an estimated net hole concentration of $2 - 4 \times 10^{13} \text{ cm}^{-3}$ in a Spectro-sil quartz boat is reported. Graphite boats surface treated to reduce out-gassing are compared with ordinary graphite boats.

4.1 Growth and Evaluation of Semi-Insulating Liquid Phase Epitaxial GaAs - Stanford University

This research program is aimed at establishing parameters (temperature, dopants, distribution coefficients, etc.) necessary for the growth of thin GaAs layers having high sheet resistance ($\approx 10^5 \text{ ohm}/\square$) on semi-insulating GaAs substrates by means of liquid phase epitaxial (LPE) techniques. Since the high resistivity epitaxial layers can only be obtained at a critical temperature in a particular growth system, different materials in the system are being investigated to broaden the transition temperature range. In addition, the electrical properties of these layers are being measured in order to study the electron transport mechanisms and to provide information for device applications.

A. Growth Studies

During the past six months, the work was concentrated on finding

the bakeout transition temperature for a fused quartz-pyrolytic boron nitride-hydrogen system. Growth series #1700 (see Table II) was carried out at a bakeout temperature of 850°C and a bakeout period of 15 hours between each growth. P-type layers with carrier densities of $1 \times 10^{15} \text{ cm}^{-3}$ were obtained after an accumulated 30 hours of bakeout. When 0.5 atomic % of Cr was added to the same melt, the layers showed no change in their electrical properties. In growth series #1800 (see Table III), layers were grown from a melt baked out at temperatures between 790 to 750°C. After 30 hours of accumulated bakeout, all grown layers were p-type and carrier densities were in the range of $3 \times 10^{14} \text{ cm}^{-3}$. In Growth series #1900 (see Table III) the first layer, grown from a fresh melt without bakeout, was n-type with a carrier density of $6 \times 10^{14} \text{ cm}^{-3}$. When the accumulated bakeout period exceeded 30 hours at 700°C, the grown layers were p-type and had carrier densities in the range of $2 \times 10^{14} \text{ cm}^{-3}$. When the same melt was later baked out at 700°C for 15 hours with a graphite lid placed on the BN growth cell, the grown layer (#1907) was n-type and had a carrier density of $3.4 \times 10^{15} \text{ cm}^{-3}$. This result indicates that graphite introduces shallow donor impurities into the melt during the bakeout and growth steps. Growth series #2000 (see Table IV) was carried out at a bakeout temperature of 600°C. Layers grown in this series were all n-type. The stabilized melt (after 75 hours of accumulated bakeout) yielded layers with electron densities in the range of $2 \times 10^{14} \text{ cm}^{-3}$. In growth series #2100 (see Table V), layers were grown from a melt baked out at 675°C. After an accumulated bakeout time of 60 hours, the layers grown from the undoped melt had carrier densities ranging from 2.4 to $7.8 \times 10^{13} \text{ cm}^{-3}$. Three layers (#2105, #2107, and #2108) were n-type and one layer (#2106) was p-type with a resis-

TABLE II: Properties of Epitaxial GaAs Layers Grown in a SiO₂-BN-H₂ System
Growth Series #1700

Growth Conditions: Bakeout Temperature: 850°C; Bakeout Period: 15 hrs.
 Growth Temperature: 700°C; Cooling Rate: 4.5°C/min.
 H₂ Flow Rate: 0.6 l/min.

Growth No.	Dopant	Mobilities @ 300/77K (cm ² /V-sec)	Carrier Densities @ 300/77K (cm ⁻³)	Resistivity @ 300K (ohm-cm)	Conductivity Type
1701	-	5,700/39,000	3.5/3.0x10 ¹⁴	3.1	n
1702	-	1,350/-	1.2x10 ¹⁵ /-	3.8	n
1703	-	460/-	1.1x10 ¹⁵ /-	12	p
1704	-	450/5,700	2.9/1.4x10 ¹⁵	5	p
1705	-	400/5,300	2.6/1.3x10 ¹⁵	6	p
1706	-	(Grown on n ⁺ substrate)			
1707	-	350/4,500	2.7/1.0x10 ¹⁵	7	p
1708	Cr. (0.5 atm %)	350/-	4.8x10 ¹⁴ /-	37	p
1709	"	280/4,100	2.1x10 ¹⁵ /8.0x10 ¹⁴	11	p
1710	"	380/5,400	1.9x10 ¹⁵ /8.5x10 ¹⁴	9	p
1711	"	(Grown on n ⁺ substrate)			
1712	"	400/4,800	1.9/1.0x10 ¹⁵	9	p

TABLE III: Properties of Undoped Epitaxial Layers Grown in a SiO₂-BN-H₂ System
Growth Series #1800 and 1900Growth Conditions: Growth Temperature: 700°C; Cooling Rate: 4.5°C/min.
H₂ Flow Rate: 0.6 g/min.

Growth No.	Bakeout Temperature (°C)/Period (hr.)	Mobilities @ 300/77K (cm ² /V-sec)	Carrier Densities @ 300/77K (cm ⁻³)	Resistivity @ 300K (ohm-cm)	Conductivity Type
1801	790/1	2,000/5,100	1.8/1.4x10 ¹⁴	17	n
1802	790/15	1,500/13,000	3.0/2.5x10 ¹⁴	14	n
1803	790/15	380/5,500	2.0/1.9x10 ¹⁴	82	p
1804	790/15	460/8,000	3.2/2.8x10 ¹⁴	43	p
1805	780/15	530/ -	5.7x10 ¹⁴ / -	21	p
1806	780/15	470/6,100	2.4x1.4x10 ¹⁴	56	p
1807	780/15	510/11,000	1.8/1.5x10 ¹⁴	87	p
1808	770/15	380/6,600	3.0/2.3x10 ¹⁴	56	p
1809	750/15	340/6,100	3.5/2.5x10 ¹⁴	52	p
1901	-	6,100/56,000	6.0/5.4x10 ¹⁴	2	n
1902	750/15	5,100/ -	9.4x10 ¹³ / -	13	n
1903	700/15	6,400/59,000	2.0/1.8x10 ¹⁴	5	n
1904	700/15	400/9,000	2.2/1.7x10 ¹⁴	70	p
1906	700/15	190/ -	3.7x10 ¹⁴ / -	91	p
1907 *	700/15	6,300/34,000	3.4/2.8x10 ¹⁵	0.3	n

* A graphite lid was placed over the BN crucible.

TABLE IV: Properties of Undoped Epitaxial GaAs Layers Grown in a SiO₂-BN-H₂ System
Growth Series #2000

Growth Conditions: Bakeout Temperature: 600°C; Bakeout Period: 15 hrs.
Growth Temperature: 700°C; Cooling Rate: 4.5°C/min.
H₂ Flow Rate: 0.6 l/min.

Growth No.	Mobilities @ 300/77K (cm ² /V-sec)	Carrier Densities @ 300/77K (cm ⁻³)	Resistivity @ 300K (ohm-cm)	Conductivity Type
2001	6,300/66,000	7.7/7.3x10 ¹⁴	1.3	n
2002	6,500/63,000	6.3/5.9x10 ¹⁴	1.5	n
2003	6,600/83,000	3.4/3.4x10 ¹⁴	2.8	n
2004	6,000/67,000	2.9/3.2x10 ¹⁴	3.6	n
2005	6,500/67,000	4.2/4.0x10 ¹⁴	2.3	n
2006	6,000/74,000	1.9/1.9x10 ¹⁴	5.5	n
2007	6,000/77,000	1.9/2.0x10 ¹⁴	5.5	n
2008	6,300/78,000	2.4/2.3x10 ¹⁴	4.2	n
2009	6,400/83,000	1.8/1.9x10 ¹⁴	5.5	n

TABLE V: Properties of Epitaxial GaAs Layers Grown in a SiO₂-BN-H₂ System
Growth Series #2100

Growth Conditions: Bakeout Temperature: 675°C; Bakeout Period: 15 hrs.
 Growth Temperature: 700°C; Cooling Rate: 4.5°C/min.
 H₂ Flow Rate: 0.6 l/min.

Growth No.	Dopant	Mobilities @ 300/77K (cm ² /V-sec)	Carrier Densities @ 300/77K (cm ⁻³)	Resistivity @ 300K (ohm-cm)	Conductivity Type
2101	-	6,000/68,000	2.0/1.9x10 ¹⁴	5	n
2102	-	5,800/73,000	1.2/1.2x10 ¹⁴	10	n
2103	-	8,400/98,000	1.0/1.1x10 ¹⁴	7	n
2104	-	7,300/94,000	1.1/1.2x10 ¹⁴	8	n
2105	-	6,100/80,000	7.4/8.2x10 ¹³	13	n
2106	-	420/6,800	2.4/1.9x10 ¹³	610	p
2107	-	7,500/100,000	3.6/4.2x10 ¹³	23	n
2108	-	6,700/79,000	7.8/7.9x10 ¹³	12	n
2109	Cr. (1.5 atm %)	8,300/69,000	4.3/4.1x10 ¹⁴	1.7	n
2110	"	7,500/78,000	1.8/1.6x10 ¹³	47	n
2111	"	300/-	9.2x10 ¹² /-	2300	p
2112	"	680/-	1.3x10 ¹³ /-	720	p
2113	"	390/-	2.7x10 ¹³ /-	600	p
2114 *	"	7,900/82,000	1.3x10 ¹³ /1.1x10 ¹³	59	n

* #2114 was grown at 675°C.

tivity of 610 ohm-cm. These results indicated that the bakeout transition temperature of the $\text{SiO}_2\text{-BN-H}_2$ system is about 675°C. Growth series #2100 was continued after adding 1.5 atomic % of Cr to the same melt. The carrier densities decreased, ranging from 9.2×10^{12} to $2.7 \times 10^{13} \text{ cm}^{-3}$. Layer #2111 had the highest resistivity of 2.3×10^3 ohm-cm and a sheet resistance of 1.3×10^6 ohm/ \square . The decrease in carrier density suggests that Cr introduces deep levels in the layers, but with carrier densities in the 10^{13} cm^{-3} range, it appears that the density of the deep level impurities is not large enough to compensate all of the residual impurities.

Complete data on carrier density vs. bakeout temperature for the $\text{SiO}_2\text{-C-H}_2$, $\text{SiO}_2\text{-BN(C)-H}_2$, and $\text{SiO}_2\text{-BN-H}_2$ systems (using undoped melts) were established as shown in Fig. 13. The bakeout transition temperatures are 775°C for the $\text{SiO}_2\text{-C-H}_2$ system, 700°C for the $\text{SiO}_2\text{-BN(C)-H}_2$ system, and 675°C for the $\text{SiO}_2\text{-BN-H}_2$ system. The carrier densities in layers grown from melts baked out at these temperatures are in the range of $1 \times 10^{14} \text{ cm}^{-3}$, $8 \times 10^{13} \text{ cm}^{-3}$, and $3 \times 10^{13} \text{ cm}^{-3}$, respectively.

B. Evaluation of Buffer Layers - Buffered vs. Unbuffered Structures

GaAs FETs fabricated using conventional epitaxial layers, grown directly on Cr-doped substrates, often show looping and bumping in the drain current-voltage characteristics. These have been attributed to the effects of the deep level impurities near the interface.²⁹ Transient capacitance techniques were used, therefore, to investigate the interface properties of active layers with and without semi-insulating LPE buffer layers. The buffer layers were grown at Stanford while the active layers were grown

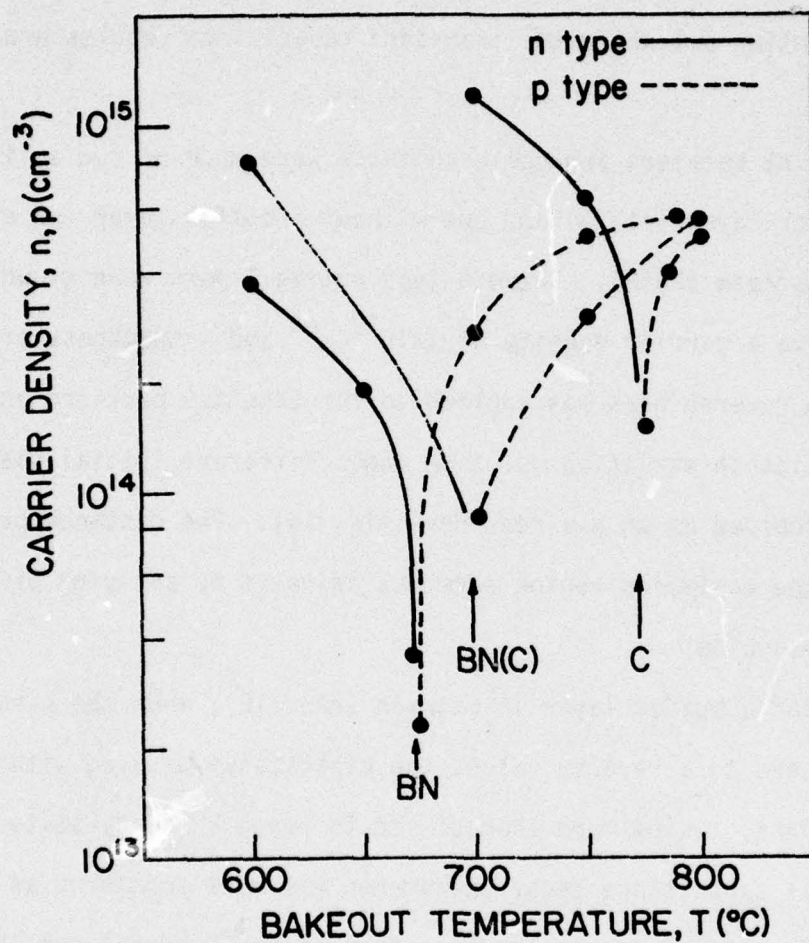


Fig. 13 Carrier density vs. bakeout temperature for three different growth systems:

C: Fused quartz-graphite-hydrogen ($\text{SiO}_2\text{-C-H}_2$) system.

BN(C): Fused quartz-boron nitride (on graphite cradle)-hydrogen ($\text{SiO}_2\text{-BN(C)-H}_2$) system.

BN: Fused quartz-boron nitride-hydrogen ($\text{SiO}_2\text{-BN-H}_2$) system.

separately at the Science Center. Each sample was split into two halves, one being used for the transient capacitance measurement, and the other being used to fabricate FET devices at the Science Center. The FET results are discussed in Section 6.1 while the transient capacitance results are reported here.

Schottky barriers and ohmic contacts were made on two active layers, one with a buffer layer (#1323) and one without a buffer layer (on a Crystal Specialties substrate #2312). These n-type active layers were grown in the same run and have a carrier density of $1 \times 10^{17} \text{ cm}^{-3}$ and a thickness of $0.35 \mu\text{m}$. A step function reverse bias was applied to the Schottky barriers and the depletion capacitance variation vs. time under different initial bias conditions were recorded by an x-y recorder (Fig. 14). The distance between the interface and the depletion region edge was adjusted by applying different values of reverse bias.

Without a buffer layer in between (#XS2312), when the bias was switched from zero to a reverse value, the capacitance decayed with a very long time constant, taking more than 50 sec to reach a steady-state value (Fig. 14). This capacitance decay phenomenon was more prominent as the depletion region came closer to the interface at the Cr-doped substrate. From the emission time constant vs. the reciprocal of the measurement temperature (Fig. 15), an activation energy of $0.57 \pm 0.02 \text{ eV}$ was obtained in the temperature range of 255 to 273K, with a trap density of 10^{16} cm^{-3} near the interface.

Transient capacitance measurements made on a second active layer (#3x45Hb) also grown directly on a semi-insulating substrate (Crystal Special-

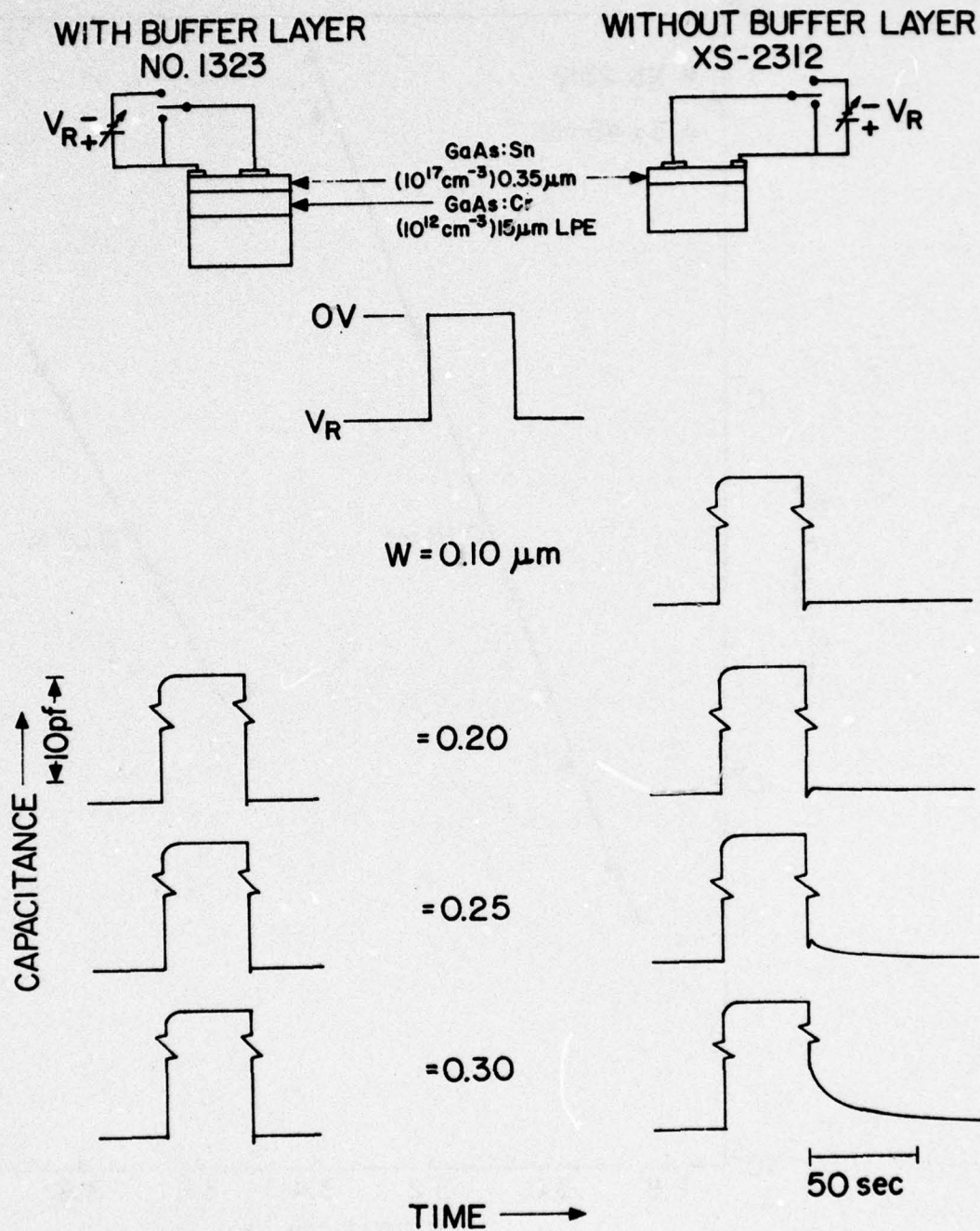


Fig. 14 Schematic diagram of the transient capacitance measurement setup and the capacitance variation with time corresponding to different bias states. W is the depletion region width of the Schottky barrier.

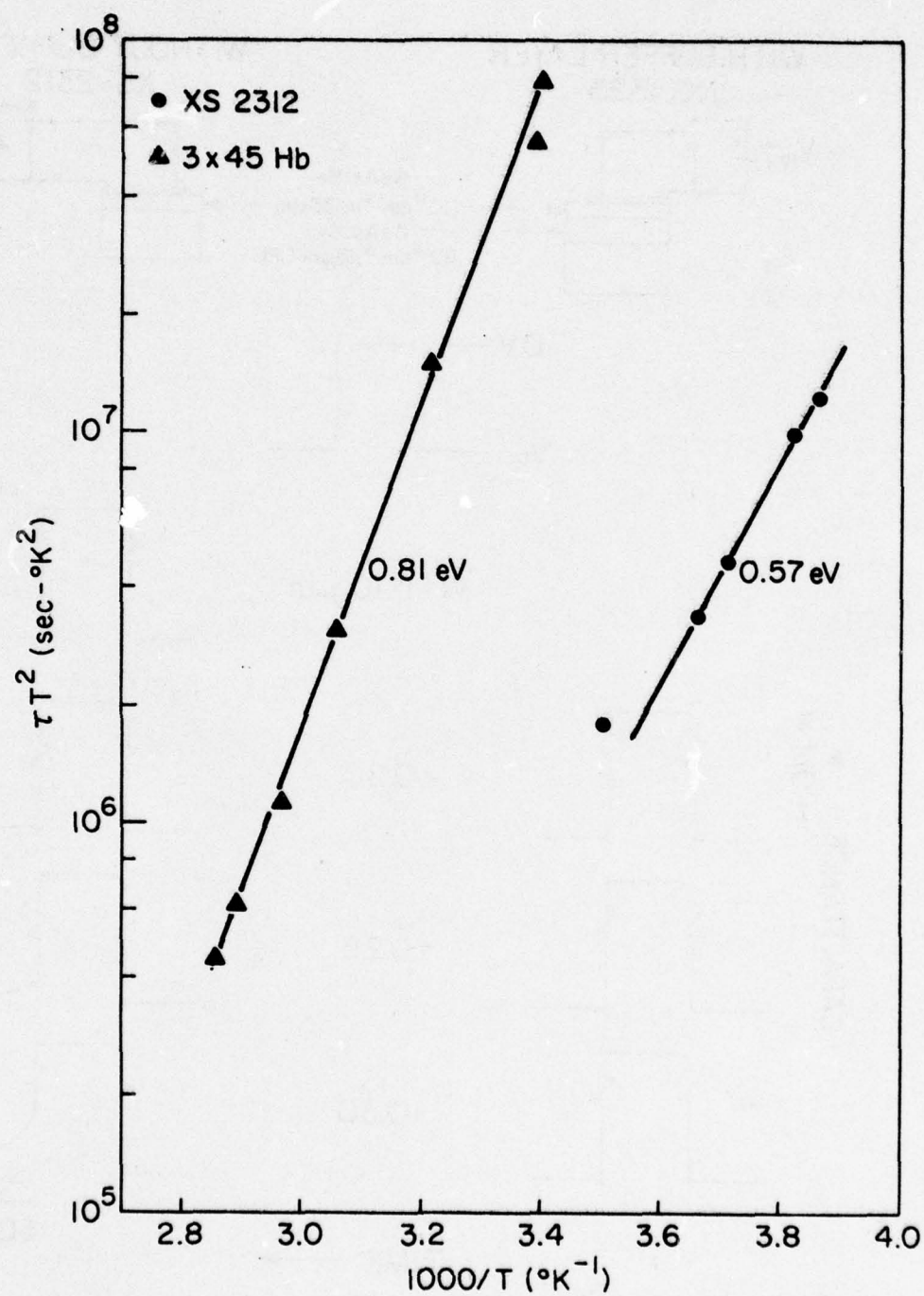


Fig. 15 Temperature dependence of the corrected time constant (τT^2) of the transient capacitance of an n-type GaAs FET active layer grown on a Cr-doped substrate.

ties #2000), showed the same trapping level. In the temperature range of 295 to 350K, an additional deep trap with an activation energy of 0.81 ± 0.01 eV and a trap density of $2 \times 10^{15} \text{ cm}^{-3}$ was obtained (Fig. 15).

In contrast with the unbuffered samples, the sample containing a buffer layer between the active layer and the substrate (#1323), showed no long time constant capacitance decay when tested under the same conditions. The capacitance reached its steady-state value simultaneously with the bias change (Fig. 14).

The sign of the capacitance change in the unbuffered samples indicates that both the 0.57 and 0.81 eV levels are hole traps. Since there is no minority carrier injection at a Schottky barrier under zero bias conditions, it should not be possible to detect hole traps in these measurements. However, since the trapping effects were observed only when the depletion edge of the Schottky barrier approached the substrate interface, they are probably due to an image effect of the trapping centers in the substrate side near the interface.³⁰

These results are a demonstration of the usefulness of a buffer layer between the active layer and the Cr-doped substrate to eliminate the effects of deep level impurities near the interface.

4.2 LPE Growth of Active and Buffer Layers for Microwave FETs - Cornell University

The boats used in the past for buffer layer growth (machined from Ultra-Carbon graphite) have required a long bakeout time (24 hrs. at 700°C) during each run to reach a steady value of ambient impurity density. If

shorter baking times are used, purity results are quite variable in buffer layers. In order to shorten the baking time and still get repeatable, good results, other boat materials are being tested. One such boat is a graphite boat that has been treated by a proprietary POCO carbon deposition³¹ that fills most of the pores in the graphite after the boat has been machined. Measurements in vacuum in our laboratory show that only one-sixth as much gas evolution occurs at 1400°C from this boat as compared with the usual graphite. Another such boat is pure (Spectrasil) quartz, which is dense and has much less capability of adsorbing oxygen or water vapor.

In a new, multiple-well boat made from Spectrasil quartz, pure p-type GaAs resulted, as expected, from silicon acceptors. The hole concentration was deduced to be approximately $2 - 4 \times 10^{13} \text{ cm}^{-3}$. This concentration was deduced by growing another layer in identical conditions with a controlled amount of tin, which resulted in n-type material with $160,000 \text{ cm}^2/\text{v-s}$ mobility at 77K and electron density of $\sim 1 \times 10^{14} \text{ cm}^{-3}$. Because the quartz is a relatively poor thermal conductor, some severe thickness variations ($\pm 25\text{-}40\%$) were obtained at slow cooling rates, ($.1^\circ\text{C}/\text{minute}$) but acceptable thickness variations ($\pm 5\%$) were obtained with $1^\circ\text{C}/\text{minute}$ cooling rates.

A POCO treated graphite boat³¹ was built. It was designed to hold large substrates, with $1.7 \times 1.7 \text{ cm}$ size, with an oversize melt of $2.1 \times 2.1 \text{ cm}$. The oversize melt allowed growth over the full substrate area with nearly negligible growth buildup at the edges, so that only $\pm 4\%$ thickness variations occurred over this larger area substrate. The melt height was constrained by using a tight cap with an array of holes to provide outgassing. The initial bakeout was done without a cap on the melt. After the first four runs, the

wetting and thus, the thickness uniformity fell below acceptable levels.

This particular problem is attributed to O_2 buildup in the melt (possibly an oxide scum) and was eliminated by baking the melt after every four runs without the cap on the melt.

Undoped epitaxial layers from a 4mm high melt have been grown in the POCO treated graphite boat and preliminary results in terms of electron mobility are very encouraging. These layers were grown at 700°C and all had a thickness of approximately 10μ . The substrate material was supplied by Crystal Specialties (boule #2440). Layer #CSD24102 was grown at 700°C after baking the melt nearly 14 hrs. at 700°C with a cooling rate of about $5.5^\circ\text{C}/\text{hour}$. This layer exhibited an electron mobility in excess of $9000\text{ cm}^2/\text{V-sec}$ with an associated net donor concentration of $1.7 \times 10^{14}\text{ cm}^{-3}$ at room temperature and a mobility between 120,000 and 150,000 $\text{cm}^2/\text{V-sec}$ with an associated net donor concentration of $1.7 \times 10^{14}\text{ cm}^{-3}$ at 77K. No significant change of the liquid nitrogen electron mobility or electron concentration was observed when the baking period was extended to 21 hours.

5.0 ION IMPLANTATION AND ION BEAM ANALYSIS

This section of the report covers four distinct areas: (1) Qualification tests for semi-insulating GaAs in order to determine its suitability as a substrate for doping by ion implantation, (2) Capless annealing of high dose Se implants, (3) Investigations of the Ge-Au-Ni system used for contacts to GaAs, and (4) Reordering of implanted amorphous layers in GaAs.

The first part shows that it is possible to identify semi-insulating GaAs which is not suitable for low level implantation doping by a simple annealing test of capped samples. The second portion of the work demonstrates that when high dose Se implanted samples are annealed by a capless technique approximately the same doping levels can be produced as were reported using an aluminum oxy-nitride cap. The third investigation on the behavior of Ge-Au-Ni triple layers is of interest in connection with a widely used metalization scheme for GaAs. The outstanding result is that short-term annealing of 450°C induces vast modifications, the nature of which are presently being investigated further. The fourth study investigates the reordering of amorphous layers produced by implantation of 100 keV Zn or 400 keV Se ions at a dose of 3×10^{13} ions/cm² into GaAs substrates at LN₂ temperatures and followed by annealing between 200 and 600°C. We conclude that reordering of amorphous layers is not a simple epitaxial regrowth process as found for implanted Si and Ge.

5.1 Substrate Qualification - Science Center

The evaluation of semi-insulating GaAs substrates for epitaxial growth by annealing in an epitaxial reactor at temperatures of the order of

750 to 800°C has been described elsewhere in this report (Section 3.2.2) and in an earlier report.¹ An equivalent type of test to evaluate the suitability of substrates for implantation would be to anneal a capped sample at the temperature used for annealing implanted samples. Any significant decrease in the resistivity of the substrate as a result of this treatment would indicate that the material was not suitable for implantation doping and subsequent fabrication of devices. A possibly more severe test would be to simulate the disorder introduced during the implantation of the dopant by bombarding the substrate with inert gas ions having approximately the same mass as the dopant. We have employed both types of tests in evaluating material from 8 different boules of semi-insulating GaAs grown by Crystal Specialties. Kr bombardment was used to simulate the disorder introduced during Se implantation.

The results of these tests are summarized in Table VI. Material from 3 different boules showed large changes under both types of qualification test. The material from the other five boules retained a high resistivity after either type of qualification test. The material which did change showed n-type conducting layers following the anneal. Boule #2132, which exhibited the largest change, was material specially prepared to have a very high Cr content ($\sim 5 \times 10^{17} \text{ cm}^{-3}$). The conductivity of the n-type layers formed during these annealing tests seems to be somewhat higher in the case of the Kr bombarded samples than for those which received no bombardment prior to capping and annealing.

Samples from these different boules of semi-insulating GaAs were

TABLE VI: Si_3N_4 -Capped, Cr-doped GaAs Samples Annealed at 850°C for 30 Minutes.

Boule No	No Implant		1.8×10^{12} -400 keV Kr ions/ cm^2	
	$\rho_s(\Omega/\square)$	$N_s(\text{cm}^{-2})$	$\rho_s(\Omega/\square)$	$N_s(\text{cm}^{-2})$
2132	~ 1500		482	4.2×10^{12}
2299	2250	5×10^{11}	~ 1500	
2312			1220	1×10^{12}
Typical Good Material			$\sim 6 \times 10^8$	

implanted with 400 keV Se ions to a dose of $1.8 \times 10^{12}/\text{cm}^2$ and annealed at the same time as the samples undergoing the qualification test. Electron concentration profile results obtained using an automatic C-V profiler are shown in Fig. 16. The doping level for the sample from boule #2132 is much higher than any of the other profiles. Since the semi-insulating material normally used for implantation does not contain the very high level of Cr in this material, this result will not be discussed further. The other profiles in Fig. 16 include a typical profile from an implant into good semi-insulating material and a profile obtained from an implant into a low electron concentration epitaxial layer. These two are seen to be quite close to each other. The fourth profile in the figure (labeled "bad semi-insulating material") was obtained from a sample of the material from boule #2312 which was implanted with Se. The maximum electron concentration observed for this sample is similar to the other two, however, there is a deep tail on the profile which was typical of results obtained when implanting into samples from boule #2312 and #2299.

Se doping profiles were measured for two samples from each of the five boules of good semi-insulating material. Average profile parameters, as well as the standard deviation in these parameters, are shown in Table VII. N_{max} is the maximum electron concentration observed, $X_{70\%}$ is the depth at which the electron concentration was 70% of N_{max} and $X_{10\%}$ is the depth at which the electron concentration was 10% of N_{max} . These results indicate that by employing a fairly simple qualification test it is possible to select semi-insulating GaAs substrates which will permit one to obtain good reproducibility in doping profiles for low dose implantations which yield layers suitable for the fabrication of Schottky barrier FETs.

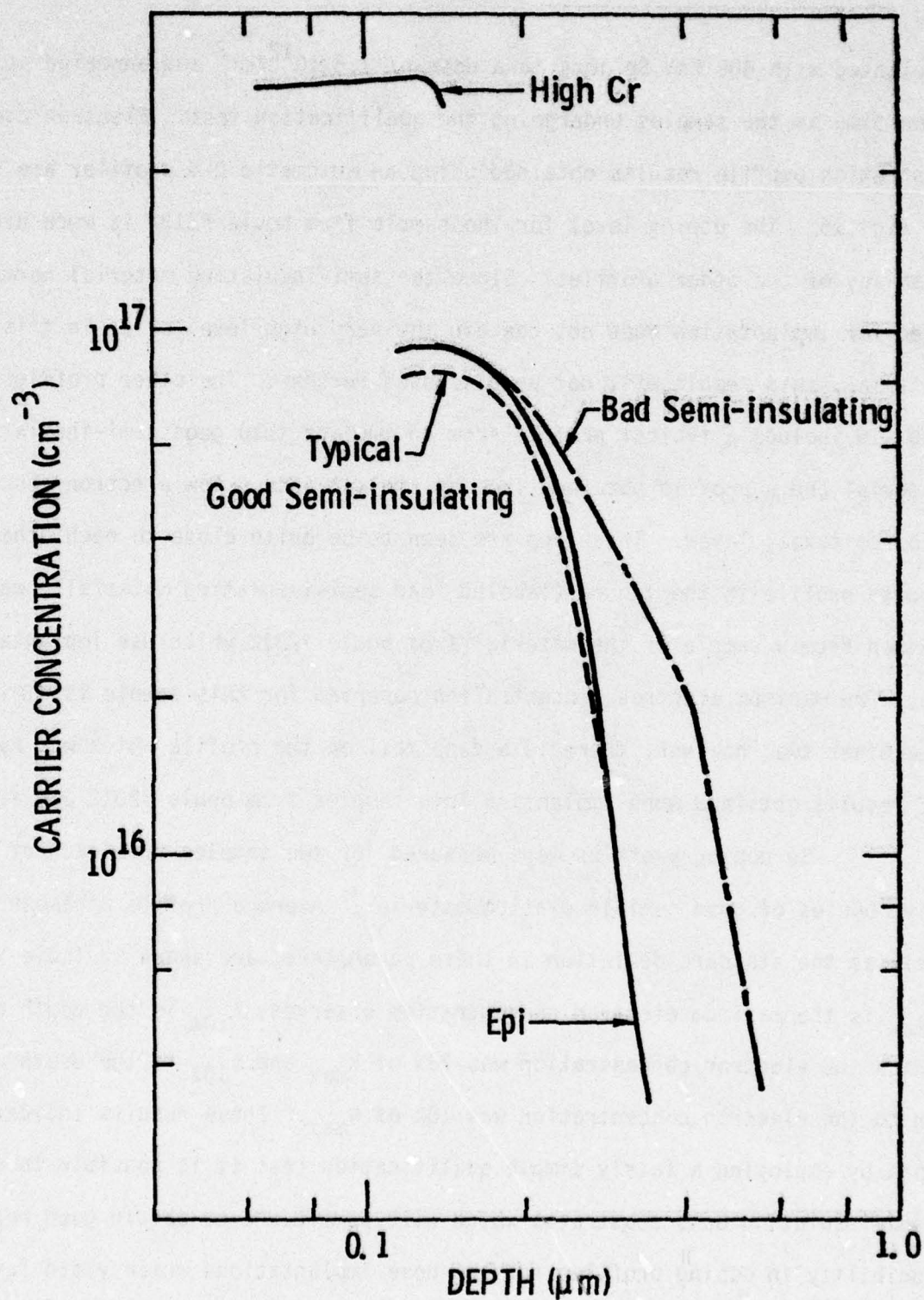


Fig. 16 Electron concentration profiles for various GaAs substrates implanted at 350°C with 1.8×10^{12} 400 keV Si ions/cm² and annealed at 850°C for 30 min with a silicon nitride cap.

TABLE VII: Average Profile Parameters for Se Implants
(400 keV - 1.8×10^{12} ions/cm²) into Cr-doped
Semi-Insulating GaAs from 5 Different Boules.

N_{max}	$8.2 \pm .8 \times 10^{16} \text{ cm}^{-3}$
X at 70% of N_{max}	$2100 \pm 100 \text{ \AA}$
X at 10% of N_{max}	$3125 \pm 245 \text{ \AA}$

It should be pointed out again that the results of this qualification test for material from a given boule are different than the results of the qualification test employed for epitaxial growth (see Section 3.2.2). In particular, substrates #2299 and #2312 seemed to be suitable for epitaxial growth whereas they were not suitable for implantation. The reasons for these differences and the mechanism for the production of the n-type layer observed in the implantation qualification tests are not clear at present. For the material tested, one correlation has been observed. Excluding the very high Cr boule (#2312), all good material was from boules which had been grown directly from the components. The bad material was from boules which had been regrown or prereacted.

5.2 Capless Annealing of High Dose Se Implants - Science Center and California Institute of Technology

A capless technique for the annealing of ion implanted GaAs has recently been developed as a part of our IR&D supported implantation program. Details of the application of this technique to the annealing of low dose Se implanted samples are contained in a recent publication.³² The capless technique was also applied to the annealing of samples implanted with high doses of Se ions. The results were found to be similar to those previously reported for high dose Se implants annealed with an aluminum oxy-nitride cap. Results for doses of 1×10^{14} and 2×10^{14} Se ions/cm² are shown in Figs. 17 and 18, respectively. Data from samples annealed with an aluminum oxy-nitride cap are included for comparison. For both doses, there is a significant increase in the doping level achieved, using the capless technique, when the annealing

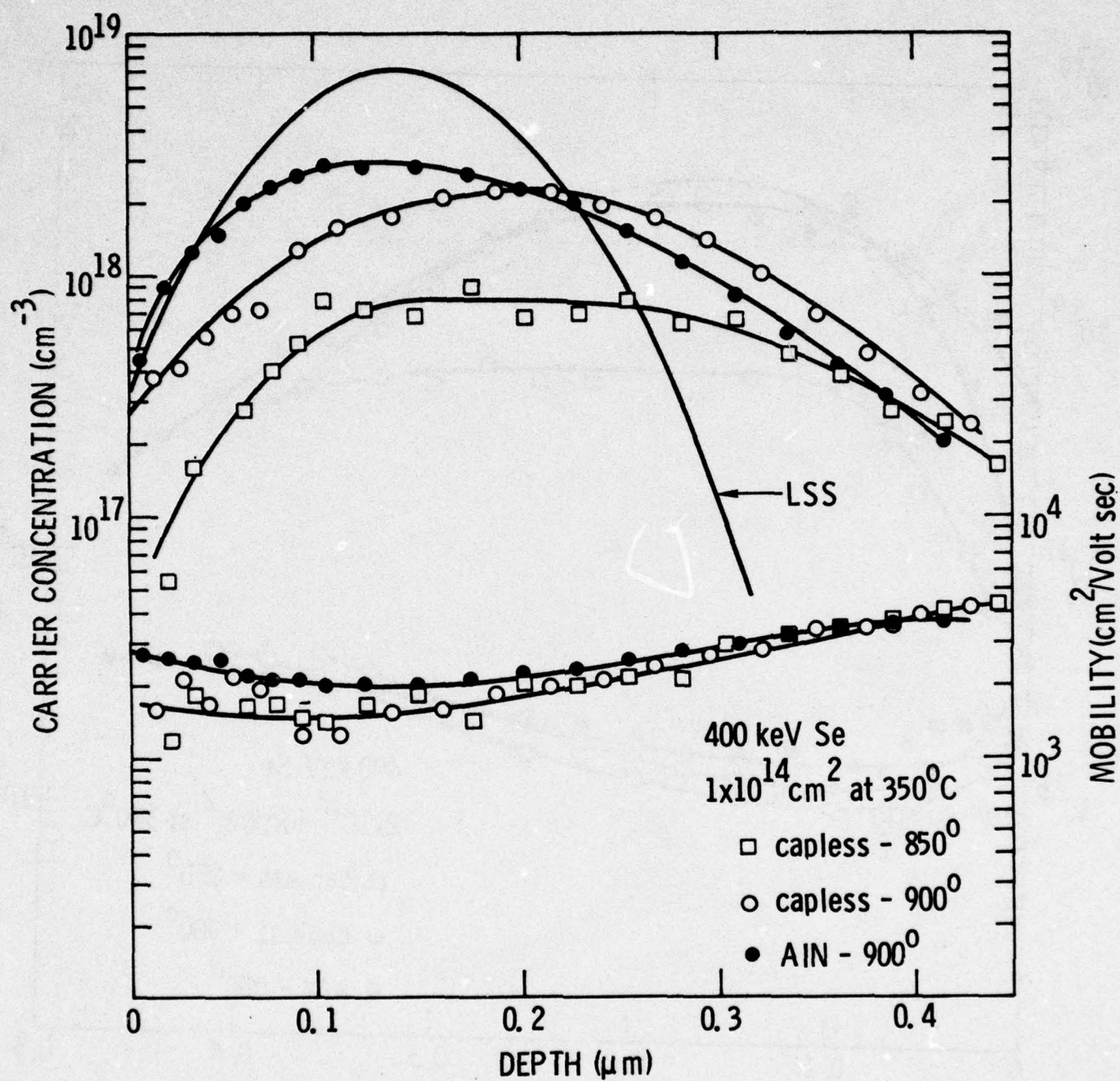


Fig. 17 Electron concentration and mobility profiles for semi-insulating GaAs samples implanted with 1×10^{14} 400 keV Se ions/cm² at 350°C and annealed under the conditions indicated.

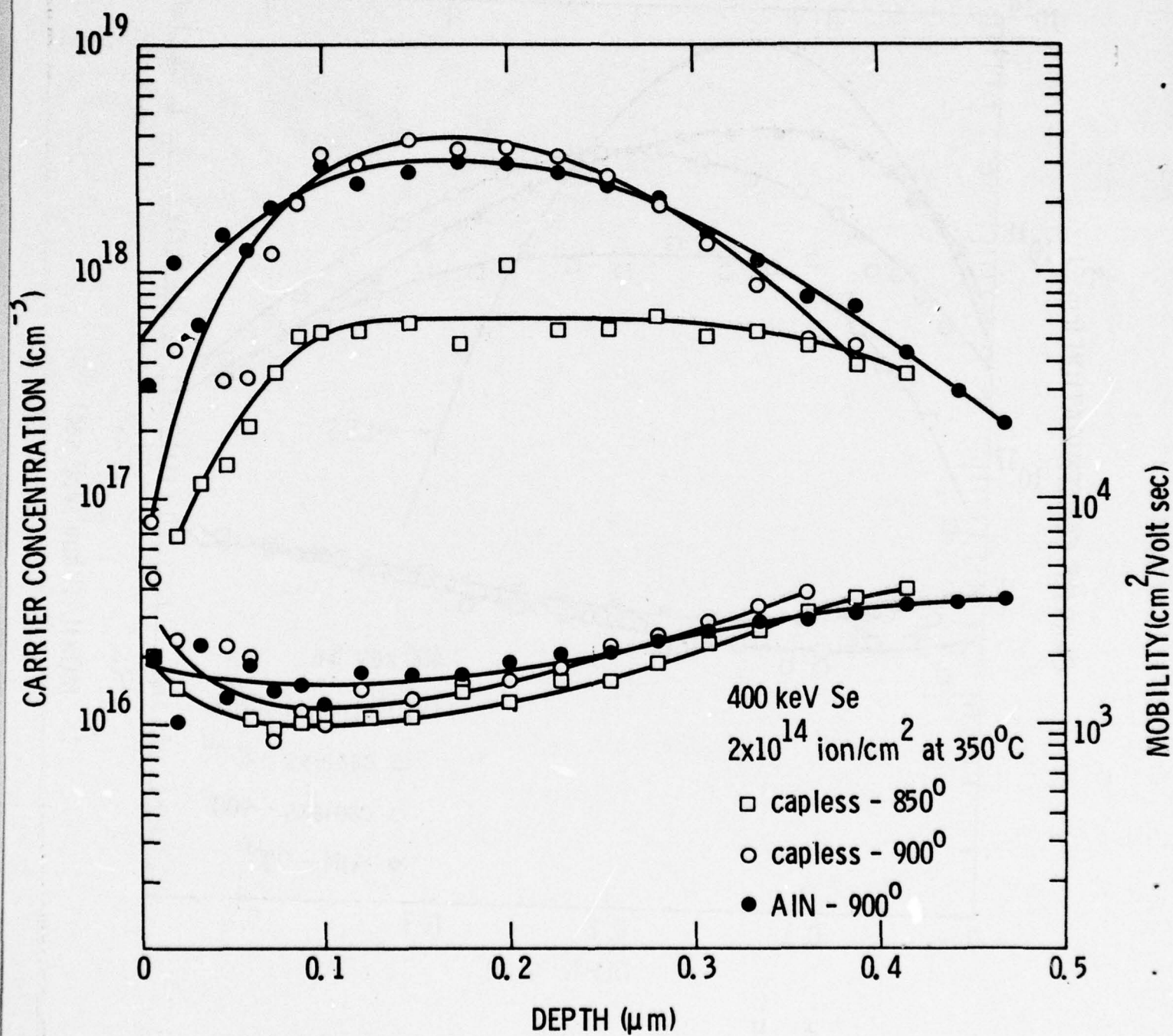


Fig. 18 Electron concentration and mobility profiles for semi-insulating GaAs samples implanted with 2×10^{14} 400 keV Se ions/cm² at 350°C and annealed under the conditions indicated.

temperature was raised from 850° to 900°C. The data for a dose of 1×10^{14} Se ions/cm² indicate that the doping level for the capless annealed sample was not quite as high as that observed for the sample annealed with an aluminum oxy-nitride cap. However, the doping profiles observed for 900° anneals of the samples implanted with 2×10^{14} Se ions/cm² are quite similar. The ability to obtain high doping levels by ion implantation of GaAs using either a capped or a capless annealing technique gives considerable flexibility in the development of processes to utilize high dose implantations in the fabrication of microwave devices in GaAs.

5.3 Investigations of the Ge-Au-Ni System Used for Contacts to GaAs - California Institute of Technology

A Ge-Au-Ni metalization scheme is widely used for ohmic contacts to GaAs. However, the metallurgy of this system is not understood. After heat treatment of the contacts above the Ge-Au eutectic temperature, island formation of unknown composition has been reported and the high current injection capability of the contacts has been attributed to this island formation. Therefore, it is important to get more information about the ternary system Ge-Au-Ni.

In order to prevent reactions with GaAs, which would complicate the situation, an inert substrate (SiO₂) was used. Different sequences of Ge, Au and Ni layers were evaporated on the substrate with an electron gun in a vacuum of 10^{-7} torr. The samples were then annealed at 450°C for 5, 10, 20 and 40 min in a vacuum of 8×10^{-7} torr. The analysis of the samples was carried out using 2 MeV He⁺ backscattering spectrometry, SEM observation and SEM

electron-beam-induced X-ray analysis.

Early investigations showed that Ni and Ge form Ni_2Ge in a temperature range of 150°C to 300°C. This is illustrated in Fig. 19. From the heights of the Ni and Ge signals in the backscattering spectrum, a concentration ratio of Ni to Ge of 2.1 was found, and X-ray diffraction analysis identified the compound as Ni_2Ge . Between 250°C and 600°C, NiGe is formed as shown in Fig. 20.

After annealing a sample having the structure $\text{SiO}_2/\text{Ge}/\text{Au}/\text{Ni}$ at 450°C for 5 min, backscattering analysis shows the spectrum given in Fig. 21. This spectrum indicates that annealing has major effects: (a) the Ge peak disappears in the annealed sample, (b) the Au peak is shifted to lower energies, indicating that additional mass has accumulated on top of the Au layer, and finally, (c) a little Au has penetrated into the layer above it. This implies that Ge moved through the Au and formed a Ni-Ge compound with the Ni. That the Au plays only a passive role in the Ni-Ge reaction is shown in a backscattering spectrum of a sample having the structure $\text{SiO}_2/\text{Ge}/\text{Ni}/\text{Au}$ (Fig. 22). The Ni and the Ge react together but the Au signal is not changed at all by the heat treatment. Similar results were obtained by other combinations of the Ge, Au and Ni layers.

Since there is more Ge than needed to form a compound with Ni, two questions arise immediately: Where is the excess Ge? What Ni-Ge compound is formed? The first question is answered by etching off the nickel-germanide layer from the sample of Fig. 21 and investigating the remaining Au layer. From SEM observation it was determined that the Au layer was laterally nonuniform. However, an X-ray analysis did not detect any amount of Ge in the

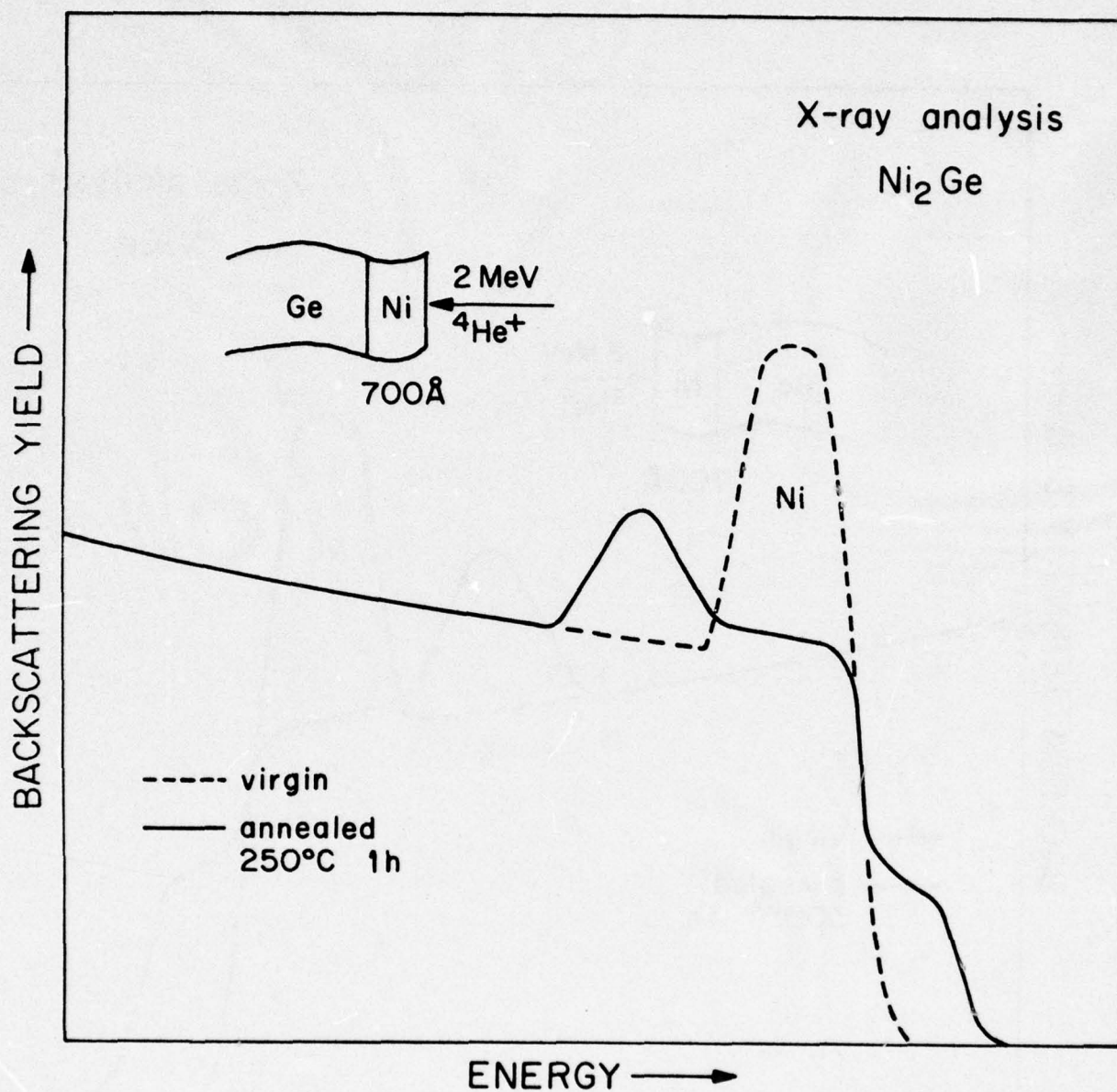


Fig. 19 Backscattering spectra for 2 MeV He ions incident on a Ni-Ge sample before and after annealing at 250°C for 1 hour.

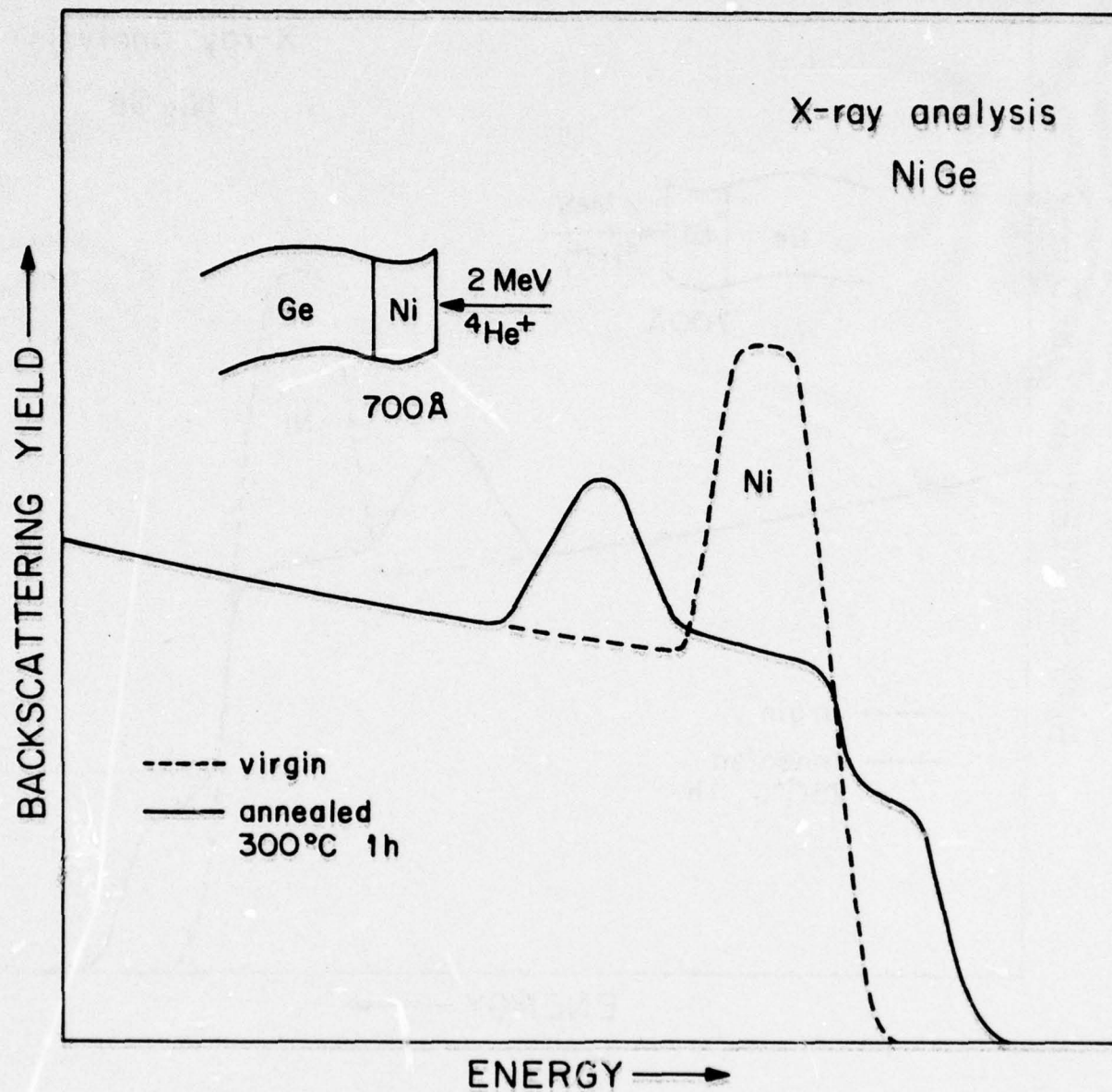


Fig. 20 Backscattering spectra for 2 MeV He ions incident on a Ni-Ge sample before and after annealing at 300°C for 1 hour.

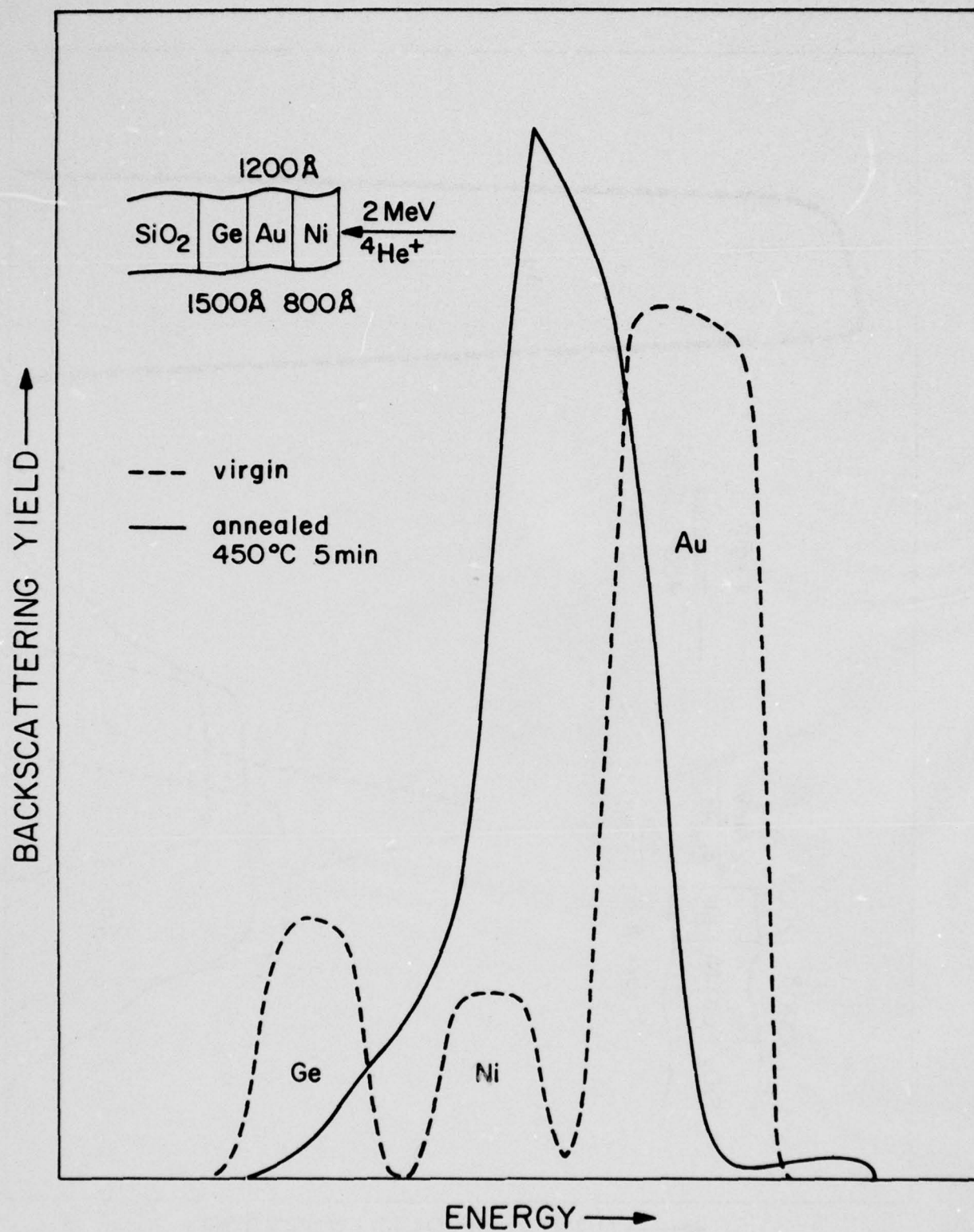


Fig. 21 Backscattering spectra for 2 MeV He ions incident on a Ni-Au-Ge sample before and after annealing at 450°C for 5 min.

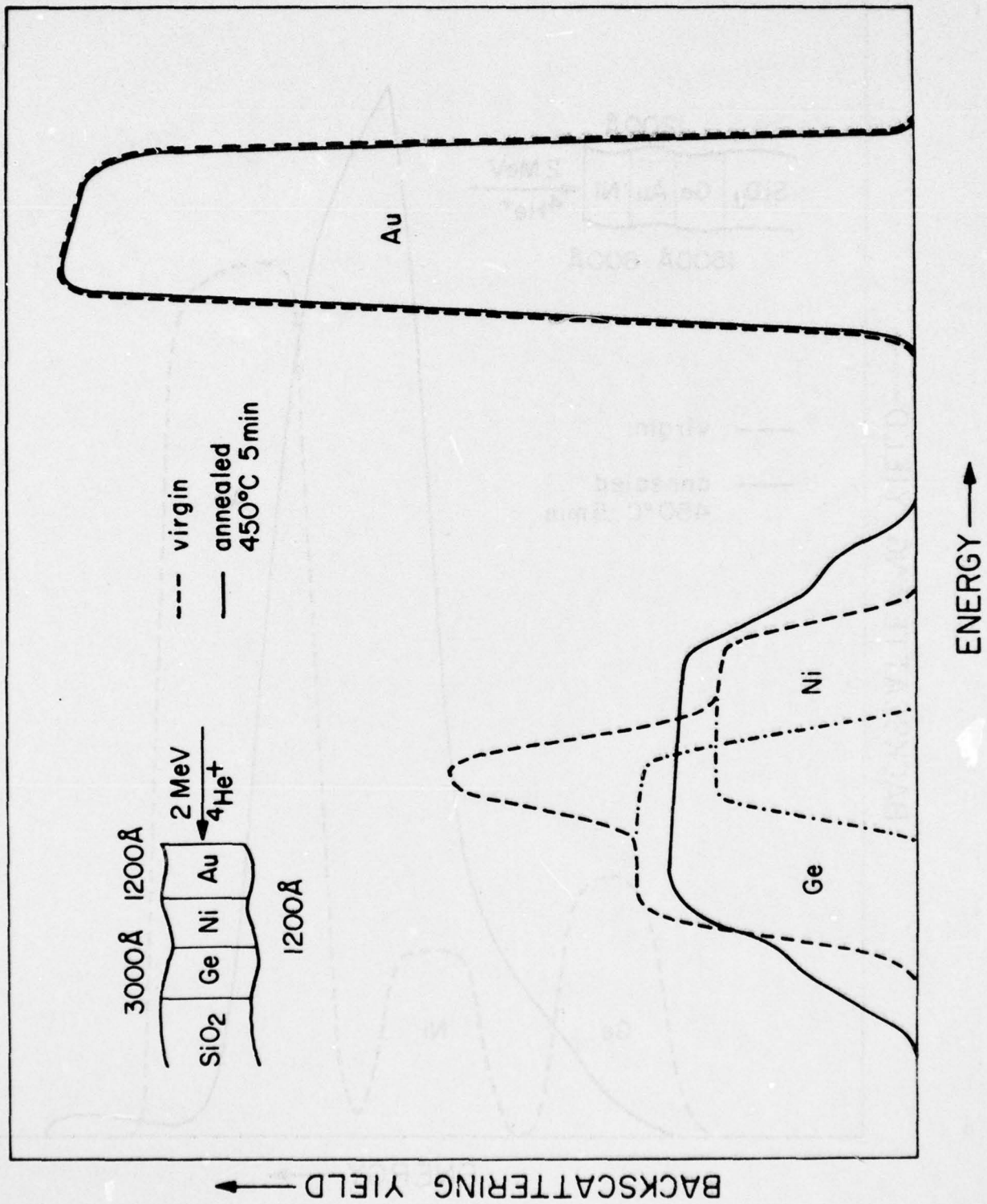


Fig. 22 Backscattering spectra for 2 MeV He ions incident on a Au-Ni-Ge sample before and after annealing at 450°C for 5 min.

Au within its resolution limit ($\sim 1\%$). Thus, the excess Ge forms a mixture with the Ni-Ge compound on top of the Au layer. The second question is answered by the Ni-Ge study which indicates that at 450°C the Ni-Ge compound is of the chemical form NiGe. Both answers have to be confirmed by X-ray analysis.

In conclusion, the backscattering technique is proving very useful for studying the behavior of the ternary Ge-Au-Ni upon heat treatment. Our preliminary results indicate that during annealing Ge diffuses through the Au and forms a compound with the Ni. The Au acts mainly as transport medium for the Ge but it otherwise plays a passive role. Investigations on this subject continue.

5.4 Reordering of Implanted Amorphous Layers in GaAs - Science Center and California Institute of Technology

Amorphous layers produced by ion implantation in Si or Ge reorder epitaxially on the underlying single crystal substrate.³³ Recent measurements^{34,35} have shown that the kinetics of the epitaxial reordering are rather simple: the growth rate is linear in time and there is a well-defined activation energy. For isochronal anneal sequences, the reordering occurs over a relatively narrow temperature interval of 50 to 70°C . In contrast, studies of the annealing of high dose implanted GaAs³⁶⁻³⁸ have shown that the reordering occurs over a broad temperature interval.

Another difference between GaAs and Si is in the electrical behavior of the implanted regions. In Si, high electrical activity is found after annealing in the temperature range where the amorphous layer reorders.³³ Significantly higher anneal temperatures are required to achieve high electrical

activity in hot substrate implantation in Si where the disorder anneals during the implantation process as compared to R.T. implantation where an amorphous layer is formed. Almost the reverse is true for high dose implantation in GaAs. Hot substrate implantation is required to achieve high electrical activity.³⁹ In low temperature implantation where an amorphous layer is formed, much lower electrical activity is found at the same anneal temperatures as those used for hot substrate implantations.

These results suggest that there is a major difference between the anneal behavior of amorphous layers of Si and Ge and that of GaAs. Shimada et al.⁴⁰ also noted that implanted amorphous layers of GaP exhibited high amounts of residual disorder after annealing. The purpose of the present work was to investigate the reordering of implanted amorphous layers on GaAs following the precautions observed in studies of Si and Ge. Amorphous layers were formed by implantation at LN₂ temperatures so that impurity concentrations did not exceed solubility values. Both n- and p-type dopants were used to determine if the impurity type had an influence on the annealing behavior. In $\langle 111 \rangle$ oriented Si the anneal behavior is strikingly different than in $\langle 100 \rangle$ Si and the amount of disorder depends on the anneal procedures.⁴¹ Therefore, $\langle 111 \rangle$, $\langle 100 \rangle$ and $\langle 110 \rangle$ substrates were used to investigate possible orientation effects. Both isothermal and isochronal anneal sequences were also used to determine if the amount of disorder was dependent on the anneal procedure.

The samples were Cr-doped semi-insulating GaAs having $\langle 100 \rangle$, $\langle 110 \rangle$ or $\langle 111 \rangle$ orientation. In these samples the surface normal was $< 1^\circ$ off the specified crystal axis. The amorphous layer was formed by im-

planting Zn or Se into samples held at 80K and oriented such that the beam was incident at about 10° to the crystal axis, in order to minimize channeling. The Zn implantations were made at 100 keV to a dose of 3.3×10^{13} ions/cm²; the Se at 400 keV to a dose of 3×10^{13} ions/cm². In some cases, implantations at two energies were used to produce a nearly uniform impurity concentration. The maximum impurity concentrations in the region near the projected range correspond to 7×10^{18} atoms/cm³ for Zn and 2.8×10^{18} atoms/cm³ for Se. The annealing was performed in a flowing hydrogen atmosphere in a quartz tube furnace. Annealing at temperatures higher than 500°C was done using sputtered silicon nitride films, deposited on the sample surface, to avoid surface decomposition.

Channeling effect measurements with 1 MeV ^4He ions were used to investigate the recovery of the amorphous layer. Measurements were also made with 400 keV H^+ ions. Energy to depth conversions for ^4He analysis were made using the stopping cross-sections of Ziegler and Chu.⁴² Transmission electron microscopy and glancing angle X-ray diffraction were employed to obtain information on the structure of the regrown layer.

Fig. 23 shows random and $\langle 100 \rangle$ GaAs samples implanted with Zn and annealed at various temperatures for 15 min. The spectrum for an as-implanted sample indicates that the implanted layer becomes amorphous over a depth of about 720Å. The spectrum for a sample annealed at 200°C shows that some recovery of crystallinity occurs at the interface between the amorphous layer and the underlying crystal. This is indicated by a shift in the rear edge of the aligned spectra toward the surface. After 300°C annealing, the backscattering yield decreases but is still high compared to

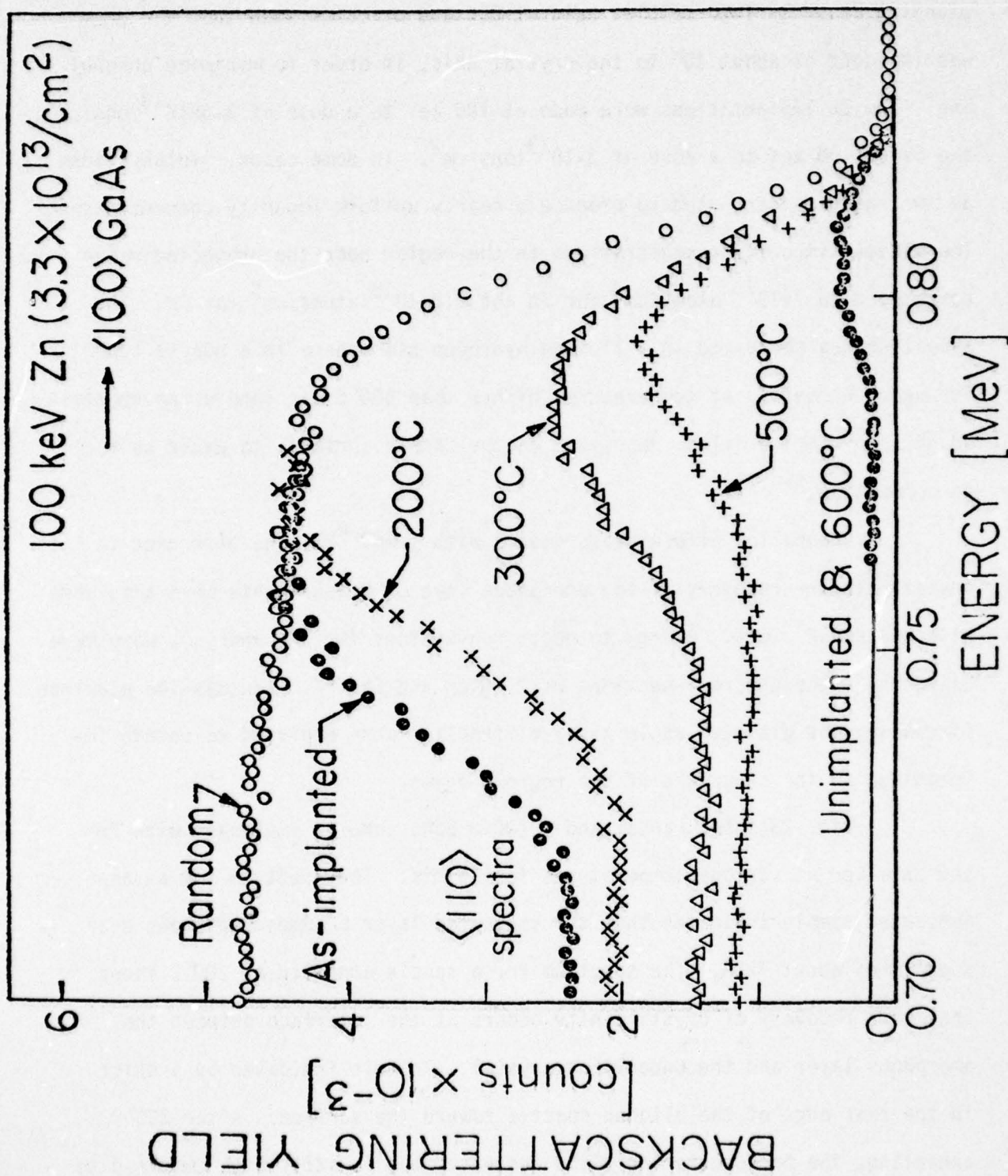


Fig. 23 Random and $\langle 110 \rangle$ aligned backscattering spectra from $\langle 100 \rangle$ GaAs samples implanted with Zn and annealed for 15 min at the indicated temperatures.

the unimplanted samples, showing that the implanted layer contains a high level of disorder. Complete recovery was observed after 600°C annealing. The annealing of the amorphous layer produced in $\langle 100 \rangle$ and $\langle 110 \rangle$ GaAs by 400 keV Se implants shows almost the same behavior as shown in Fig. 23. Some recovery was observed at the interface between the amorphous layer and the underlying crystal for annealing at 200°C, the amorphous layer disappeared after annealing at 300°C and significant recovery occurred after annealing at 600°C. These results suggest that the temperature range between 200 and 300°C is an interesting region in which to investigate the reordering of amorphous layers.

The isothermal annealing behavior of Zn implanted $\langle 100 \rangle$ and $\langle 111 \rangle$ GaAs at 200°C and 300°C is shown in Fig. 24. The aligned backscattering spectra were measured for the $\langle 110 \rangle$ axis. At 200°C both $\langle 100 \rangle$ (Fig. 24a) and $\langle 111 \rangle$ (Fig. 24c) GaAs shows recovery at the interface between the amorphous layer and the underlying crystal. The recovery during the initial 15 minutes is fast compared to that which occurs during subsequent annealing. This is possibly due to recovery in the transition region (not amorphous) between the amorphous and the crystalline layer. The recovery rate seems to be lower for $\langle 111 \rangle$ GaAs than for $\langle 100 \rangle$ GaAs but the difference is not large compared to the difference found between $\langle 111 \rangle$ and $\langle 100 \rangle$ orientations in Si³⁴ and Ge.⁴³ After annealing for 350 min., the amorphous layer almost disappeared but a high density of disorder still remained in the implanted layer. After the samples were annealed for 700 minutes, the residual disorder seems somewhat higher for $\langle 111 \rangle$ GaAs than for $\langle 100 \rangle$ GaAs.

At 300°C (Figs. 24b and 24d) the amorphous layer disappeared after

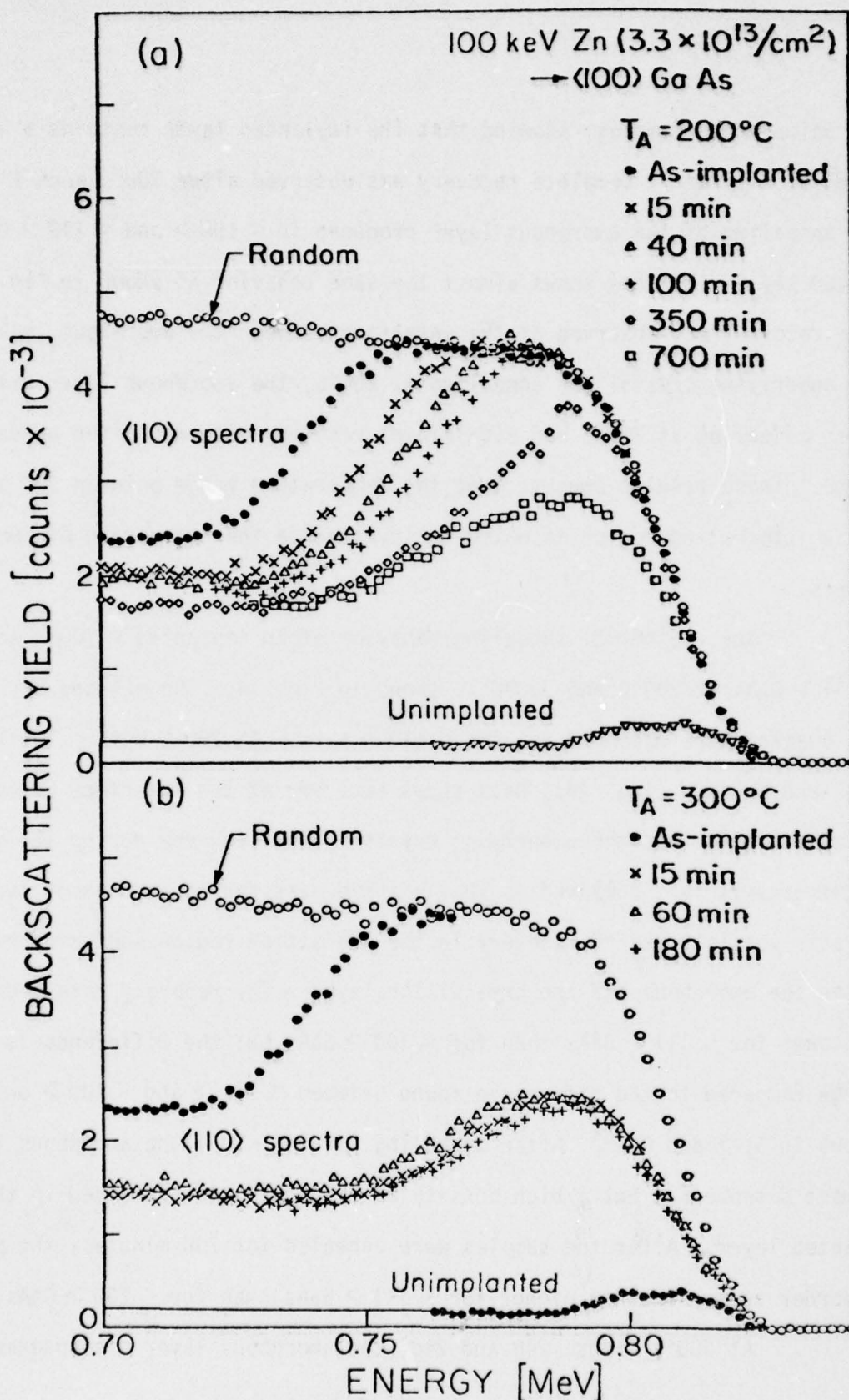


Fig. 24 Random and $\langle 110 \rangle$ aligned backscattering spectra from $\langle 100 \rangle$ (a and b) GaAs samples implanted with Zn and annealed as indicated.

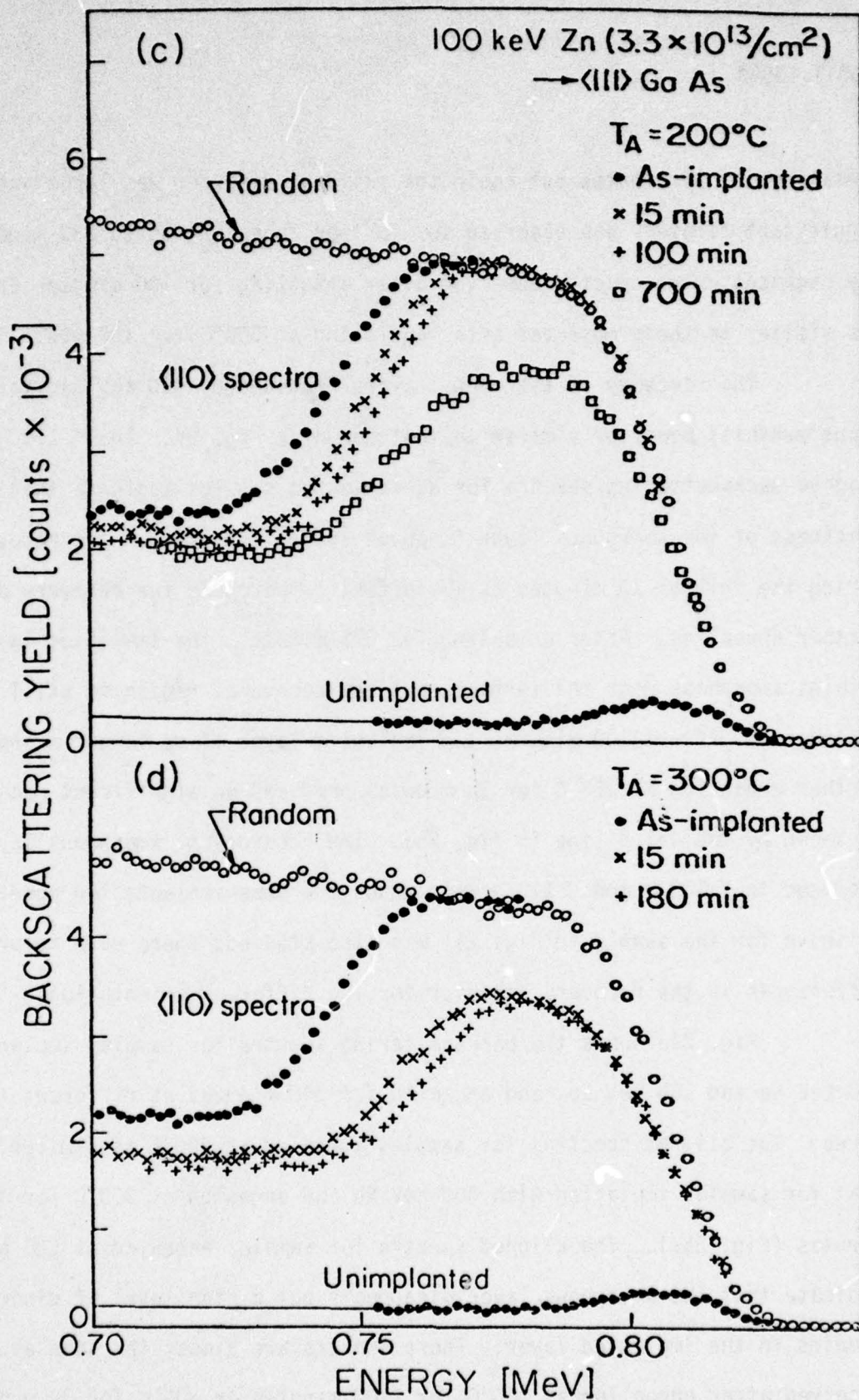


Fig. 24 Random and $\langle 110 \rangle$ aligned backscattering spectra from $\langle 111 \rangle$ (c and d) GaAs samples implanted with Zn and annealed as indicated.

annealing for 15 minutes but again the residual disorder was large and no significant recovery was observed for further annealing up to 180 minutes. The backscattering spectra observed after annealing for 700 minutes at 200°C are similar to those observed after annealing at 300°C for 180 min.

The recovery of amorphous layers produced by 400 keV Se implantations exhibits behavior similar to that shown in Fig. 24. The $\langle 111 \rangle$ aligned backscattering spectra for as-implanted samples indicate that the thickness of the amorphous layer is about 1600Å (Fig. 25a). The recovery during the initial 15 minutes is again fast compared to the recovery during further annealing. After annealing for 375 minutes, the implanted layer only remains amorphous near the surface, but the recovered region is still heavily disordered. After 1100 minutes the implanted layer is no longer amorphous. Further annealing at 300°C for 30 minutes produces no significant recovery as shown by the solid line in Fig. 25a. The recovery of amorphous layers produced in $\langle 100 \rangle$ and $\langle 110 \rangle$ GaAs under the same implantation conditions as shown for the sample in Fig. 25a was also studied; there were no pronounced differences in the recovery behavior for the different orientations.

Fig. 25b shows the backscattering spectra for samples implanted with 400 keV Se and 100 keV Se₂ and annealed for 343 minutes at different temperatures. The aligned spectrum for samples annealed at 200°C is similar to that for samples implanted with 400 keV Se and annealed at 300°C for 375 minutes (Fig. 25a). The aligned spectra for samples annealed at 220 and 250°C indicate that the amorphous layer disappears but a high level of disorder still remains in the implanted layer. These spectra are almost the same as those observed after annealing at 200°C for 1100 minutes or 300°C for 30 minutes

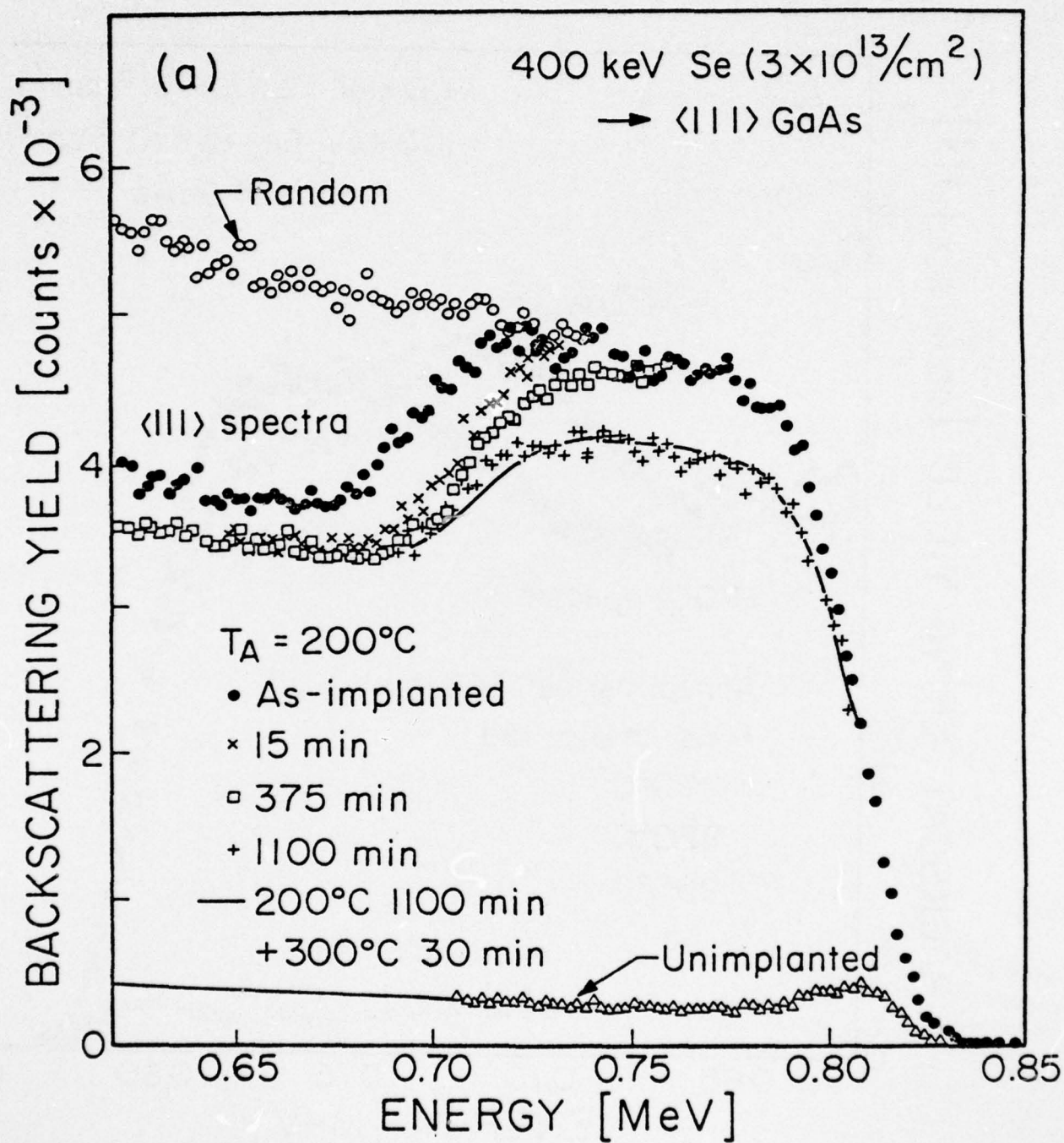


Fig. 25(a) Random and aligned spectra from Se implanted GaAs samples annealed as indicated. $\langle 111 \rangle$ GaAs and $\langle 111 \rangle$ aligned spectra.

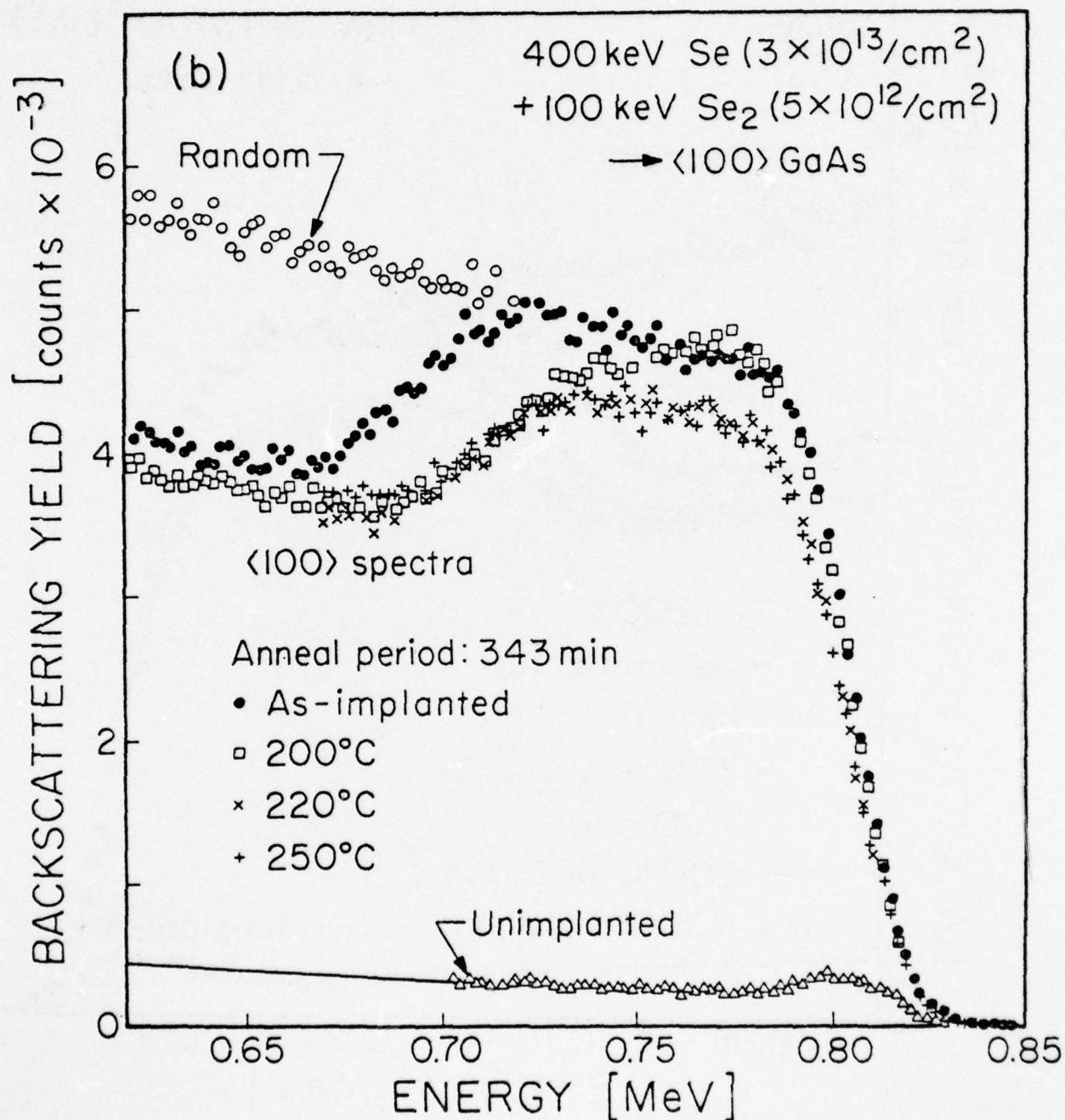


Fig. 25(b) Random and aligned spectra from Se implanted GaAs samples annealed as indicated. (b) $\langle 100 \rangle$ GaAs and $\langle 100 \rangle$ aligned spectra.

as shown in Fig. 25a.

Transmission electron microscopy and glancing angle X-ray diffraction measurements have been employed in an effort to characterize the disorder present in annealed implanted layers. The samples were implanted with 400 keV Se ions and exhibited backscattering spectra similar to that represented by the solid curve in Fig. 25a. The glancing angle X-ray diffraction measurements showed blurred spots in the diffraction pattern. This indicated the presence of substructure in the annealed layer. The absence of rings and extra spots in the diffraction pattern shows that the regrown layer is not polycrystalline and it is epitaxial with the underlying substrate.

The epitaxial nature of the regrown layer and the presence of substructure was shown directly in TEM micrographs and selected area electron diffraction patterns. An example of the substructure is shown in Fig. 26. Extensive streaking in $\langle 111 \rangle$ directions in the electron diffraction pattern in Fig. 24b arises from the high density of thin regions (substructure) lying along $\{111\}$ planes, one variant of which is illustrated in Fig. 24a. We speculate that this substructure may be antiphase domains, resulting from homogeneous nucleation of crystalline GaAs in the amorphous layer. Evidence for epitaxy was the observation that the crystallographic direction of the normal to the surface of the regrown layer was $[100]$ which is parallel to the $[100]$ surface normal of the substrate.

In conclusion, a significant difference was found between the annealing behavior of implanted amorphous layers in GaAs and that found for Ge or Si. In the case of GaAs, the recovery of the amorphous layer shows no

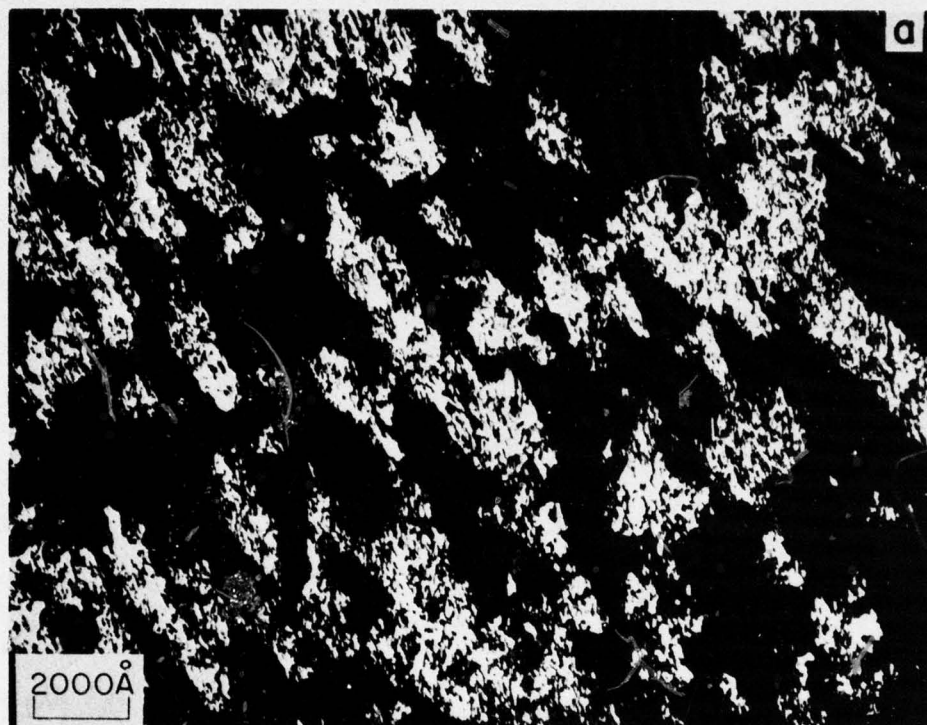
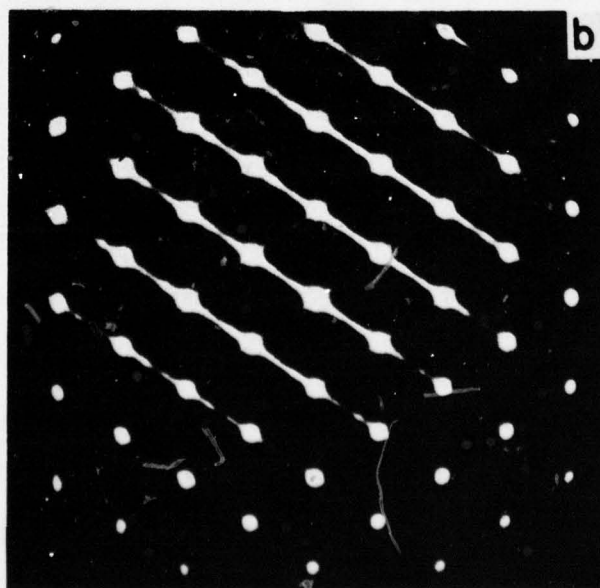


Fig. 26 TEM of GaAs implanted with 400 keV Se ions and annealed at 200°C for 1100 minutes. (a) Dark field image illustrating crystalline substructure in implanted layer. g : $\langle 111 \rangle$ streak. (b) Selected area diffraction pattern, $[110]$ zone normal with intense $\langle 111 \rangle$ streaking.



significant orientation dependence and the regrown layer exhibits a high amount of disorder. In case of Ge or Si the recovery shows a strong orientation dependence and there is low residual disorder following reordering of the amorphous layer for $< 100 >$ samples. The isochronal annealing data for GaAs shows that reordering occurs over a relatively broad temperature interval in contrast to the reordering of Si and Ge. Our results indicate that in GaAs the reordering of the implanted amorphous layer does not follow the simple epitaxial growth found in Si and Ge. We speculate that the different behavior of GaAs is due to local variations of its stoichiometry in the implanted region. At low temperatures (200 to 300°C) the amorphous layer can recrystallize, but the temperature may be too low to permit the motion of Ga and As necessary to adjust the local stoichiometry. On this basis we believe that reordering phenomena similar to that observed in GaAs will also be found in other compound semiconductors.

6.0 EFFECTS OF MATERIAL PARAMETERS ON DEVICE PERFORMANCE

6.1 Characterization of FETs Fabricated on Epitaxial and Implanted Active Layers - Science Center

In our previous report, FET devices with ion implanted and epitaxial active layers were compared. Significant differences were observed in the "settling times" of the two types of transistors. Most epitaxial transistors showed a long settling time for the noise figure after gate switching while transistors made on implanted layers responded instantly to changes in the gate bias voltage. The observed parameter drift for epitaxial transistors was attributed to the presence of interface states between the active layers and the substrates. The corresponding trap density for ion implanted transistors will be much lower since the GaAs surface is never exposed in high temperature processing.

Further exploration of the relationship between the transistor characteristics and the method of active layer preparation has been carried out. The different layers are specified in Table VIII. Simultaneous LPE growth onto two different wafers was employed in preparing the active layers of transistors 130F8. One substrate had a high-resistivity buffer layer grown by Stanford University, while the second was a regular semi-insulating substrate. Part of each layer was used for the transient capacitance experiment described in Section 4.1. Transistors of batch #912 were fabricated on layers prepared by sulfur implantation into a buffer layer also grown at Stanford University. Batch #818 was fabricated from a selenium implanted layer on a preselected substrate (see Section 5.1). Finally, the F8J60

TABLE VIII: Summary of RF Measurements of FETs at 10 GHz

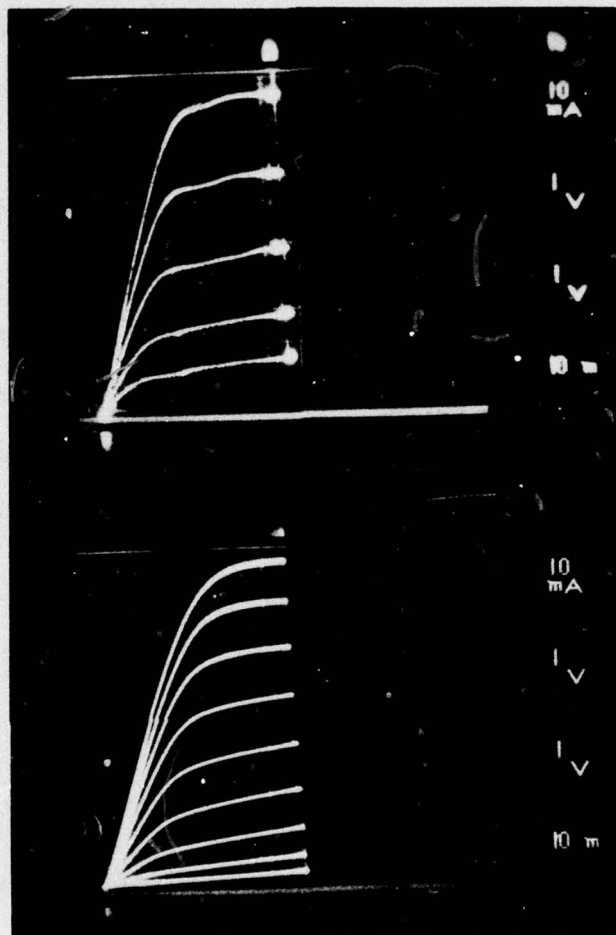
Transistors	MAG	N.F. (steady state)	N.F. (initial)	At Min. N.F. Gain
130F8-S Sn doped LPE layer on substrate	8 dB	7.95 dB	7.9 dB	5.0 dB
130F8-B Sn doped LPE on buffer layer	8 dB	6.1 dB	6.0 dB	2.5 dB
912 S implanted in buffer layer	9 dB	5.0 dB	4.6 dB	3.5 dB
818 Se implanted layer	10 dB	3.6 dB	3.6 dB	6.0 dB
F8J60 Sn doped LPE layer	13 dB	5.2 dB	4.35 dB	3.5 dB

transistors had a tin doped LPE active layer.

The purpose of comparing the two types of transistors 130F8 was to determine the merits of using a high resistivity buffer layer between the epitaxial active layer and the substrate, with respect to device performance. Improvements may be expected due to the lack of interface traps discussed in Section 4.1. Fig. 27 compares the dc characteristics of the FETs with and without the buffer layer. It is observed that the total current carried by the buffered transistor is similar to that in the unbuffered one but that the transconductance is lower. More gate voltage is required to pinch off the device. As to RF performance at 10 GHz (Table VIII), the gain is slightly better for the single layer device while the noise performance is slightly better in favor of the buffered device. These initial results indicate no obvious advantage from using a buffer layer. However, the advantage may be masked by other effects since both transistors have a rather high noise figure. Other potential advantages may exist in terms of smaller drift vs. time of RF parameters. These questions will be given further consideration.

The 912 FETs were fabricated from a sulfur implantation into a buffer layer. The peak doping of this layer was only $4 \times 10^{16} \text{ cm}^{-3}$, which limits the performance in terms of gain and noise. The measured results are summarized in Table VIII and are in good agreement with the theoretical prediction. However, the RF parameters changed as a function of time in contrast to implanted transistors on semi-insulating substrates. These transistors also display a high value of S_{12} reaching 0.15 at 10 GHz. This high value of S_{12} is attributed to the buffer layer. The buffer layer was $5 \mu\text{m}$ thick with an n-type carrier concentration in the low $10^{14} / \text{cm}^3$ range. It is possible that

(a) 130 F8 0 SINGLE LAYER
 $N = 8.5 \times 10^{16}$ $T = .30 \mu\text{M}$



(b) 130 F8 0 ACTIVE ON BUFFER
 ACTIVE: 8.5×10^{16} $T = .30 \mu\text{M}$
 BUFFER: S.U.1323 CR N 1×10^{12}

Fig. 27 Saturation characteristics of FETs fabricated from an epitaxial layer. (a) grown on an unbuffered semi-insulating substrate, (b) grown on a high resistivity LPE buffer layer.

these characteristics are responsible for undesired capacitive effects resulting in the high value of S_{12} . Further work is scheduled to investigate this possibility.

Finally, the series 818 and F8J60 allow a comparison to be made of epitaxial and selenium implanted active layers. The measurements of gain and noise indicate that the selenium devices present more gain at the minimum noise figure, while the maximum amount of gain available from the epitaxial transistor is higher. The implanted transistors are free of short term drift problems displayed by the epitaxial transistors (see Table VIII). The importance of stable performance and the similarity of device characteristics suggest that ion implantation is the better approach for preparing the active layer.

6.2 GaAs Ionization Coefficients

It has been acknowledged for several years now that series difficulties are encountered when one attempts to quantitatively model GaAs avalanche devices by specifying an electric field distribution and using published ionization coefficients. It has been thought that more accurate measurements of the ionization coefficients were needed to resolve the difficulties. Although the literature contains some measurements,⁴⁴ there are uncomfortably large differences between them. The majority of the papers on the GaAs ionization coefficients were based on measurements on diodes designed for use as IMPATTs, therefore, the experiments lacked good control over pure electron or hole injection. No attempt was made to measure the two carrier rates in the same junction. The only exception is the experiment of Stillman et al.⁴⁴ where

a serious effort was made to control these factors of injection and to measure both carrier rates in the same junction. This experiment demonstrated a new feature of the ionization rates, namely that the ionization rate of holes could exceed that of electrons. However, this experiment was performed for only a very narrow range of impurity density. There is also a significant discrepancy between theory and experiments concerning the noise measure of the diodes. The experimentally measured values were significantly lower than those predicted theoretically.⁴⁵ The lack of agreement between theory and experiment in GaAs is puzzling because of the rather good agreement that had generally been obtained for silicon avalanche diodes.^{8,46}

In an attempt to resolve these problems in GaAs, work has been carried on under the present contract to study small and large signal measurements of GaAs microwave avalanche diodes and make a more extensive study of the basic ionization coefficients of electrons and holes for a wide range of impurity density. From these studies an understanding of the physical mechanisms responsible for the discrepancies has been achieved. In the development of this understanding there were three important observations.

The first of these was the determination of the width of the avalanche zone of a flat profile IMPATT from microwave admittance measurements. It was found that the avalanche zone comprised only 12% of the transition width of the diode. For the effective avalanche width to be so narrow, the field dependence of the ionization rates had to be very strong; stronger, in fact, than indicated by any published ionization rates.⁴⁷ The second development was a means of extracting the multiplication, the saturation current, and most importantly, the intrinsic response time of the avalanche from low frequency (30-500 MHz)

measurements of the short circuit current fluctuations.⁴⁶ The results of these noise measurements verified indirect indications of microwave admittance measurements that the intrinsic response time in GaAs was an order of magnitude greater than the expected theoretical value.¹ Lastly, conventional measurements of the ionization coefficients over a wide doping range indicated that they were dependent upon the doping. That is, one could observe the same ionization rate for electrons at two widely different electric field strengths and correspondingly different doping densities. Measurements to date indicate that the field dependence of the hole ionization rate does not depend on the doping while the electron ionization rate is less than that of holes for $N_d \geq 2 \times 10^{16} \text{ cm}^{-3}$, but it exceeds the hole coefficient for $N_d \leq 7 \times 10^{15} \text{ cm}^{-3}$.

In the last semi-annual report,¹ an explanation of the origin of the observations was suggested. Specifically it was noted that only in the $\langle 110 \rangle$ direction was it possible for an electron in the normal or lower band to be accelerated to the threshold energy for pair production.⁴⁸ Knowing that the distribution function in the Γ_1 or central valley is very much like that of a drifted Maxwellian one because polar optical phonon scattering is dominant,⁴⁹ it is probable that when the electric field is in the $\langle 100 \rangle$ direction most ionizing collisions will be made by electrons that have been scattered to the $\Gamma_{15} - X_3$ band and there accelerated to the threshold energy. Thus, it is apparent that the interband scattering rate can limit the rate at which secondaries are produced, and thereby account for the observed intrinsic response time being an order of magnitude larger than expected.

The dependence of the electron ionization coefficient upon the im-

purity density is a little more difficult to see, but one can still make an argument based on an interband scattering rate limitation. As the impurity density increases, the effective width of the triangular electric field distribution decreases, and the time an electron spends in the high field portion decreases with the result that fewer interband transitions can occur. Consequently fewer electrons have the opportunity to be accelerated to the threshold energy. Thus, the number of secondary collisions is less than if interband transitions were unimportant.

The third observation to be accounted for is a narrower avalanche region width than one would estimate from the measured field dependence of the ionization coefficient. Here, one can again appeal to the fact that the effective width of the avalanche region is reduced by the distance traveled before an interband transition occurs. Very crudely one might estimate the reduced avalanche width by

$$x_1 = (1 - e^{-x_1/v_s \tau_{bb}}) v_s \tau_{bb} \quad , \quad (15)$$

where x_1 would represent the avalanche width in the limit of vanishing interband scattering time τ_{bb} .

Finally, it was noted that secondary ionization events caused by an energetic hole were not subject to interband scattering rate limitations as were electron initiated events. As a consequence the hole ionization rate ought not to depend upon the doping. Recent measurements have so far supported this view. For a donor doping level of $9 \times 10^{15} \text{ cm}^{-3}$ the hole ionization rate was observed to remain the same as that reported by Stillman et al.⁴⁴ while

the electron ionization rate increased to match that of the holes.

The reasoning pursued so far provides an adequate qualitative explanation of the exceptionally narrow avalanche width of flat profile GaAs IMPATTs, the anomalously high intrinsic response time, and the observed doping dependence of the electron ionization coefficient. However, it is not well suited to a quantitative explanation. The difficulty in quantifying the argument seems elusive until it is realized that the arguments used implicitly rest on results obtained for equilibrium distribution functions. To some extent the experience with silicon avalanche phenomena, where these anomalies are absent, may have influenced our thinking because it has been possible to use equilibrium distribution functions due to the rapid electron energy relaxation. In this case it is necessary to consider only the normal conduction band. The key point is that the time development of the electron distribution function is an important contribution to avalanche phenomena on a time scale comparable to the transit time of an electron through the avalanche region.

With the realization that non-equilibrium distribution functions are important, a quantitative approach to finding the interband scattering can be found in the Monte Carlo technique of Kurosawa⁵⁰ or the iterative integral technique of Rees.⁴⁹ Either of these methods seems quite capable of handling the increased complication of two electron conduction bands at least with a spatially uniform electric field. To correspond to this theoretical simplification of a spatially uniform field, it would seem quite feasible to obtain experimental data in long uniform fields where the electron transit time was much longer than the interband transition time.

In parallel with the efforts to explain the doping dependence of the ionization coefficients, it was necessary to further improve the accuracy of the data on ionization rates. Some new results on the ionization rates of holes and electrons in GaAs at the doping of $9.5 \times 10^{15} \text{ cm}^{-3}$ will be presented.

The material used in this experiment was grown by VPE technique at Raytheon Co. Platinum Schottky barriers were sputtered on the material and were sintered at 300°C for 45 min. A flat bottomed well was anodically etched out from the substrate side such that the thickness of the diode substrate was about 1 mil. In this structure, pure hole and pure electron excitation currents can be injected into the same junction. Electron injection was obtained by illuminating the top of the opaque platinum contact. Hole injection was obtained by strong illumination of the substrate side with non-penetrating radiation and diffusion of the generated holes to the high field region. Different frequencies of the light source were used to insure pure hole and pure electron injection. Measurements were made on several diodes and they are consistent. The multiplication curve for electron M_n and that of hole M_p were obtained.

The ionization coefficients of electrons α and holes β can be extracted by the following relationship:

$$\alpha(E_m) = E_m \left[\frac{d(\ln M_n)}{dV} - \frac{M_n - 1}{M_n} \frac{d(\ln M_p)}{dV} \right] \quad (16)$$

$$\beta(E_m) = \frac{E_m}{M_n} \frac{d(\ln M_p)}{dV} \quad (17)$$

where,

E_m = peak electric field

M_n = multiplication of electrons

M_p = multiplication of holes

V = reverse bias voltage

The values of α and β were calculated. The results together with Stillman's results⁴⁴ and previous measurements¹ of electron ionization rate are shown in Fig. 28. In the present measurement, α and β are almost the same, while in Stillman's data, β is greater than α . However, Stillman's data were taken on a sample with doping = $1-2 \times 10^{16} \text{ cm}^{-3}$.

To substantiate the results in our measurements, field uniformity inside the material was studied in detail. This study is important because ionization coefficients are strong functions of electric field. A small fluctuation of the field inside the diode will affect the accuracy of the experiment.

A thin layer of platinum was sputtered onto the same material which the ionization rate measurements were based upon. After sintering, the diodes showed good I-V characteristics on a curve tracer. One of the diodes was then scanned by a fine focused beam ($\approx 5 \mu\text{m}$ diameter) on a micrometer stage. The photoresponse and the scanning position x were traced out by a recorder. After each trace, the y position of the diode was moved upward by 1 mil, and at the same time, the zero axis of the photoresponse was moved upward by one division. By doing this, a three dimensional effect of the photoresponse along the x - y plane of the diode was obtained. In Fig. 29(a) the bias on the diode was 6V (at which the multiplication should be 1) and this trace

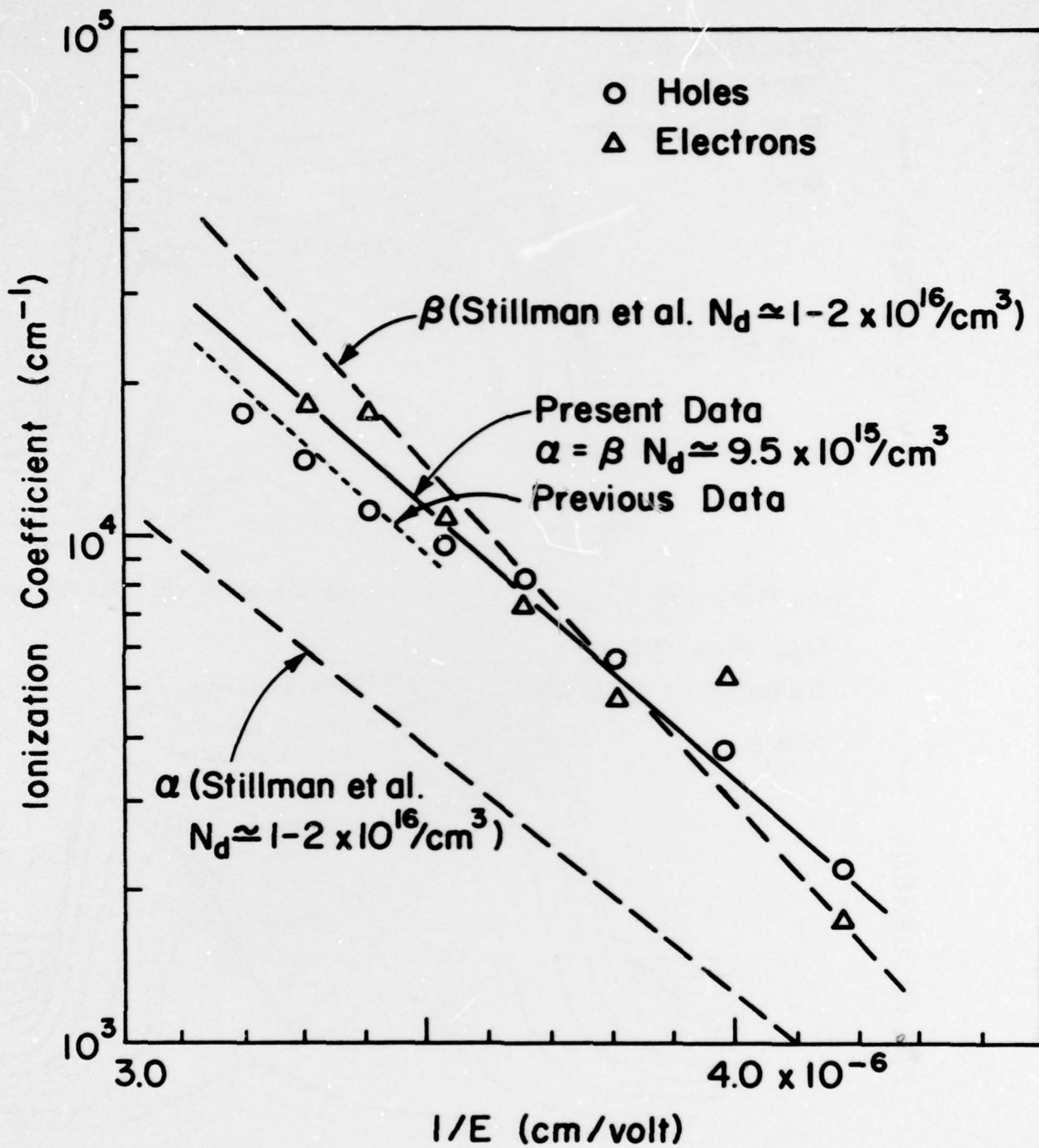


Fig. 28 Ionization coefficients of electron and hole in GaAs.

GaAs

Rev. Bias 6 V

Sensitivity 100 μV

Spot Size \rightarrow | \leftarrow

$M = 1$

PHOTOCURRENT \uparrow

1.0 mil $\frac{\uparrow}{\downarrow}$

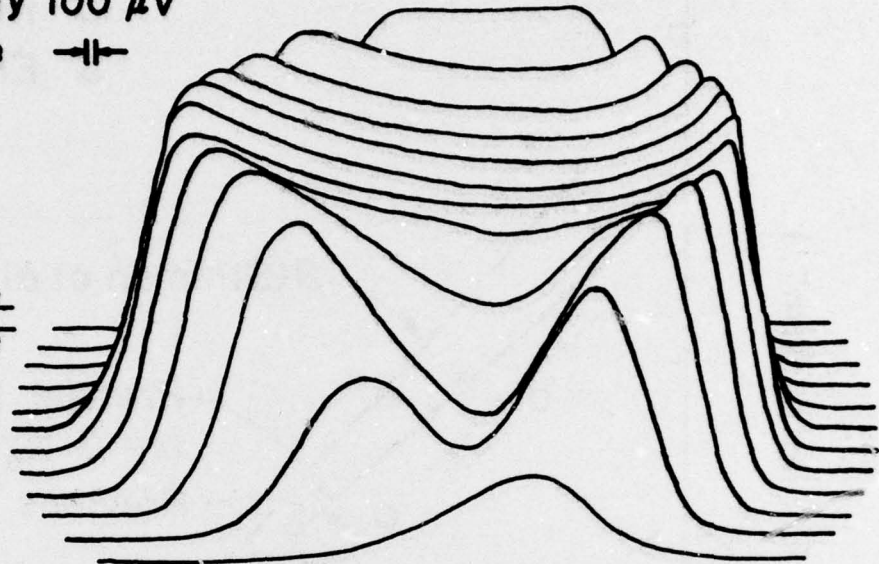


Fig. 29(a) Multiplication profile inside the diode ($N = 9.5 \times 10^{15} \text{cm}^{-3}$) for $M = 1$.

Rev. Bias 34 V

Sensitivity 200 μV

$M \approx 2$

PHOTOCURRENT \uparrow

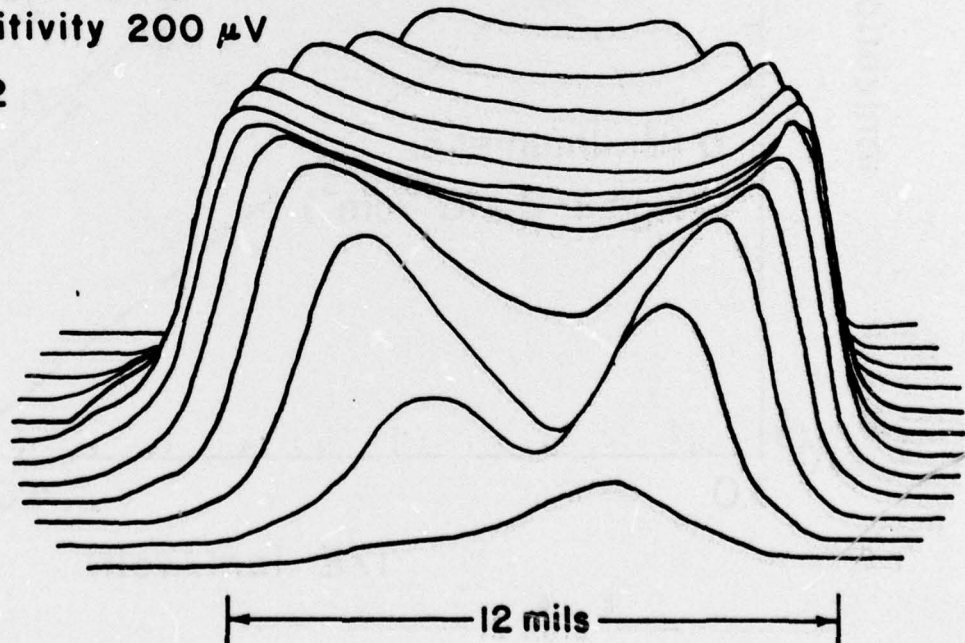


Fig. 29(b) Multiplication profile inside same diode in Fig. 29(a) for $M \approx 2$.

will act as a light intensity reference to the diode. In Fig. 29(b) the bias was brought up to 34 V ($M \approx 2$) while the sensitivity of the amplifier was decreased to half of that in Fig. 29(a). From the fluctuation of the multiplication, one can estimate the field fluctuation inside the diode. By expanding the multiplication factor to the first order, one gets:

$$\frac{1}{M} = \frac{1}{M_0} + E_0 \left. \frac{\partial \left(\frac{1}{M} \right)}{\partial E} \right|_{E=E_0} \left(\frac{\Delta E}{E_0} \right) \quad (18)$$

where,

M = multiplication factor

E_0 = electric field at the point of interest

M_0 = multiplication factor at $E=E_0$.

Therefore, the fluctuation of electric field will be:

$$\frac{\Delta E}{E_0} = \left[\frac{M_0 - M}{M M_0} \right] \left[\frac{1}{E_0 \left. \frac{\partial \left(\frac{1}{M} \right)}{\partial E} \right|_{E=E_0}} \right] \quad (19)$$

$$\approx \left(\frac{\Delta M}{M_0^2} \right) \left(\frac{1}{E_0 \left. \frac{\partial \left(\frac{1}{M} \right)}{\partial E} \right|_{E=E_0}} \right)$$

Assuming $\alpha = \beta$ (which is reasonable at this doping),

$$1 - \frac{1}{M} = \int_0^w \alpha dx \quad (20)$$

Or,

$$-\frac{d\left(\frac{1}{M}\right)}{dE} = \frac{\epsilon}{qN} \int_0^{E_0} \frac{d\alpha}{dE} dE \quad (21)$$

In the last expression, triangular field has been assumed, such that at $x = 0$, $E = 0$ and at $x = w$, $E = E_0$. Using the data for $\alpha(E)$ in Fig. 28, at $E_0 = 3 \times 10^5$ Volt/cm (corresponds to 34V bias, at which data in Fig. 29(b) was taken):

$$-\left. \frac{d\left(\frac{1}{M}\right)}{dE} \right|_{E=E_0} = 3.15 \quad (22)$$

Therefore, taking $M_0 = 2$, the ratio of field fluctuation according to Eq. (19) is

$$\frac{\Delta E}{E_0} \approx \frac{1}{6.3} \frac{\Delta M}{M_0} \quad (23)$$

It is obvious that in Fig. 29(a) and Fig. 29(b), the multiplication fluctuation is less than 15%. Therefore, the field fluctuation should be less than 3%.

Several attempts have been made on similar measurements of α and β in the other doping ranges. However, due to material quality limitations, the experiments were not as successful as the one described. The difficulties were mainly due to the nonuniform doping and high trap densities inside the materials. Also, edge breakdown on the planar diodes has been observed in many cases. Some of them were so severe that when the diodes were reverse

biased to 0.3 mA, bluish white light could be seen around the edges through a microscope, in a dark room. Anodic oxide has been grown on the surface and a structure as shown in Fig. 30 was fabricated to prevent edge breakdown. However, the improvement was still not satisfactory. Surface passivation with silicon monoxide will be investigated in the future.

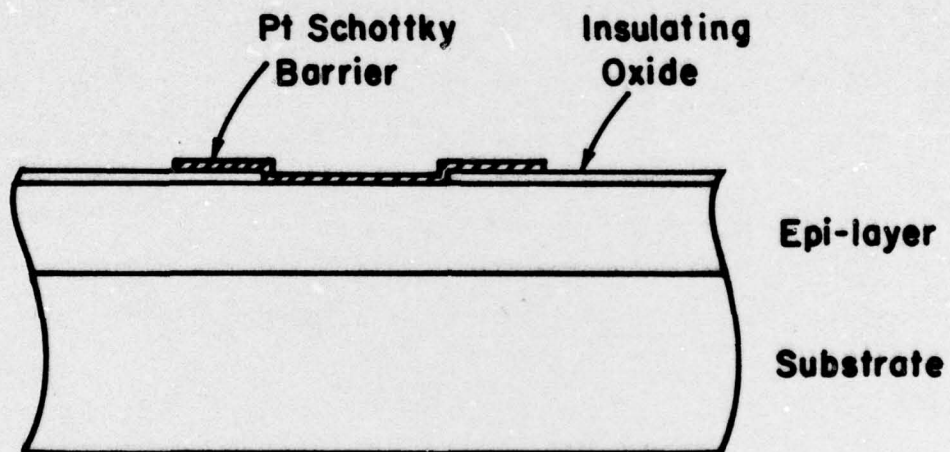


Fig. 30 Pt Schottky barrier in GaAs with native oxide guard ring.

7.0 FUTURE PLANS

7.1 Semi-Insulating Substrate Material Growth - Crystal Specialties

Efforts will continue to identify the causes of boat wetting.

Attempts to associate the variations in resistivity due to heat treatment with crystal growth conditions will be made.

7.2 Semi-Insulating Substrate Material Evaluation - Science Center

Study of the effects of heat treatment will be continued. Photoluminescence measurements at 4.2K will be performed. Samples will be heat treated at different As overpressures in order to study the mechanism of vacancy formation. The effects of heat treatment in H₂ atmosphere will be compared with the effects of heat treatment with protective caps similar to those used in post-implantation anneal.

7.3 LPE Growth and Evaluation of Semi-Insulating Buffer Layers - Stanford University

A. Further studies on the control of the growth conditions in the SiO₂-BN-H₂ system at the transition temperature will be carried out in order to grow semi-insulating GaAs LPE layers reproducibly.

B. Studies on the interface properties between the active epitaxial layer and the high-resistivity buffer layer will be continued in order to investigate the mechanisms of the trapping effects.

C. Studies of the carrier density profiles and the effects of the substrate on semi-insulating GaAs layers will be made by oxide stripping and differential Van der Pauw measurements.

7.4 LPE Growth of FET Active Buffer Layers - Cornell University

Tests will continue on LPE growth in the POCO graphite boat and the Spectrasil quartz boat to improve buffer layer purity. In addition, control of thickness of active layers, grown immediately after buffer layers, will be sought by using thin melts.

7.5 Ion Implantation and Ion Beam Analysis

In the next six month period more detailed studies of the metallurgy of contact systems for GaAs and TEM studies of the structure of reordered amorphous layers on GaAs will be made. The influence of the properties of semi-insulating substrate material on the results of low dose implants will be explored further. Studies of the lattice location of implanted sulfur in GaAs will be carried out using channeling techniques and ion induced X-rays.

7.6 Effects of Material Parameters on FET Performance - Science Center

Studies to correlate the RF performance of FET devices with the fabrication procedure of the active layer will be continued. This includes comparison between epitaxial and implanted device layers fabricated with or without buffer layers.

7.7 GaAs Ionization Coefficients - Cornell University

Effort will continue to extend measurements of the ionization coefficient to higher resistivity material utilizing an oxide edge protection. This new structure will permit refinement of measurement of micro-inhomogeneities. Effort will continue on determination of the interband scattering time.

8.0 REFERENCES

1. F. H. Eisen, J. A. Higgins, A. A. Immorlica, Jr., R. L. Kuvås, B. W. Ludington, B. M. Welch, C. P. Wen and R. R. Zucca, "Investigation of Technological Problems in GaAs," Semi-annual Technical Report No. 2, AFCRL-TR-75-0435, January 22, 1976, Contract No. F19628-75-C-0113.
2. J. Blanc and L. R. Weisberg, *Nature* 192, 155 (1961).
3. R. W. Haisty, E. W. Mehal, and R. Stratton, *J. Phys. Chem. Sol.* 23, 829 (1962).
4. G. R. Cronin and R. W. Haisty, *J. Electrochem. Soc.* 111, 874 (1964).
5. T. Inoue and M. Ohyama, *Sol. State Comm.* 8, 1309 (1970).
6. D. C. Look, *J. Phys. Chem. Solids* 36, 1311 (1975).
7. A. T. Philadelphus and P. C. Euthymiou, *J. Appl. Phys.* 45, 955 (1974).
8. F. H. Eisen, J. A. Higgins, A. A. Immorlica, Jr., R. L. Kuvås, B. W. Ludington, B. M. Welch, C. P. Wen and R. R. Zucca, "Investigation of Technological Problems in GaAs," Semi-annual Technical Report No. 1, AFCRL-TR-75-0435, October 15, 1975, Contract No. F19628-75-C-0113.
9. We used for n_i the room temperature (298K) value $n_i = 3.6 \times 10^6 \text{ cm}^{-3}$ determined by transport measurements on semi-insulating GaAs.⁶
10. C. D. Thurmond, *J. Electrochem. Soc.* 122 1133 (1975).
11. W. J. Turner, G. D. Pettit, and N. G. Ainslie, *J. Appl. Phys.* 34, 3274 (1963).

12. J. C. Carballes and J. Lebailly, Sol. State Comm. 6, 167 (1968).
13. G. A. Allen, J. Phys. D 1, 593 (1968).
14. T. Nishino, T. Yanagida, and Y. Hamakawa, Japan. J. Appl. Phys. 11, 1221 (1972).
15. H. J. Stocker and M. Schmidt, J. Appl. Phys. 47, 2450 (1976).
16. R. F. Broom, J. Appl. Phys. 38, 3483 (1967).
17. A. L. Lin and R. H. Bube, J. Appl. Phys. 47, 1859 (1976).
18. D. Bois and P. Pinard, Phys. Rev. B9, 4171 (1974).
19. J. Barrera, Proc. Fifth Biennial Cornell Electrical Engineering Conference, Cornell University, Ithaca, New York, p. 135 (1975).
20. M. D. Sturge, Phys. Rev. 127, 768 (1962).
21. M. I. Nathan and G. Burns, Phys. Rev. 129, 125 (1963).
22. C. J. Hwang, Phys. Rev. 180, 827 (1969).
23. W. Schairer and N. Stath, J. Appl. Phys. 43, 447 (1972).
24. J. A. Rossi, C. M. Wolfe and J. O. Dimmock, Phys. Rev. Lett. 25, 1614 (1970).
25. D. J. Ashen, P. J. Dean, D. T. J. Hurle, J. B. Mullin, A. M. White, and P. D. Greene, J. Phys. Chem. Solids 36, 1041 (1975).
26. E. W. Williams and C. T. Elliot, J. Phys. D 2, 1657 (1969).
27. E. Munoz, W. L. Snyder and J. L. Moll, Appl. Phys. Lett. 16, 262 (1970).
28. S. Y. Chiang and G. L. Pearson, J. Appl. Phys. 46, 2986 (1975).

29. P. L. Hower, W. W. Hooper, D. A. Tremere, W. Lehrer and C. A. Bittmann, in Proc. of 1969 Symposium on GaAs (The Institute of Physics and the Physical Society of London, 1970) p. 187.
30. K. Lehovec and R. Zuleeg, Inst. Phys. Conf. Ser. No. 24, 292 (1975).
31. Done by POCO Graphite, Inc.
32. A. A. Immorlica and F. H. Eisen, Appl. Phys. Lett. 29, 94 (1976).
33. J. W. Mayer, L. Eriksson and J. A. Davies, Ion Implantation in Semiconductors (Academic Press, New York, 1970) p. 65.
34. L. Csepregi, J. W. Mayer and T. W. Sigmon, Phys. Lett. 54A, 157 (1975).
35. J. W. Mayer, L. Csepregi, J. Gyulai, T. Nagy, G. Mezey, P. Revesz and E. Kotai, Thin Solid Films 32, 303 (1976).
36. S. T. Picraux, Radiation Effects 17, 261 (1973).
37. R. G. Hungperger, E. D. Wolf, G. A. Shifrin, O. J. Marsh and D. M. Jamba, Radiation Effects in Semiconductors, Ed. by J. W. Corbett and G. D. Watkins (Gordon and Breach, London, 1971), p. 393.
38. G. Carter, W. A. Grant, J. D. Haskell and G. A. Stephens, Ion Implantation, Eds. F. H. Eisen and L. T. Chadderton (Gordon and Breach, London, 1971), p. 261.
39. J. S. Harris, F. H. Eisen, B. Welch, R. D. Pashley, D. Sigurd and J. W. Mayer, Appl. Phys. Lett. 21, 601 (1972).
40. T. Shimada, Y. Kato, Y. Shiraki and K. F. Komatsubara, J. Phys. Chem. Solids 37, 305 (1976).

41. L. Csepregi, W. K. Chu, H. Müller, J. W. Mayer and T. W. Sigmon, *Rad. Effects* 28, 227 (1976).
42. J. F. Ziegler and W. K. Chu, *Atomic Data and Nuclear Data Tables* 13, 463 (1974).
43. L. Csepregi (private communication).
44. G. E. Stillman, C. M. Wolfe, J. A. Rossi and A. G. Foyt, *Appl. Phys. Lett.* 24, 471 (1974).
45. H. Statz, R. A. Pucel, and J. Simpson, "Noise in Gallium Arsenide Avalanche Read Diodes," to be published.
46. F. H. Eisen, J. A. Higgins, B. M. Welch, C. P. Wen and R. Zucca, "Investigation of Technological Problems in GaAs," Semi-annual Technical Report No. 2, AFCRL-TR-74-0371, July 30, 1974, Contract No. F19628-74-C-0038.
47. F. H. Eisen, B. M. Welch, C. P. Wen and R. Zucca, "Investigation of Technological Problems in GaAs," Semi-annual Technical Report No. 3, AFCRL-TR-75-0093, February 5, 1975, Contract No. F19628-74-C-0038.
48. C. L. Anderson and C. R. Crowell, *Phys. Rev.* B5, 2267 (1972); M. L. Cohen and T. K. Bergstresser, *Phys. Rev.* 141, 789 (1966).
49. H. D. Rees, *J. Phys. Chem. Solids* 30, 643 (1969).
50. T. Kurosawa, Proc. of International Conference on the Physics of Semiconductors, Kyoto, 1966. *J. Phys. Soc. Japan (Supplement)* 21, 242 (1966).